Modification of electronic properties of graphene by interaction with substrates and dopants

Submitted by Alexander Markevich to the University of Exeter
as a thesis for the degree of Doctor of Philosophy in Physics.

December, 2012

This thesis is available for library use on the understanding that it is copyright material and that no quotation from the thesis may be published without proper acknowledgement.

I certify that all material in this thesis which is not my own work has been identified and that no material has previously been submitted and approved for the award of a degree by this or any other University.

Abstract

First-principles calculations have been carried out to investigate structural and electronic properties of graphene on SiC and diamond substrates and for a study of doping of fluorographene with various surface adsorbates.

New insight is given into the problem of the decoupling of the graphene layers from SiC substrates after epitaxial growth. Mechanisms of hydrogen penetration between graphene and SiC(0001) surface, and properties of hydrogen and fluorine intercalated structures have been studied. Energy barriers for diffusion of atomic and molecular hydrogen through the interface graphene layer with no defects and graphene layers containing Stone-Wales defect or two- and four-vacancy clusters have been calculated. It is argued that diffusion of hydrogen towards the SiC surface occurs through the hollow defects in the interface graphene layer. It is further shown that hydrogen easily migrates between the graphene layer and the SiC substrate and passivates the surface Si bonds, thus causing the graphene layer decoupling. According to the band structure calculations the graphene layer decoupled from the SiC(0001) surface by hydrogen intercalation is undoped, while that obtained by the fluorine intercalation is p-type doped.

Further, structure and the electronic properties of single and double layer graphene on H-, OH-, and F- passivated (111) diamond surface have been studied. It is shown that graphene only weakly interacts with the underlying substrates and the linear dispersion of graphene π-bands is preserved. For graphene on the hydrogenated diamond surfaces the charge transfer results in n-type doping of graphene layers and the splitting of conduction and valence bands in bilayer graphene. For the F- and OH-terminated surfaces, charge transfer and doping of graphene do not occur.

Finally, the possibility of doping fluorographene by surface adsorbates have been investigated. The structure and electronic properties of fluorographene with adsorbed K, Li,

Au atoms, and F4-TCNQ molecule are described. It is shown that adsorption of K or Li atoms results in electron doping of fluorographene, while Au atoms and F4-TCNQ introduce deep levels inside the band gap. The calculated value of the fluorographene work function is extremely high, 7.3 eV, suggesting that p-type doping is difficult to achieve.

Acknowledgements

I would sincerely like to thank my supervisor, Bob Jones, for accepting me as a PhD student. Through the time of my PhD study, I have felt Bob's full support and has benefitted from his exceptional experience and knowledge.

I wish to thank Derek Palmer and Hugo Pinto for being my mentors and for providing me with general support in Exeter.

I wish to express my thanks to all the members of AIMPRO group for their friendly support and very helpful discussions. Specially I am grateful to Professor Sven Öberg for collaborating on many problems and for the great and productive time I had in Luleå . Many thanks to Chris Ewels, Jonathan Goss, Patrick Briddon, Mark Rayson, José Coutinho and Alexandra Carvalho for their assistance and partnership.

I am very grateful for the financial support provided by College of Engineering, Mathematics and Physical Sciences of the University of Exeter.

I gratefully thank my family for kind support and encouragement.

Contents

List of Tables **9**

List of Figures **11**

List of Publications **20**

1 Introduction **21**

1.1 Graphene crystal structure 22

1.2 Electronic structure of graphene 22

1.3 Production of graphene 25

1.4 Doping of graphene 26

1.5 Effect of substrates on electronic transport in graphene 27

1.6 Band-gap engineering in graphene 29

1.7 Goals of the present work 30

1.8 Thesis organisation 31

2 Method **32**

2.1 Many body problem 32

2.2 Born-Oppenheimer approximation 34

2.3 Variational principle 35

2.4 Density Functional Theory 37

2.4.1 Kohn-Sham equations 38

2.4.2 The exchange-correlation functional 39

2.5 Pseudopotentials 42

2.6 The AIMPRO implementation of DFT 45

2.6.1 The supercell method 45

2.6.2 Basis functions 46

2.6.3 Basis functions in reciprocal space 47

2.6.4 Sampling of the Brillouin zone 48

2.7 Modelling graphene 49

2.7.1 Choice of k-points for the graphene Brillouin zone sampling . . . 51

3 Intercalation of hydrogen and fluorine into graphene/SiC(0001) interface **54**

3.1 Introduction 54

3.2 Details of calculations 57

3.3 Electronic and structural properties of the interfacial carbon layer on SiC(0001) according to the $R3$ and 4×4 models 59

3.4 Effect of lattice strain on the binding energy and diffusion of hydrogen through a graphene layer 62

3.5 Properties of a quasi-free-standing graphene layer on H- and F-passivated SiC(0001) 66

3.6 Mechanisms for hydrogen penetration through the interfacial carbon layer on SiC(0001) 69

3.7 Hydrogen diffusion between the interfacial carbon layer and SiC substrate 75

3.8 A model of hydrogen intercalation into graphene/SiC interface 76

3.9 Conclusions 77

4 Graphene on diamond substrates 79

4.1 Introduction 79

4.2 Details of calculations 81

4.3 Effect of the termination on the diamond (111) surface electronic properties 86

4.3.1 Clean surface 86

4.3.2 Hydrogenated surface 87

4.3.3 Fluorinated surface 89

4.3.4 Hydroxylated surface 90

4.4 Graphene on passivated diamond substrates 92

4.4.1 Graphene on the H-passivated diamond (111) surface 92

4.4.2 Graphene on the F- and OH-passivated diamond (111) surfaces . 95

4.4.3 Bilayer graphene on the passivated diamond substrates 96

4.5 Discussion 97

4.6 Conclusions 99

5 Doping of fluorographene by surface adsorbates 100

5.1 Introduction 100

5.2 Details of calculations 102

5.3 Structural and electronic properties of fluorographene 102

5.4 K, Li and Au atoms on fluorographene 105

5.5 F4-TCNQ on fluorographene 110

5.6 Effect of doping on structural parameters of fluorographene 112

5.7 Conclusions 113

6 Concluding remarks 115

6.1 Summary 115

6.1.1 Graphene on SiC(0001) substrates 115

6.1.2 Graphene on passivated diamond substrates 117

6.1.3 Doping of fluorographene by surface adsorbates 119

6.2 Outlook 119

List of Tables

3.1 Calculated values for the average distance between the ICL and the SiC surface, h, maximum difference in the height of C atoms in the ICL, Δh, and the binding energy per C atom, E_b, for the ICL on the SiC(0001) surface. 62

3.2 Calculated values of the formation energy, $E_{\rm f}$, the binding energy per C atom, $E_{\rm b}$, and the distance from the substrate, h, for the quasi-free-standing graphene layer obtained by intercalation of hydrogen and fluorine atoms. The distance h is calculated with respect to H(F) atoms. . . . 68

3.3 Calculated values of energy barriers in eV for H diffusion through a perfect graphene layer and a heptagon in a Stone-Wales (SW) defect and for H_2 diffusion through the SW, V_2 and V_4 defects in the free standing graphene layer. The energy barriers were calculated with respect to H and H_2 remote from the graphene layers. 74

5.1 Structural parameters and electron energy gap (E_g) for fluorographene derived from the present calculations. The values from the other theoretical and experimental works are shown for comparison. The FG lattice constant, a_0, and the C-C and C-F bond lengths, d_{CF} and d_{CC}, are shown in angstroms (Å). The angles between bonds, θ_{CCF} and θ_{CCC}, are in degrees. 103

5.2 Experimental values of the ionization energy (IE) of metal atoms [131] and calculated values of the binding energy, E_b, optimum height, h, and magnetic moment, M, for the metal atoms and F4-TCNQ at the most favourable adsorption site on top of fluorographene. The heights are calculated with respect to the top fluorine atoms. The type of doping due to the adsorbates is also shown. 106

5.3 Structural parameters calculated for pristine fluorographene, for fluorographene with the negative charge of 1 e added to the 4×4 cell and for fluorographene beneath the adsorbed metallic atom. 113

List of Figures

1.1 (a) Crystallographic structure of graphene. The primitive lattice vectors are defined as $\mathbf{a_1}$ and $\mathbf{a_2}$. Graphene lattice can be considered as a hexagonal lattice with two atoms per unit cell (atoms A and B). Alternatively it can be represented as a superposition of two sublattices shown in different colours. Each sublattice contains only atoms that can be translated by the primitive lattice vectors, i.e. only atoms A or only atoms B. (b) First Brillouin zone of graphene with the reciprocal lattice vectors defined as $\mathbf{b_1}$ and $\mathbf{b_2}$. High symmetry **k**-points are labeled as **Γ**, **M**, **K** and **K´**. . . . 23

2.1 Calculated electronic band structure of graphene. Red solid lines represent occupied states, while blue dashed lines represent empty states. The zero of the energy scale is set to the Fermi level. 50

2.2 Plot of the xy-plane-averaged electrostatic potential as a function of the position along the z axis for a graphene layer. Graphene carbon atoms was positioned at $z = 0$. The black solid line defines the position of the vacuum level. 51

2.3 Convergence of (a) the total energy (b) the Fermi level with the number of $\mathbf{k}$-points $(N \times N \times 1)$ for the Brillouin zone sampling for band structure calculations. The red and black circles are for the initial shifts of (0.5;0.5;0.5) and (0;0;0) respectively. The lines are plotted as guides for eyes. 53

3.1 Schematic representations of atomic structures and calculated electronic band structures of the iterfacial carbon layer (ICL) on the $(\sqrt{3}\times\sqrt{3})R30^{\circ}$ (a) and (c), and the 4×4 (b) and (d) SiC(0001) surface reconstructions. The $(\sqrt{3} \times \sqrt{3})R30^{\circ}$ unit cell is indicated in (a). Silicon atoms are represented by large (yellow) circles. Smaller dark gray and light gray circles represent carbon atoms in the ICL and in the SiC substrate, respectively. Solid (red) lines represent occupied states, while (blue) dashed lines represent empty states. The position of the Fermi level is set to zero. The inset in (d) shows that graphene π and π^{*} bands are separated by the energy gap of 30 meV at the K-point in the Brillouin zone. 60

3.2 The calculated values of the binding energy of an H atom on graphene (blue triangles) and diffusion barrier of an H atom through a graphene sheet (red and black circles and squares) for different values of the graphene lattice constant stretching. Circles and squares distinguish two different dependencies of the diffusion barrier versus strain that correspond to the change of H diffusion path through the graphene layer. Open circles and squares shows the calculated diffusion barriers if the binding energy term is excluded from the Eq. 3.1. This corresponds to energy barriers for H diffusion through a graphene layer if the initial configuration is defined as an H atom remote from the layer. Lines represent linear fits to the data. . . 64

3.3 The calculated band structures for a graphene layer on top of the (a) hydrogenated and (b) fluorinated SiC(0001) surface calculated with the use of the 4×4 model. Solid (red) lines represent occupied states, while (blue) dashed lines represent empty states. The position of the Fermi level is set to zero. 67

3.4 (a) Initial, saddle point and final configurations for H diffusion through the intefacial carbon layer (ICL) on the 4×4 SiC(0001) surface reconstruction. The total energy variation along the corresponding diffusion path is shown in (b). Black circles correspond to the calculated energies of atomic configurations along the diffusion path relative to the energy of the initial configuration. N is the number of an atomic configuration along the diffusion path. N equal 1, 4 and 7 corresponds to the initital, saddle point and final configurations, respectively. The blue solid curve is an interpolation shown as a guide for eyes. In (c) considered adsorption sites for an H atom on the ICL are marked out and numbered. The H atom adsorbed on the site 1 corresponds to the initital configuration for the modelled diffusion path. 70

3.5 Atomic structures of Stone-Wales (SW), V_2 and V_4 defects in graphene. The SW defect (c) is formed by in-plane 90° rotation of the C–C dimer shown in red in (a). Removal of the C–C dimer results in the formation of the V_2 defect (d). The V_4 defect (e) is formed by the removal of four C atoms shown in (b) with red colour. The structures shown in (c)–(e) are the reconstructed defect structures. 72

3.6 The total energy variation, $E_i - E_{\text{init}}$, along the paths for (a) H diffusion through a heptagon in a Stone-Wales defect and (b) for H_2 diffusion through the SW (blue circles), V_2 (black squares) and V_4 (red triangles) defects in the graphene layer. The symbols correspond to the calculated energies of atomic configurations along a diffusion path, E_i, relative to the energy of the corresponding initial configuration E_{init}. z-positions correspond to positions of a hydrogen atom or the center of a hydrogen molecule along the axis perpendicular to the graphene plane. The zero of this axis is the position of the graphene plane. The solid curves are the interpolations shown as guides for eyes. 73

3.7 A path for H_2 diffusion through the V_4 defect. Positions of the H_2 molecule in the initial and saddle point configurations are denoted by I and SP respectively. 74

3.8 Schematic representation (a) H and (b) H_2 diffusion along the SiC surface below the interface graphene layer. Silicon atoms are represented by large yellow circles. Smaller dark gray and light gray circles represent carbon atoms in the graphene layer and in the SiC substrate, respectively. The arrows show the direction of hydrogen diffusion. 76

4.1 (a) The unit cell of the hydrogenated diamond substrate. (b) Atomic structure of graphene with the orthorhombic unit cell defined by the blue solid rectangle and the conventional unit cell defined by the blue dashed rhomb. (c) The Brillouin zone for the orthorhombic unit cell of graphene and diamond slab. Shaded region shows the irreducible part of the Brillouin zone with the **k**-points labelled. (d) The electronic structure of graphene with the equilibrium (red solid lines) and extended (blue dashed lines) lattice constants. The zero of the energy scale is set to the Fermi level. 82

4.2 (a) Optimized atomic geometry and (b) calculated electronic band structure of the Pandey-chain reconstructed (111) diamond surface. Solid (red) lines represent occupied states, while (blue) dashed lines represent empty states. The zero of the energy scale is the vacuum level. Shaded regions represent the aligned band structure of the bulk diamond. The horizontal solid black line defines the Fermi energy. 87

4.3 (a) Optimized atomic geometry and (b) calculated electronic band structure of the H-terminated (111) diamond surface. Carbon atoms are represented with large grey spheres, while H atoms are shown by small white spheres. The band labeled as A originates from the C-H σ bonds and is characteristic for hydrogenated diamond surfaces. 88

4.4 (a) Optimized atomic geometry and (b) calculated electronic band structure of the F-terminated (111) diamond surface. Carbon atoms are represented with large dark grey spheres, while F atoms are shown by smaller light grey spheres. 89

4.5 Optimized atomic geometry of the OH-terminated (111) diamond surface: (a) side view and (b) top view. Large grey spheres represent carbon atoms, red spheres show oxygen atoms, and small white spheres are hydrogen atoms. 90

4.6 Calculated electronic band structure of the OH-terminated (111) diamond surface. Solid (red) lines represent occupied states, while (blue) dashed lines represent empty states. The zero of the energy scale is the vacuum level. Shaded regions represent the aligned band structure of the bulk diamond. 91

4.7 Optimized atomic geometry of a graphene layer on the H-terminated (111) diamond surface: (a) side view and (b) top view. Carbon atoms are represented with large grey spheres, while H atoms are shown by small white spheres. In (b) graphene lattice is shown by blue wireframe. 92

4.8 (a) Calculated electronic band structure for a single graphene layer on the hydrogenated diamond (111) surface. Solid (red) lines represent occupied states, while (blue) dashed lines represent empty states. The zero of the energy scale is the vacuum level. Shaded regions represent the aligned band structure of the bulk diamond. The horizontal solid black line defines the Fermi energy. (b) and (c) show the plot of the charge density with two isosurface values for the states defined as B and C in (a) respectively. Blue and red colors correspond to the charge density of unoccupied (b) and occupied (c) states respectively. The state defiend as A is referred to in the text. 93

4.9 Calculated electronic band structure for a single graphene layer on the (a) F- and (b) OH-terminated diamond (111) surfaces. Solid (red) lines represent occupied states, while (blue) dashed lines represent empty states. The zero of the energy scale is the vacuum level. The horizontal solid black line defines the Fermi energy. 96

4.10 Calculated electronic band structure for a bilayer graphene on the (a) H-, (b) F-, and (c) OH-terminated diamond (111) surfaces. The zero of the energy scale is the vacuum level. The horizontal solid black line defines the Fermi energy. 97

4.11 Calculated values of ionization potentials (red lines) end electron affinities (blue lines) for H-, F- and OH-terminated (111) diamond surfaces. The bulk related values are defined by short solid lines, while the surface related values are shown with short dashed lines. The zero of the energy scale is the vacuum level V_{vac}. Long dashed line defines the calculated work function of graphene, W_{GR}. All energy values are given in eV. . . . 98

5.1 Schematic representation of the fluorographene atomic structure: (a) side view and (b) top view. Dark grey and green (light grey) spheres represent carbon and fluorine atoms respectively. 103

5.2 Calculated electronic band structure of (a) graphene and (b) fluorographene. Red solid lines represent occupied states, while blue dashed lines represent empty states. The zero of the energy scale is set to the Fermi level in (a) and to the valence band maximum in (b). 104

5.3 (a) Schematic representation of 4×4 fluorographene supercell. Dark grey and light grey spheres represent C-F units with fluorine atoms above and below the fluorographene plane, respectively. Small filled circles show the most favorable adsorption sites for metal atoms on FG, which are above the centre of triangles formed by the three nearest fluorine atoms. Positions marked by opened circle and those directly above the fluorine atoms are less favorable. (b) Side view of fluorographene with an adsorbed metal atom. 105

5.4 The calculated electronic band structure of (a) the 4×4 fluorographene supercell, and (b) fluorographene with an adsorbed K atom. Red solid lines represent occupied states, while blue dashed lines represent empty states. The valence band maximum is set to zero. The Fermi level in (b) is shown with a black solid line and labeled as E_F. The arrow points at the position of the potassium $4s^1$ level. Points labeled as A, B and C are the points at which wave functions are calculated. 107

5.5 Plot of the real part of the wave function for (a) fluorographene at point A in Fig. 5.4(a) and (b) for fluorographene with the adsorbed K atom at point B in Fig. 5.4(b). Carbon atoms are shown in dark grey color, while fluorine atoms are in green (light grey) color. Red and blue colors correspond to the different signs of the wave function. Note that the state in (a) is empty while the same delocalized state is occupied in (b) showing that doping has occured. 107

5.6 Plot of the real part of the wave function for the half-filled metallic level of fluorographene with the adsorbed K atom at a) point B and b) point C of the bandstructure shown in Fig. 5.4(b). Carbon atoms are shown in dark grey color, while fluorine atoms are in green (light grey) color. Red and blue colors correspond to the different signs of the wave function. . . 109

5.7 (a) Spin-up and (b) spin-down band structures for fluorographene with the adsorbed Au atom. Red solid lines represent occupied states, while blue dashed lines represent empty states. The valence band maximum is set to zero. 110

5.8 (a) Molecular structure of F4-TCNQ and (b) F4-TCNQ on top of fluorographene. Carbon atoms are shown in grey color. Fluorine and nitrogen atoms are represented with green and blue colors and labeled as F and N respectively. (c) Electronic band structure of fluorographene with the F4-TCNQ molecule. Red solid lines represent occupied states, while blue dashed lines represent empty states. The valence band maximum is set to zero. 111

List of Publications

1. *First principles study of hydrogen-induced decoupling of epitaxial graphene from SiC substrates*
   A. V. Markevich, R. Jones, S. Öberg, and P. R. Briddon,
   Physics, Chemistry and Applications of Nanostructures, Proceedings of International Conference Nanomeeting-2011, edited by V. Borisenko, S.V. Gaponenko, V.S. Gurin, and C.H. Kam (World Scientific, New Jersey, 2011), pp. 311-314.

2. *Doping of fluorographene by surface adsorbates*
   A. Markevich, R. Jones, and P. R. Briddon,
   Phys. Rev. B 84, 115439 (2011).

3. *First-principles study of hydrogen and fluorine intercalation into graphene-SiC(0001) interface*
   A. Markevich, R. Jones, S. Öberg, M. J. Rayson, J. P. Goss, and P. R. Briddon,
   Phys. Rev. B 86, 045453 (2012).

4. *Graphene on diamond substrates*
   A. Markevich, R. Jones, S. Öberg, M. J. Rayson, J. P. Goss, and P. R. Briddon,
   submitted to Phys. Rev. B.

Chapter 1

Introduction

Graphene is a monolayer of carbon atoms arranged in a two-dimensional (2D) hexagonal lattice. Initially graphene has been studied theoretically as a basic building block of graphite. In 1947 Wallace [1] showed that graphene is a zero-gap semiconductor with unusual linear dispersing electronic excitations more recently called Dirac electrons. Later graphene was used as a model subject to describe the properties of carbon nanotubes and fullerenes. The existence of graphene, as well as other (2D) crystals, in a free state was doubted, since it was shown theoretically that two dimensional crystals are thermodynamically unstable [2,3]. However, in 2004 Kostya Novoselov, Andre Geim et al. [4] managed to observe single graphene layers created by mechanical exfoliation of graphite and investigate their properties. It was further shown that charge carriers in graphene indeed have a linear dispersion relation and exhibit properties specific for a two-dimensional gas of massless Dirac fermions [4–8]. The discovery of graphene has provided a new insight into low-dimensional physics and has given a possibility to observe experimentally phenomena that were predicted for 2D systems. Graphene also shows remarkable transport [5,9], optical [10,11] and mechanical [12] properties which open a fertile ground for applications.

1.1 Graphene crystal structure

The crystal structure of graphene can be represented as a hexagonal lattice with a basis of two atoms per unit cell Fig. 1.1(a) [13]. The primitive lattice vectors can be written as

$$\mathbf{a_1} = \frac{a_0}{2}(3, \sqrt{3}), \qquad \mathbf{a_2} = \frac{a_0}{2}(3, -\sqrt{3}), \tag{1.1}$$

where $a_0 \approx 1.42\,\text{Å}$ is the distance between neighbouring carbon atoms. The graphene lattice constant is then $a = |\mathbf{a_1}| = |\mathbf{a_2}| = \sqrt{3}a_0 \approx 2.46\,\text{Å}$. The corresponding reciprocal lattice vectors (Fig. 1.1(b)) are given by

$$\mathbf{b_1} = \frac{2\pi}{3a_0}(1, \sqrt{3}), \qquad \mathbf{b_2} = \frac{2\pi}{3a_0}(1, -\sqrt{3}) \tag{1.2}$$

Figure 1.1(b) shows the first Brillouin zone of graphene with the high symmetry **k**-points defined as

$$\mathbf{\Gamma} = (0,0), \quad \mathbf{M} = \frac{2\pi}{3a_0}(1,0), \quad \mathbf{K} = \frac{2\pi}{3a_0}(1, \frac{1}{\sqrt{3}}), \quad \mathbf{K}' = \frac{2\pi}{3a_0}(1, -\frac{1}{\sqrt{3}}). \tag{1.3}$$

It should be noted that **K** and **K**´ points are not related by reciprocal lattice vectors and therefore they are not equivalent.

1.2 Electronic structure of graphene

An isolated carbon atom has six electrons with the ground state electronic configuration of $1s^2 2s^2 2p^2$ [14]. The four electrons in the outer $2s$ and $2p$ orbitals are the valence electrons and can participate in the formation of chemical bonds with other atoms. A specific

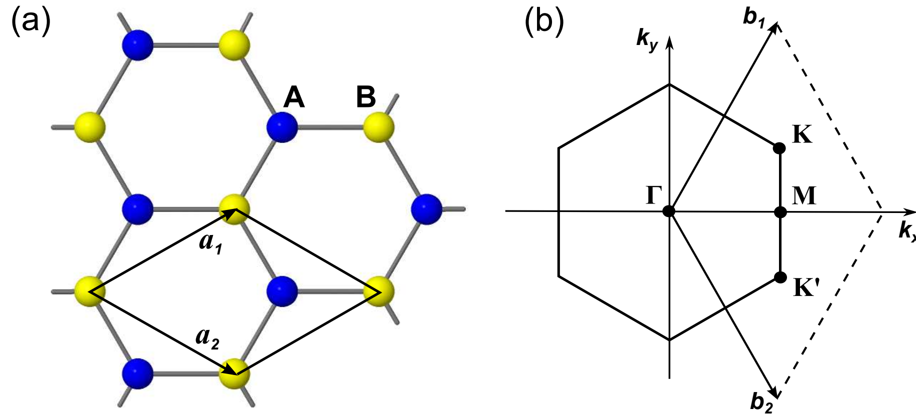

Figure 1.1: (a) Crystallographic structure of graphene. The primitive lattice vectors are defined as $\mathbf{a_1}$ and $\mathbf{a_2}$. Graphene lattice can be considered as a hexagonal lattice with two atoms per unit cell (atoms A and B). Alternatively it can be represented as a superposition of two sublattices shown in different colours. Each sublattice contains only atoms that can be translated by the primitive lattice vectors, i.e. only atoms A or only atoms B. (b) First Brillouin zone of graphene with the reciprocal lattice vectors defined as $\mathbf{b_1}$ and $\mathbf{b_2}$. High symmetry **k**-points are labeled as $\mathbf{\Gamma}$, **M**, **K** and **K´**.

binding of carbon atoms in a planar graphene lattice is a consequence of the sp^2 hybridization of carbon valence orbitals. That is, the $2s$ valence orbital mixes with the $2p_x$ and $2p_y$ ones forming three equivalent sp^2 hybrid orbitals lying in the xy plane. Three in-plane covalent bonds are then formed between a carbon atom and its three nearest neighbours by overlapping their sp^2 orbitals. The remaining $2p_z$ orbital, with an axis normal to the xy plane, can overlap with a neighbouring $2p_z$ orbital forming π bonding and π^* antibonding orbitals [14]. Overlap between $2p_z$ orbitals of neighbouring carbon atoms in graphene results in the formation of a delocalized π system. Most of the spectacular electronic properties of graphene are related to its π and π^* electron energy bands.

The form of the π energy bands in graphene was first derived by Wallace in 1947 within the approximation of tight-binding electrons [1]. Considering only interactions between

nearest neighbours in the lattice this will be

$$E(\mathbf{k}) = \pm t\sqrt{1 + 4\cos\left(\frac{\sqrt{3}}{2}a_0k_x/2\right)\cos\left(\frac{1}{2}a_0k_y\right) + 4\cos^2\left(\frac{1}{2}a_0k_y\right)}, \qquad (1.4)$$

where a_0 is the carbon-carbon distance and $t \approx 2.8$ eV is the nearest neighbour hopping energy. The minus sign applies to the lower π band, which is fully occupied, and the plus sign to the upper π^* band, which is empty. At the corners of the Brillouin zone of graphene (points **K** and **K´**) the π and π^* bands touch. Expanding Eq. 1.4 at **K**(**K´**) gives the linear dispersion relation

$$E(\mathbf{k}) = \pm\hbar v_{\mathrm{F}}|\mathbf{k}|, \qquad (1.5)$$

where $v_F = \sqrt{3}ta/(2\hbar) \approx 10^6\ ms^{-1}$ is the Fermi velocity [10]. Such linear dependence of the electron energy on the wave vector is specific for massless relativistic particles, such as photons or neutrinos. But the role of the speed of light in graphene is played by Fermi velocity v_F. Thus, graphene is a unique system, in which there are charged relativistic particles with zero rest mass, which do not have analogues among the known elementary particles. These quasiparticles are described by the Dirac equation, rather than the usual Schrödinger equation for nonrelativistic quantum particles, and are called massless Dirac fermions. The Dirac-like Hamiltonian can be written as

$$\hat{H} = i\hbar v_{\mathrm{F}}\sigma.\nabla, \qquad (1.6)$$

where σ is the Pauli matrices [15]. The corners of the Brillouin zone, where the band crossing occurs (points **K** and **K´**), are called Dirac points. The linear energy spectrum in graphene in the vicinity of **K** points has been observed directly by angle-resolved photoemission spectroscopy [16].

The unique nature of charge carriers in graphene reveals itself in the number of spectacular phenomena observed experimentally, such as anomalous quantum Hall effect [17], Klein

Paradox [18], and unusual Berry phase equal to π [5]. Remarkably, the quantum Hall effect in graphene can be observed at room temperature [19]. Linear dispersion graphene π bands close to the Dirac points result in a linear dependence of density of states on the energy. The density of states per unit cell can be written as [13]

$$\rho(E) = \frac{2A_C}{\pi\hbar^2}\frac{|E|}{v_{\mathrm{F}}^2}, \tag{1.7}$$

where A_C is the unit cell area. At the Dirac point the density of states is in principle zero. Despite that, graphene exhibits a minimum quantum conductivity of the order of $4e^2/h$ [5].

1.3 Production of graphene

The most commonly used method of graphene production is mechanical exfoliation that is simply rubbing a piece of crystalline graphite onto a smooth substrate surface [4, 20]. By this method quite large (up to 1 mm^2) graphene sheets with good electrical properties can be produced. One of the reasons of the success of the mechanical exfoliation technique is related to the fact that the graphene layers can be identified using an optical microscope [21, 22]. Interestingly, from an analysis of graphene optical images some reliable information on number of layers in exfoliating graphene sheets can be obtained [22].

The relative ease of graphene production by mechanical exfoliation has opened the field of two-dimensional material physics for many researchers. However, the technique produces randomly placed graphene sheets and is not reliable. For successful applications of graphene in electronics industry, techniques for large-area synthesis of graphene sheets are needed. Various surface science techniques for growth of graphene on metal and semiconductor substrates as well as chemical synthesis [23] have been considered.

Epitaxial growth of graphene on silicon carbide (SiC) substrates has been demonstrated [24,25] and is considered as a very promising technique for production of large graphene sheets with desired number of layers. There have also been significant achievements in deposition of graphene on large-area metallic substrates, such as Ni [26,27] and Cu [28] using chemical vapor deposition. Further, some techniques have been developed for transferring graphene from metals to insulating surfaces where electrical characterization of the films can be done. Obviously, recent progress on epitaxial growth provides a good basis for the development of large-scale graphene-based electronic devices. However, more work is surely needed to understand details of epitaxial growth of graphene on different substrates, to establish reliable methods of graphene production and to obtain solid results on effects of different substrates on electronic properties of graphene.

1.4 Doping of graphene

Graphene is a semimetal with zero overlap between conduction and valence bands. This means that at $T = 0$ its intrinsic charge carrier concentration is in principle zero. Carriers can be induced in graphene by thermal excitations, electric field effect or chemical doping. The effect of thermal excitation is usually small and at room temperatures can be neglected.

Charge carriers can be induced in graphene by application of an external electric field perpendicular to a graphene plane in the presence of an external source of electrons [4]. This is usually realized in graphene-based field effect transistors, where charge carriers are introduced by applying a gate voltage. Varying the gate voltage allows to continuously tune the concentration of carriers and switch between electron and hole conductivities. It was shown that for graphene on SiO_2 the concentration of charge carriers induced by this method can be as high as 10^{13} cm^{-2} [4].

Another way to create free charge carriers in graphene is chemical doping [29]. There

are two main mechanisms of chemical doping: surface transfer doping and substitutional doping. In the first case the charge carriers are introduced by the electron transfer between graphene and surface adsorbates or a substrate. It has been shown that graphene can be doped either n- or p-type by deposition of different metals and molecules [29]. The substrate induced doping has been observed for graphene on SiC [24, 25] and boron-nitride (BN) [30] substrates. Surface transfer doping is not destructive and is an effective method to control concentration of charge carriers in graphene. In some cases unintentional doping of graphene by residual chemical species or adsorbates from ambient air can also occur which is undesirable.

Substitutional doping occurs when a graphene carbon atom is substituted by another atom with a different number of valence electrons. This type of doping has been observed for B and N substitutional atoms and leads to p- and n-type conductivity respectively [31, 32]. However, incorporation of foreign atoms into graphene lattice can result in significant modification of graphene's electronic structure. For example, N-doped graphene behaves like an n-type doped semiconductor and exhibits low charge carrier mobility [32].

1.5 Effect of substrates on electronic transport in graphene

Graphene has been shown to be a material with extremely high mobility of charge carriers. Already in the first transport measurements carried out for graphene on SiO_2 values of charge carrier mobility were measured to be in excess of 15,000 $cm^2V^{-1}s^{-1}$ and were found to be almost independent of temperature [4]. This indicates that electrons and holes in graphene exhibit ballistic transport on submicrometer scale even at room temperatures. Furthermore, the observed temperature independence indicates that the carrier mobility is limited by scattering on defects [4]. It was shown that the main source of scattering is charged impurities in the SiO_2 substrate [33, 34]. Even if the charge impurity scattering is suppressed, for example by high dielectric constant liquids between graphene and oxide,

the mobility is still limited to about 40,000 $cm^2V^{-1}s^{-1}$ due to the scattering of charge carriers by remote interfacial phonons [34].

One of the ways to improve graphene transport quality is to create suspended graphene layers and thus eliminate the influence of the substrate. For suspended graphene the mobility values of several 10^6 $cm^2V^{-1}s^{-1}$ have been reported [9,35]. The fabrication of these systems is, however, extremely complicated and involves dangerous chemical species, such as hydrofluoric acid (HF). Thus, the scalable production of suspended graphene structures for applications in electronics is not realistic, at least at the present time.

Another technique to reduce the scattering of charge carriers in graphene is to use substrates with higher quality surfaces and higher energies of optical phonons than those of SiO_2. For example, in graphene deposited on boron nitride (BN) mobility values higher than 100,000 $cm^2V^{-1}s^{-1}$ can be achieved [36, 37]. The main drawbacks of the graphene-BN devices is a complicated fabrication procedure, unavoidable doping of graphene by BN and the current leakage through the BN substrates.

High mobilities for graphene epitaxially grown on the SiC(000$\bar{1}$) substrates has also been demonstrated. The mobility of charge carriers as high as 250,000 $cm^2V^{-1}s^{-1}$ has been reported for these systems [38]. In contrast, for graphene on the SiC(0001) surface the strong graphene to substrate interaction results in strong modification of the graphene electronic structure [39, 40]. In this case the linear dispersion of graphene π-bands does not occur. It has been shown, however, that the graphene-like electronic properties can be restored after intercalation of different chemical species into the graphene/SiC(0001) interface [41, 42].

Thus, there is strong requirement for substrates which, from one side, will not worsen the transport quality of graphene and, from the other side, are not very expensive and do not require sophisticated procedure for graphene layers deposition.

1.6 Band-gap engineering in graphene

High mobilities of charge carriers, observed at room temperature and for technologically relevant carrier densities of 1×10^{12} cm^{-2}, make graphene a promising material for applications in ultrafast electronics. However, the absence of an energy gap and the minimum quantum conductivity prevent the large on-off ratio of graphene-based transistors, which limits their potential application. This problem has been addressed in many investigations and a lot of progress was achieved in the field of band-gap engineering in graphene. There are several ways to open a band gap in graphene: 1) chemical modification of graphene lattice, 2) confinement of charge carriers in narrow graphene strips (nanoribbons) [43], and 3) application of perpendicular electric field to few-layer graphene (FLG) structures, such as bilayer or trilayer graphene [44, 45].

Chemical modification of graphene lattice involves changing the electronic configuration of carbon atoms from sp^2 to sp^3 by functionalization with other chemical species [46,47]. Following this route several graphene derivatives, which show insulating behavior, have been realized: namely, graphene oxide [48], graphane [46, 49, 50] and fluorographene (graphene monofluoride) [51–55]. In contrast to oxidized graphene layers, which are highly inhomogeneous, graphane and fluorographene are formed by ordered arrangement of hydrogen (in the case of graphane) and fluorine (in the case of fluorographene) atoms on both sides of the graphene layer. Such ordered graphene derivatives can in principle be considered as new two-dimensional (2D) crystals.

1.7 Goals of the present work

It is evident that the electronic properties of graphene can be significantly affected by interactions with an underlying substrate or different surface adsorbates. These effects can be unwanted or conversely can be used to modify graphene properties in a desirable way. Graphene can be doped with electrons and holes in high concentrations by various metals or gaseous and organic molecules physisorbed on its surface. Graphene reactions with some chemical species (eg., hydrogen and fluorine) offer promising techniques for bandgap engineering and the synthesis of novel graphene-related materials. Interactions with the underlying substrates can significantly deteriorate graphene transport quality or result in a doping of a graphene layer. Understanding the mechanisms of graphene interactions with substrates and adsorbates is necessary for controlling and manipulating graphene properties and construction of high quality graphene-based devices with the designed characteristics.

The aim of the present study is to investigate theoretically the interactions of graphene with different substrates and adsorbates using density functional methods. Specific aims are:

i) understanding the mechanisms of hydrogen and fluorine intercalation into the graphene/SiC interface and properties of the intercalated structures;

ii) determining the electronic properties of graphene on diamond substrates passivated with different chemical species, particularly H, F, and OH;

iii) to study and propose new routes for doping of fluorographene with electrons and holes by metallic and molecular adsorbates.

All calculations in the work have been carried out using local density functional theory as implemented in the Ab Initio Modelling Program (AIMPRO) code.

1.8 Thesis organisation

The Introduction is followed by four chapters describing the theoretical method used and original results obtained and concluding remarks.

Chapter 2 starts with a general introduction to the theoretical method used, then presents some details about the Ab Initio Modelling Program, which has been used for all the calculations in the study, and is ended with a description of results of some test calculations that were performed in order to justify the suitability of the method for calculations of graphene-related structures.

In Chapter 3 problems associated with epitaxial growth of graphene layers on SiC(0001) substrates, intercalation of different chemical species into the graphene/SiC interface, and decoupling of graphene layers from the substrates induced by heat-treatments in hydrogen ambient are considered. The results obtained in this chapter allows to propose a plausible explanation of the hydrogen-induced decoupling of graphene layers from the SiC(0001) substrates.

Chapter 4 describes results of calculation on electronic properties of single and bi-layer graphene on diamond substrates with (111) orientation and different types of surface passivation. Particularly, H-, F- and OH-passivated diamond surfaces have been considered.

In Chapter 5 results of calculations of structure and electronic properties of fluorographene are presented and compared with the results available in literature first. These are followed by the consideration of effects of various adsorbates, which include K, Li and Au metal atoms and F4-TCNQ. molecule, on electronic properties of fluorographene and discussion of suitability of these adsorbates for doping fluorographene with electrons and holes.

The thesis culminates with concluding remarks, in which all the results obtained in the entire work are discussed. Interesting questions, which have arisen in the course of the work, are briefly mentioned then and a perspective for calculation studies in the nearest future is given.

Chapter 2

Method

2.1 Many body problem

The establishment of quantum physics concepts and their further development provided us with unique tools for description of physical systems and investigation of their properties. In quantum mechanics, a system can be completely described by its *wave function*, which is a function of system parameters and, in general, time. Possible wave functions of a system and their evolution in space and time can be found by solving Schrödinger equation, which in the most general form can be written as[1]

$$\hat{H}\Psi = i\frac{\partial}{\partial t}\Psi, \tag{2.1}$$

where $\hat{H}$ is the Hamiltonian operator which corresponds to the total energy of a system, Ψ is the wave function and t is time. However, to determine most of the system properties it

[1]The system of atomic units will be used throughout this chapter (unless otherwise specified). In this system of units $\hbar$, e, m_e and $4\pi\epsilon_0$ are taken to be unity, where $\hbar$ is the reduced Planck constant, e and m_e are the charge and the mass of an electron, respectively, and ϵ_0 is the permittivity of vacuum.

is enough to describe the system in its stationary states. In this case the time dependence is omitted and the Schrödinger equation takes the following form:

$$\hat{H}\Psi_i = E_i\Psi_i, \tag{2.2}$$

where E_i is the total energy of the system i^{th} stationary state described by the wave function Ψ_i.

For a system of N_n atomic nuclei and N_e electrons and in the absence of external fields the Hamiltonian takes the form

$$\begin{aligned}\hat{H} &= \hat{T}_\mathrm{e} + \hat{T}_\mathrm{n} + \hat{V}_\text{e-e} + \hat{V}_\text{e-n} + \hat{V}_\text{n-n} \\ &= -\frac{1}{2}\sum_{i=1}^{N_e}\nabla_i^2 - \frac{1}{2M_\alpha}\sum_{\alpha=1}^{N_n}\nabla_\alpha^2 + \\ &\quad +\frac{1}{2}\sum_{\substack{i,j=1\\ i\neq j}}^{N_e}\frac{1}{|\mathbf{r}_i-\mathbf{r}_j|} - \sum_{i,\alpha=1}^{N_e,N_n}\frac{Z_\alpha}{|\mathbf{r}_i-\mathbf{R}_\alpha|} + \frac{1}{2}\sum_{\substack{\alpha,\beta=1\\ \alpha\neq\beta}}^{N_n}\frac{Z_\alpha Z_\beta}{|\mathbf{R}_\alpha-\mathbf{R}_\beta|},\end{aligned} \tag{2.3}$$

where M_α, Z_α and $\mathbf{R}_\alpha$ are the mass, the charge and the position of the αth nuclei and $\mathbf{r}_i$ is the position of the ith electron. The first two terms in the Equation 2.3 represent the kinetic energies of the electrons and nuclei respectively, and the subsequent terms describe the electron-electron, electron-nuclear, and inter-nuclear Coulomb interaction energies, respectively. The total wave function Ψ is a function of N_n nuclei coordinates, $\mathbf{R}_\alpha$, and N_e electron spatial and spin coordinated, $\mathbf{r}_i$ and s_i respectively,

$$\Psi \equiv \Psi(\mathbf{r}_1, s_1, \ldots, \mathbf{r}_{N_\mathrm{e}}, s_{N_\mathrm{e}}, \mathbf{R}_1, \ldots, \mathbf{R}_{N_\mathrm{n}}). \tag{2.4}$$

Thus, the wave function depends on $3N_\mathrm{n} + 4N_\mathrm{e}$ scalar variables. The analytical solution of the Schrödinger equation 2.2 with the wave function given by 2.4 has only been found

for a hydrogen atom. For systems consisting of a large number of atoms even a numerical solution of the Schrödinger equation became intractable. However, the complexity of the problem can be reduced by adopting several approximations.

2.2 Born-Oppenheimer approximation

Interactions between electrons and nuclei, caused by their electric charges, exert the same forces and momenta on both electrons and nuclei. In this case, since the mass of the electron is ~ 2000 times lighter than the mass of a proton or neutron, electrons must have much higher velocities than nuclei. Thus it is logical to assume that the electrons respond almost instantaneously to nuclear motion. In other words, the electrons will rapidly relax to the ground state configuration with respect to the instantaneous position of nuclei. It is therefore possible to separate electronic and nuclear motion, and look for a solution of the Schrödinger equation 2.2 in the form

$$\Psi(\mathbf{r}, \mathbf{R}) = \psi_{\mathbf{R}}(\mathbf{r})\phi(\mathbf{R}), \tag{2.5}$$

where $\psi_{\mathbf{R}}(\mathbf{r})$ and $\phi(\mathbf{R})$ are the separate electronic and nuclear wave functions. The variables $\mathbf{r}$ and $\mathbf{R}$ represent spatial coordinates of all electrons and nuclei respectively. This separation of electronic and nuclear motion is known as the *Born-Oppenheimer approximation* [56]. The subscription on ψ stresses the parametric dependence of the electronic wave function on the nuclei coordinates.

The Schrödinger equation can now be solved for the electronic wave function only, considering the nuclei to be stationary:

$$\hat{H}_{\mathrm{e}}\psi_{\mathbf{R}}(\mathbf{r}) = E_{\mathrm{e}}(\mathbf{R})\psi_{\mathbf{R}}(\mathbf{r}), \tag{2.6}$$

with Hamiltonian

$$\begin{aligned}\hat{H}_{\text{e}} &= \hat{T}_{\text{e}} + \hat{V}_{\text{e-e}} + \hat{V}_{\text{e-n}} + \\ &= -\frac{1}{2}\sum_{i=1}^{N_e}\nabla_i^2 + \frac{1}{2}\sum_{\substack{i,j=1\\ i\neq j}}^{N_{\text{e}}}\frac{1}{|\mathbf{r}_i - \mathbf{r}_j|} - \sum_{i,\alpha=1}^{N_{\text{e}},N_{\text{n}}}\frac{Z_\alpha}{|\mathbf{r}_i - \mathbf{R}_\alpha|},\end{aligned} \tag{2.7}$$

Subsequently, in the equation for the nuclei motion the electronic energy $E_{\text{e}}(\mathbf{R})$ enters as a potential:

$$\left[\hat{T}_{\text{n}} + \hat{V}_{\text{n-n}} + E_{\text{e}}(\mathbf{R})\right]\phi(\mathbf{R}) = E_{\text{tot}}\phi(\mathbf{R}), \tag{2.8}$$

where E_{tot} is the total energy of the whole system.

Within *ab initio* schemes the nuclei motion is usually neglected, however, their positions can be varied in order to find the ground state of the whole system. Therefore, from now on we will only consider the electronic problem 2.6.

2.3 Variational principle

In most of the cases the exact form of the many electron wave function is not known and an approximation has to be made. In order to find the closest approach to the true solution of the Schrödinger equation 2.6 for a system ground-state one can use the variational method. In this method the ground-state wave function Ψ_0 is approximated by a carefully chosen subspace $\{\phi_1, \cdots, \phi_M\}$ of Hilbert space:

$$\Psi_0 \approx \Psi_{\text{app}} = \sum_i^M c_i\phi_i. \tag{2.9}$$

Taking into account that the expectation value for the total energy E is a functional of the wave function, the approximate total energy is

$$E_{\text{app}} = E[\Psi_{\text{app}}] = \frac{\sum_{i,j=1}^{M} c_i^* c_j H_{ij}}{\sum_{i,j=1}^{M} c_i^* c_j S_{ij}}, \tag{2.10}$$

where $H_{ij} = \langle \phi_i | \hat{H} | \phi_j \rangle$ and $S_{ij} = \langle \phi_i | \phi_j \rangle$ are referred to as Hamiltonian and overlap matrix elements respectively. Stationary states can then be found from the condition that the derivative of E_{app} with respect to c_i vanishes, leading to

$$\sum_{j=1}^{M} (H_{ij} - E_{\text{app}} S_{ij}) c_j = 0 \quad \text{for} \quad i = 1, \ldots, M, \tag{2.11}$$

which can be generalized to a matrix eigenvalue equation with the form

$$\hat{H} \cdot \mathbf{c} = E_{app} S \cdot \mathbf{c}. \tag{2.12}$$

It can be proved that the energy E_{app} calculated from an approximate wave function ψ_{app} is an upper bound for the true value of the ground-state energy E_0. Full minimization of the functional $E[\Psi]$ with respect to the basis functions will give the true ground state energy E_0. That is

$$E_0 = \min_{\Psi} E\left[\Psi\right]. \tag{2.13}$$

This is known as the Rayleigh-Ritz variational principle [57, 58]. The variational method is widely used in electronic structure calculations to determine the ground-state properties of a system.

2.4 Density Functional Theory

Density functional theory (DFT) was introduced in 1964 by Hohenberg and Kohn who showed that the ground state of the system is uniquely determined by the electronic charge density $n(\mathbf{r})$ [59, 60].

Theorem 2.4.1 (First Hohenberg-Kohn theorem)**.** *The external potential is described, to within a trivial additive constant, by the electron density n(***r***).*

The implication of this theorem is the following. In the electronic Hamiltonian 2.7 the terms $\hat{T}_{\text{e-e}}$ and $\hat{V}_{\text{e-e}}$ are the same for all N-electron systems, and the last term, arising form the electron-nuclear interaction, can be treated as a static external potential $V_{\text{ext}}(\mathbf{r})$. Therefore, the Hamiltonian, and hence the ground-state wave function Ψ_0 are completely determined by N and $V_{\text{ext}}(\mathbf{r})$. It follows then that if the electron ground state density $n_0(\mathbf{r})$ uniquely defines $V_{\text{ext}}(\mathbf{r})$ and since $N = \int d\mathbf{r} n_0(\mathbf{r})$ it should also define all the ground-state properties of the system. Hohenberg and Kohn wrote the expression for the total energy as

$$E[n] = F[n] + \int v_{\text{ext}}(\mathbf{r}) n(\mathbf{r}) d\mathbf{r}, \tag{2.14}$$

where the functional $F[n]$ is universal (system-independent), and accounts for electronic kinetic energy, electron correlation and exchange interactions. External potential v_{ext} includes the ion-electron interaction and other external fields.

Theorem 2.4.2 (Second Hohenberg-Kohn theorem)**.** *For a trial density* $\tilde{n}(\mathbf{r})$ *such that* $\tilde{n}(\mathbf{r}) \geq 0$ *and* $\int \tilde{n}(\mathbf{r}) d\mathbf{r} = N$*,*

$$E[\tilde{n}] \geq E_0. \tag{2.15}$$

Minimizing the functional $E[\tilde{n}]$ the ground-state charge density and hence E_0 can be found:

$$E_0 = \min_{\tilde{n}} E[\tilde{n}]. \tag{2.16}$$

This is an implementation of the energy variational principle 2.16. Adopting the charge density as the variational parameter vastly simplifies the computational procedure, although no approximations are made. Instead of dealing with the many electron wave function which depends on at least $3N$ variables (coordinates for each electron) for a system of N electrons, DFT uses the charge density which is only a function of three variables, x, y and z.

2.4.1 Kohn-Sham equations

In the above shown DFT formalism it remains to define the form of the universal functional $F[n]$. For a system of interacting electrons the explicit form of this functional is unknown. Kohn and Sham proposed to treat the problem for a fictitious system of non-interacting electrons by adding the appropriate auxiliary external potential so that the charge density is exactly the same as that in the interacting system [60],

$$\sum_{\lambda} |\psi_{\lambda}(\mathbf{r})|^2 = n(\mathbf{r}), \tag{2.17}$$

where the summation is over the all occupied electron states ψ_{λ} of the non-interacting system. The kinetic energy for this system is given exactly:

$$T_s[n] = \sum_{\lambda} \left\langle \psi_{\lambda} \left| -\frac{1}{2}\nabla^2 \right| \psi_{\lambda} \right\rangle. \tag{2.18}$$

The total energy can then be written as

$$E = T_s[n] + \frac{1}{2}\int \frac{n(\mathbf{r})n(\mathbf{r}')}{|\mathbf{r}-\mathbf{r}'|} d\mathbf{r}d\mathbf{r}' + \int v_{\text{ext}}(\mathbf{r})n(\mathbf{r})d\mathbf{r} + E_{\text{xc}}[n], \tag{2.19}$$

where $E_{\text{xc}}[n]$ includes exchange and correlation energies and the difference between the kinetic energies of the interacting and non-interacting systems. The remarkable result of this approach is that the first three terms in the Equation 2.19 can be dealt with simplicity, while the unknown $E_{\text{xc}}[n]$ term is a small part of the total energy and can be approximated surprisingly well.

The functions ψ_λ and hence the ground state charge density can be obtained from the self-consistent solution of the following equations:

$$-\frac{1}{2}\nabla^2\psi_\lambda(\mathbf{r}) + v_{\text{eff}}(\mathbf{r})\psi_\lambda(\mathbf{r}) = \epsilon_\lambda\psi_\lambda(\mathbf{r}) \tag{2.20}$$

$$v_{\text{eff}}(\mathbf{r}) = v_{\text{ext}}(\mathbf{r}) + \int \frac{n(\mathbf{r}')d\mathbf{r}'}{|\mathbf{r}-\mathbf{r}'|} + \frac{\delta E_{\text{xc}}}{\delta n(\mathbf{r})} \tag{2.21}$$

$$n(\mathbf{r}) = \sum_\lambda |\psi_\lambda(\mathbf{r})|^2 \tag{2.22}$$

These equations are known as *Kohn-Sham equations*. It is worth noting that the functions ψ_λ are only used to construct the charge density and should not be treated as one-electron wave functions.

2.4.2 The exchange-correlation functional

The remarkable result of the DFT is that all the energy terms that cannot be calculated explicitly are accounted in one uniform functional $E_{\text{xc}}[n]$ which depends only on the electron density. Thus the accuracy of the ground state energy and charge density calculations depends on the correctness of the $E_{\text{xc}}[n]$ approximation. There are two main approaches that are widely used in today's electronic structure calculations: Local Density Approximation (LDA) [60, 61] and Generalised Gradient Approximation (GGA) [62–64].

In the LDA the exchange-correlation energy is assumed to be local and for any infinitesimal volume in space $d\mathbf{r}$ takes the value it would have for the homogeneous electron gas with the same charge density.

$$E_{\text{xc}}[n] = \int n(\mathbf{r})\epsilon_{\text{xc}}(n)d\mathbf{r}, \tag{2.23}$$

where $\epsilon_{\text{xc}}[n(\mathbf{r})]$ is the exchange-correlation energy per electron in a homogeneous electron gas of density $n(\mathbf{r})$. A generalization of LDA for a non-zero spin systems is local spin-density approximation (LSDA) [65]. In this case the spin-up $n_\uparrow$ and spin-down $n_\downarrow$ charge densities are considered. Usually the exchange and correlation effects are treated separately, so that

$$E_{\text{xc}}[n_\uparrow, n_\downarrow] = E_{\text{x}}[n_\uparrow, n_\downarrow] + E_{\text{c}}[n_\uparrow, n_\downarrow]. \tag{2.24}$$

For the homogeneous electron gas the exchange part can be obtained analytically from the Hartree-Fock theory:

$$E_{\text{x}}[n_\uparrow, n_\downarrow] = -\frac{3}{2}\left(\frac{3}{4\pi}\right)^{1/3}\left(n_\uparrow^{4/3} + n_\downarrow^{4/3}\right). \tag{2.25}$$

The correlation part is more complex. In the high density limit it is evaluated from the many body perturbation theory [61], while for low charge densities the evaluation obtained from Green function quantum Monte Carlo calculations is used [66–68]. The numerical results for both density limits are then fitted to a simple parametrized functional form. Several parametrisations to E_{c} have been proposed. The most commonly used are those of Perdew and Zunger (PZ) [61], Vosko et al. (VWN) [67] and Perdew and Wang [64].

Despite the simplicity of the approximation the LDA was shown to produce surprisingly accurate results in lots of cases. It was successfully applied to study properties of bulk semiconductors and the calculated values for lattice constants, bulk modulus and phonon spectra agreed exceptionally well with the experimentally determined ones [69–71]. It was also proven to be reasonably accurate for determination of equilibrium structures and vibrational frequencies of molecules [72–74]. However, the LDA generally significantly overestimates the binding energies of molecules and tends to underestimate atomic ground state energies and ionization energies [75, 76].

The generalised gradient approximation was developed as an attempt to improve the LDA by including the dependence of E_{xc} on the gradient of the charge density, and hence taking into account the inhomogeneity of the electron gas. This approach was shown to give more accurate descriptions of atomic and molecular systems than those by LDA [75, 76]. However, in applications to bulk solids, where valence electron densities vary rather slowly, the GGA generally does not show an improvement over the LDA [76]. The general trend is that the LDA tends to underestimate bond lengths and hence to overestimate bulk moduli while the GGA shows an opposite behaviour [75].

Since almost all calculations in the present work were performed for investigation of interactions between two surfaces (graphene and substrate) or between adsorbates and a surface it was crucial to have an appropriate description of the van der Waals (vdW) interactions [77, 78]. These types of interactions are intrinsically a non-local correlation phenomena and therefore cannot be correctly described by LDA or GGA due to the local character of the approximation to the exchange and correlation potential [79]. Nevertheless, the LDA was shown to produce in some cases surprisingly good results due to the cancellation of errors in the exchange and correlation energies [79, 80]. Particularly, the LDA predicts the interlayer binding in graphite and other layered solids and gives their bulk properties in a reasonable agreement with the experimental results [79, 81]. In contrast, the GGA fails to describe the binding between the carbon layers in graphite [79, 81].

The proper representation of the vdW interactions can be obtained from quantum Monte Carlo (QMC) [82–84] or random-phase approximation (RPA) [79, 85, 86] calculations. These methods are however extremely computationally expensive and, at present, are only suitable for studying systems of a few atoms. Therefore several other approaches to treat vdW interactions have been proposed, mainly non-local van der Waals density functionals [87–89] and semiempirical dispersion correction schemes (DFT-D) [90–92]. The latter ones became very popular because they can be easily implemented in the available DFT programs with almost no additional computational cost. The DFT-D methods are based on the addition of a pairwise interatomic C_6R^{-6} correction term to the DFT energy, where R is the distance between a pair of atoms and the C_6 parameters are obtained by fitting to the experimental data. Dispersion corrections are usually added to GGA functionals and were shown to give an improved accuracy for description of noncovalently bound molecular complexes and chemical reactions when compared with standard GGA or LDA functionals [93]. However, when applied to layered solids the GGA+D methods produce errors in interlayer separations and binding energies similar to those from LDA [79]. Recently, Tkatchenko and Scheffler [94] proposed a promising nonempirical method to obtain C_6 coefficients, which produced very accurate results for a large set of tested molecules and also for hexagonal boron nitride, which is a layered solid.

In the present work all the calculations were performed within LDA. This approach was shown to well reproduce the electronic and structural properties of the modelled materials: graphene, diamond and SiC. The calculated bond lengths in these materials was found to be within less than 1% error from the experimental values.

2.5 Pseudopotentials

It is well known that binding of atoms into molecules or solids are governed by their valence electrons. The core electrons are tightly bound to the nucleus and are relatively

unaffected by the chemical environment of an atom. It is therefor reasonable to incorporate the effects of the core electrons into the effective screened nuclear potential, *pseudopotential*, felt by the valence electrons [95–98]. This allows to effectively eliminate the core states from the calculations, while keeping precision on the description of the valence states. The use of pseudopotentials has several considerable advantages. Firstly, in all electron calculations, in order to maintain orthogonality with the localized core electrons states the valence electrons wave functions must rapidly oscillate in the core region and therefore require a large number of basis functions for an accurate description. In the pseudopotential approach the valence electrons wave functions are replaced by pseudo-wave functions which are much smoother in the core region and easier to approximate. This considerably reduces computational efforts and consequently systems with larger number of atoms can be modelled. Secondly, the exclusion of the core states results in significant lowering in the magnitude of the total energy therefore reduces errors when comparing similar systems. And thirdly, relativistic effects, which became important for heavy elements, can be included into the pseudopotentials, which are then called relativistic pseudopotentials [99]. The valence electrons can then continue to be treated non-relativistically.

There is no unique method to construct pseudopotentials. However, several requirements for pseudopotentials are generally imposed [100]:

1. The real and pseudo valence eigenvalues are equal for a given atomic configuration;
2. Beyond a certain cut-off radius, r_{c}, the real and pseudo atomic wave functions are identical;
3. The integrated real and pseudo charge densities are the same for $r > r_{\mathrm{c}}$ for each valence state (*norm conservation*);
4. The logarithmic derivatives and the first energy derivatives of the real and pseudo wave functions agree for $r > r_{\mathrm{c}}$.

Pseudopotentials that satisfy the above conditions are called the norm-conserving pseudopotentials [100]. The most commonly used forms of norm-conserving pseudopotentials are those of Bachelet, Hamann and Schlüter (BHS) [101], and Troullier and Martins (TM) [102].

A practical pseudopotential has to be *transferable*. This means that it has to be capable to reproduce the properties of the valence electrons of an atom in different chemical environments. For example, a pseudopotential for the carbon atom should give accurate results when used in graphene or diamond. The transferability of pseudopotentials is to some extent ensured by the third and fourth conditions from those listed above [100]. The third condition, the norm conservation constraint, guarantees that an identical electrostatic potential is produced outside the cut-off radius for pseudo and real charge distributions. The fourth condition gurantees, that the scattering properties of real ion cores are reproduced with minimal errors when the chemical environment of an atom is changed [100]. Typically, reducing the cut-off radius improves the tranferability of the pseudopotential, since the corresponding pseudo-wave function is getting closer to the true all electron wave function. Increasing cut-off radius allows to make pseudopotential smoother (*softer*) and to improve convergence of calculations, however, this can result in the loss of accuracy [103]. Quite recently a new scheme for the construction of *ultrasoft* pseudopotential with good transferability was proposed by Vanderbilt *et al.* [104]. In these pseudopotentials the norm conservation constraint is relaxed giving a much more slowly varying charge density that can be treated with a smaller set of basis functions.

All the calculations in this thesis were performed using the relativistic, separable and dual-space Gaussian pseudopotentials of Hartwigsen, Goedecker, and Hutter (HGH) [105]. The advantage of using the HGH pseudopotentials is that all integrals involving matrix elements between Gaussian orbitals can be treated analytically.

2.6 The AIMPRO implementation of DFT

All the calculations presented in this thesis were performed using the Ab-initio Modelling Program (AIMPRO) [106–108]. The important feature of the AIMPRO code is that it uses a real space Gaussian type basis set. The code allows us to perform both supercell and cluster calculations. All the problems here were treated within the supercell method which will be discussed in more detail.

2.6.1 The supercell method

In the supercell method the periodic boundary conditions are applied to a unit cell which contains a modelled structure. This method is ideal for modelling bulk materials, especially crystalline solids, as they naturally obey a periodic condition. It allows to calculate specific property of periodic structures as the dependence of electronic energies on the wave vector. The supercell method can also be used for modelling surfaces and molecules, and it was implemented in most of the calculations presented in this thesis. For modelling surfaces one of the three lattice vectors of the unit cell are considerably extended in length, while the number of atoms and their positions are kept the same. Thus a volume free of atoms is created. A layer of vacuum then appears between regions of material and their repeated images in this direction. The material repeats as usual in the two remaining directions. Thus, slabs of a material with infinite planar extent are created, bounded by the surfaces to be modelled and separated by layers of vacuum. It should be ensured that the width of the vacuum layers is enough to minimize any interaction between surfaces of neighbouring slabs. For modelling molecules the procedure is in principle the same. A molecule should be placed in a unit cell (box) which has dimensions large enough to avoid any interaction between the molecule and its own repeated images.

2.6.2 Basis functions

In the supercell method the wave functions have to obey periodic boundary conditions. Therefore the Kohn-Sham orbitals $\psi_{\mathbf{k}\lambda}(\mathbf{r})$ are expanded using a set of Bloch basis functions $B_{\mathbf{k}i}(\mathbf{r})$ as

$$\psi_{\mathbf{k}\lambda}(\mathbf{r}) = \sum_i c_{\lambda\mathbf{k},i} B_{\mathbf{k}i}(\mathbf{r}), \tag{2.26}$$

In AIMPRO a basis set of localized orbitals $\phi_i(\mathbf{r})$ is used, so that $B_{\mathbf{k}i}(\mathbf{r})$ is defined as

$$B_{\mathbf{k}i}(\mathbf{r}) = \frac{1}{\sqrt{N_\mathrm{L}}} \sum_n^{N_\mathrm{L}} \phi_{\mathbf{L}_n,i}(\mathbf{r} - \mathbf{L}_n)\, e^{\mathrm{i}\mathbf{k}\cdot\mathbf{L}_n}, \tag{2.27}$$

where $\phi_{\mathbf{L}_n,i}$ refers to the i-th localized orbital in the unit cell described by the lattice translation vector $\mathbf{L}_n$ and the sum is over all the N_L vectors $\mathbf{L}_n$. The localized orbitals are Cartesian Gaussian functions centred at the atomic sites $\mathbf{R}_i$, which are given by

$$\phi_i(\mathbf{r}) = (x - R_{ix})^{l_1}(y - R_{iy})^{l_2}(z - R_{iz})^{l_3} \times e^{-a_i(\mathbf{r}-\mathbf{R}_i)^2}, \tag{2.28}$$

where the choice of $l_i \geq 0$ defines the orbital type. Setting $\sum_i l_i = 0$ gives s-orbital, $\sum_i l_i = 1$ gives p-orbitals and setting $\sum_i l_i = 2$ gives a combination of five d- and one s-type orbitals.

The charge density can be obtained as

$$n(\mathbf{r}) = \sum_{i,j,\mathbf{k}} b_{ij}(\mathbf{k})\, B^*_{\mathbf{k}i}(\mathbf{r})\, B_{\mathbf{k}j}(\mathbf{r}), \tag{2.29}$$

where $b_{ij}(\mathbf{k})$ is the density matrix:

$$b_{ij}(\mathbf{k}) = \sum_\lambda f_{\mathbf{k}\lambda}\, c^*_{\mathbf{k}\lambda,i}\, c_{\mathbf{k}\lambda,j}, \tag{2.30}$$

where $f_{\mathbf{k}\lambda}$ is the occupancy of the $\mathbf{k}\lambda$ state.

The main advantage of using Gaussian functions basis is that it is very efficient. Compared to plane waves expansion much fewer localised fitting functions are needed for accurate description of atoms [109]. The drawbacks of the method is that Gaussian functions are not orthogonal, and using too many can result in overcompleteness of the basis set, i.e. very similar wave functions can be constructed from different combinations of the basis functions, which can introduce numerical instability into the calculation [109].

2.6.3 Basis functions in reciprocal space

Although a real-space basis is used to construct the Kohn-Sham orbitals the charge density in the supercell AIMPRO calculations is expanded in a plane wave basis:

$$\tilde{n}(\mathbf{r}) = \sum_{\mathbf{g}} A_{\mathbf{g}} \exp(i\mathbf{g} \cdot \mathbf{r}), \tag{2.31}$$

where the sum is taken over a discrete grid of reciprocal lattice vectors **g** inside a sphere of radius g_{cut} defined by a cut-off energy

$$E_{\text{cut}} = \frac{1}{2} g_{\text{cut}}^2. \tag{2.32}$$

This allows more efficient calculations of functionals of $n(\mathbf{r})$ in the reciprocal space. The number of plane waves and thus the accuracy of the charge density expansion is defined by E_{cut}. In calculations the cut-off energy is increased until the convergence of the total energy is achieved.

2.6.4 Sampling of the Brillouin zone

In the supercell approach, in order to obtain physical quantities, such as charge density or total energy, integration over the Brillouin zone (BZ) has to be performed. An integrand function $f(\mathbf{k})$, in general, does not have a simple analytical form. Instead of integrating this function numerically over a dense mesh, it is possible to find its average value $\bar{f}$ by sampling over a set of selected **k**-points:

$$\bar{f} = \frac{\Omega}{(2\pi)^3} \int f(\mathbf{k})\, d\mathbf{k} \approx \frac{1}{N} \sum_{i}^{N} f(\mathbf{k}_i), \tag{2.33}$$

where $(2\pi)^3/\Omega$ is the volume of the Brillouin zone. The accuracy of such description clearly depends on the number and choice of **k**-points. Monkhorst and Pack (MP) proposed simple and reliable scheme for **k**-points sampling [110, 111]. In this method the function f is calculated over $N_1 \times N_2 \times N_3$ grid of points in reciprocal space, defined as

$$\mathbf{k}(n_1, n_2, n_3) = \frac{2n_1 - N_1 - 1}{2N_1}\mathbf{b}_1 + \frac{2n_2 - N_2 - 1}{2N_2}\mathbf{b}_2 + \frac{2n_3 - N_3 - 1}{2N_3}\mathbf{b}_3, \tag{2.34}$$

where $\mathbf{b}_1$, $\mathbf{b}_2$ and $\mathbf{b}_1$ are the primitive translation vectors of the reciprocal lattice, N_1, N_2 and N_3 are integers ≥ 1 and n_1, n_2, n_3 are integers from 1 to N_1, N_2 and N_3, respectively. In high symmetry systems only m **k**-points from the irreducible part of the Brillouin zone (IBZ) are taken. Each point is then weighted with a factor ω_i. It is convenient to define ω_i as the ratio of the number of **k**-points that are related by symmetry to the i-th **k**-point in the IBZ (including the i-th **k**-point itself) to the total number of **k**-points N. The average $\bar{f}$ can then be calculated as

$$\bar{f} \approx \sum_{i}^{m} \omega_i f(\mathbf{k}_i). \tag{2.35}$$

2.7 Modelling graphene

This section aims to show the suitability of the theoretical approach for modelling graphene structural and electronic properties and consider possible difficulties in calculations.

For modelling graphene the supercell method has been used. The graphene lattice structure was described before in the Introduction (see Fig. 1.1). The unit cell of graphene has two atoms, and lets assume that they are lying in xy-plane. Thus, repeating the unit cell in xy-plane by applying the periodic boundary conditions results in the infinite and perfect graphene layer. Since graphene is basically a surface a layer of vacuum has to be included above graphene (in z-direction) in the supercell method. In all calculations the local density approximation and Hartwigsen-Goedecker-Hutter (HGH) pseudopotentials were used. Extended tests have been performed to find a set of the parameters involved in modelling that gives the best correspondence of calculated graphene properties, mainly bond length and electronic band structure, to those known from experimental studies and leads to the lowest calculated energy. The following set of parameters has been adopted:

1. The $pdpp$ basis set was adopted to represent valence states of graphene carbon atoms. In the given notation the letters are the orbital symbols. The number of symbols is equal to the number of different exponents in the basis. Each symbol corresponds to a set of Cartasian Gaussian functions of the same exponent for all values of angular momenta, l, up to maximum defined by the orbital symbol. That is, l = 0, 1 for p which gives 4 functions, and l = 0, 1, 2 for d which gives 10 functions (see section 2.6.2). Thus, $pdpp$ basis set corresponds to 22 independent functions of s-, p- and d-type with 4 different exponents.

2. The cut-off energy of 200 Ha for a plane-wave expansion of the charge density and potential terms was found to be enough to avoid the further dependence of the total energy on this parameter.

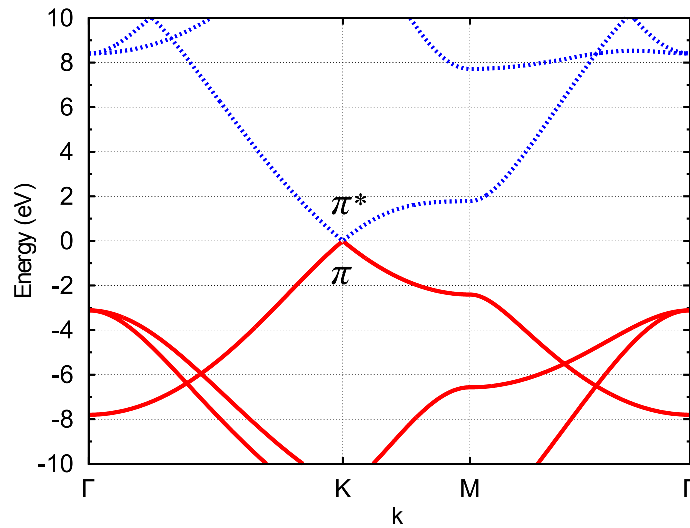

Figure 2.1: Calculated electronic band structure of graphene. Red solid lines represent occupied states, while blue dashed lines represent empty states. The zero of the energy scale is set to the Fermi level.

3. It was found that the metallic filling of the electron states, i.e. number of electrons at each **k**-point can differ, leads to a faster energy convergence compared to the filling with Fermi-Dirac statistics.

4. A layer of vacuum of ∼7 Å was found to be sufficient to avoid the interaction between graphene and its own repeated images.

The choice of the **k**-points grid for the Brillouin zone (BZ) integration will be discussed in section 2.7.1. The lattice constant of graphene obtained from the converged calculations with the above set of parameters is 2.45 Å, which is less than 0.5% from the experimental value of 2.46 Å.

The band structure calculated for a graphene unit cell is shown in Fig. 2.1. As expected, conduction and valence bands touch at the **K** point of the BZ (the Dirac point) and the linear dispersion of graphene π-bands near the **K** point can be seen. The Fermi level crosses the Dirac point separating the filled and occupied states.

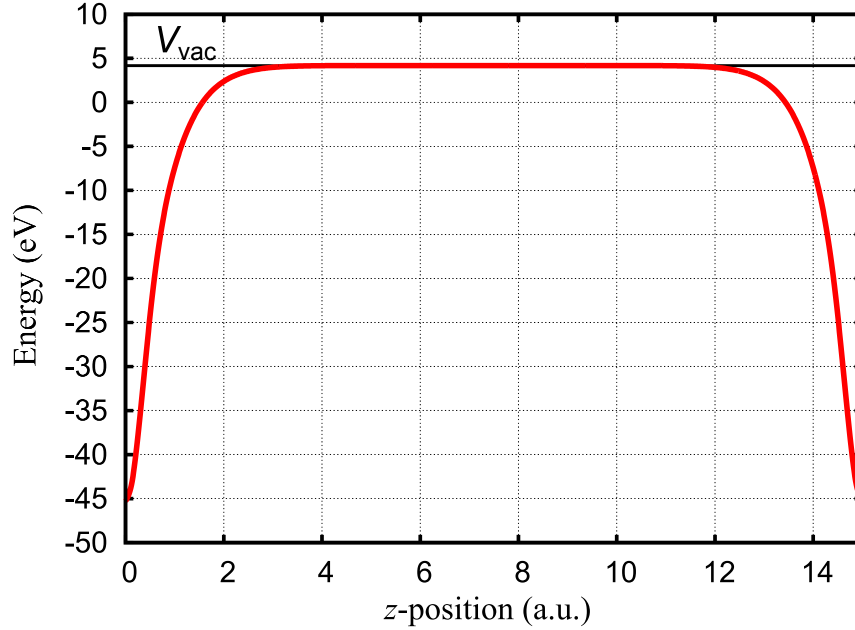

Figure 2.2: Plot of the xy-plane-averaged electrostatic potential as a function of the position along the z axis for a graphene layer. Graphene carbon atoms was positioned at $z = 0$. The black solid line defines the position of the vacuum level.

In order to calculate the work function of graphene, which is the difference between the electrostatic potential in the vacuum, V_{vac}, and the Fermi level in the material, it is necessary to determine the value of V_{vac}. This can be done by calculating the xy-plane-averaged electrostatic potential as a function of the position along the z axis (Fig. 2.2). The flat part of the potential in Fig. 2.2 correspond to the electrostatic potential in the vacuum region. The work function of graphene was found to be 4.48 eV, which is very close to the values obtained in several experimental works of 4.5-4.6 eV.

2.7.1 Choice of k-points for the graphene Brillouin zone sampling

In AIMPRO a slightly modified version of the MP sampling scheme (equation 2.34) for defining a grid of the k-points is used:

$$\mathbf{k}(n_1, n_2, n_3) = \frac{n_1 + S_1}{N_1}\mathbf{b_1} + \frac{n_2 + S_2}{N_2}\mathbf{b_2} + \frac{n_3 + S_3}{N_3}\mathbf{b_3} \tag{2.36}$$

where $\mathbf{b_1}$, $\mathbf{b_2}$, $\mathbf{b_3}$ are the primitive translation vectors of the reciprocal lattice, N_1, N_2, N_3 are the integers that define the number of $\mathbf{k}$-points in each direction, n_1, n_2, n_3 are the integers from 1 to N_1, N_2 and N_3, respectively. S_1, S_2 and S_3 define the initial shift, which allows changing the coordinates of the $\mathbf{k}$-points included. Usually the shift is defined as (0.5; 0.5; 0.5). This results in even numbered grids that are equivalent to that obtained from equation 2.34. However, the odd numbered grids are shifted compared to those generated by equation 2.34 in order to avoid inclusion of the $\mathbf{\Gamma}$ point into the sampling.

Figure. 2.3 shows convergence tests for the total energy and the Fermi level depending on the choice of the sampling over the BZ. The totally converged values are chosen as the zero energy level. Clearly, for the initial shift of 0.5, in general, the errors are smaller and the convergence is faster. However, for the initial shift equal to 0 and for all values of N which are multiples of 3 the calculated positions of the Fermi level exactly coincide with the Dirac point. These grids include the $\mathbf{K}$ point with coordinates $(1/3\mathbf{b_1}; 1/3\mathbf{b_2}; 0)$ into the sampling. It is important to note that the biggest error for the total energy calculations is less than 20 meV, while for the Fermi energy it is about 1.2 eV. Typically the $\mathbf{k}$-points mesh of $10 \times 10 \times 1$ or close to this within the first Brillouin zone of graphene is used, so an error in the Fermi energy determination can be several hundreds meV. Including the $\mathbf{K}$ point into the sampling will give a slightly bigger error in the total energy of the order of several meV, while the error for the Fermi energy will be close to 0.

The problem with the Fermi energy convergence can be explained by the facts that there is no overlap between conduction and valence bands and the energy near the $\mathbf{K}$-point changes quite rapid with the changes of the wave vector. This implies that for a good description of the region near the Dirac point and for the accurate determination of the Fermi energy a lot of $\mathbf{k}$-points have to be included. The problem is that for the most *ab*

initio codes in the standard procedure, which is used for generation of the $\mathbf{k}$-points for sampling, the $\mathbf{k}$-points are put uniformly into the whole Brillouin zone. So, even if a very high mesh of $\mathbf{k}$-points is defined, only a few of them fall into the small region of interest, that usually is not enough to calculate the Fermi energy correctly. The problem with the Fermi energy convergence concerns not only graphene, it is a general problem for materials in which the energy bands, which are close to the Fermi level, change rapidly in the narrow regions of the BZ.

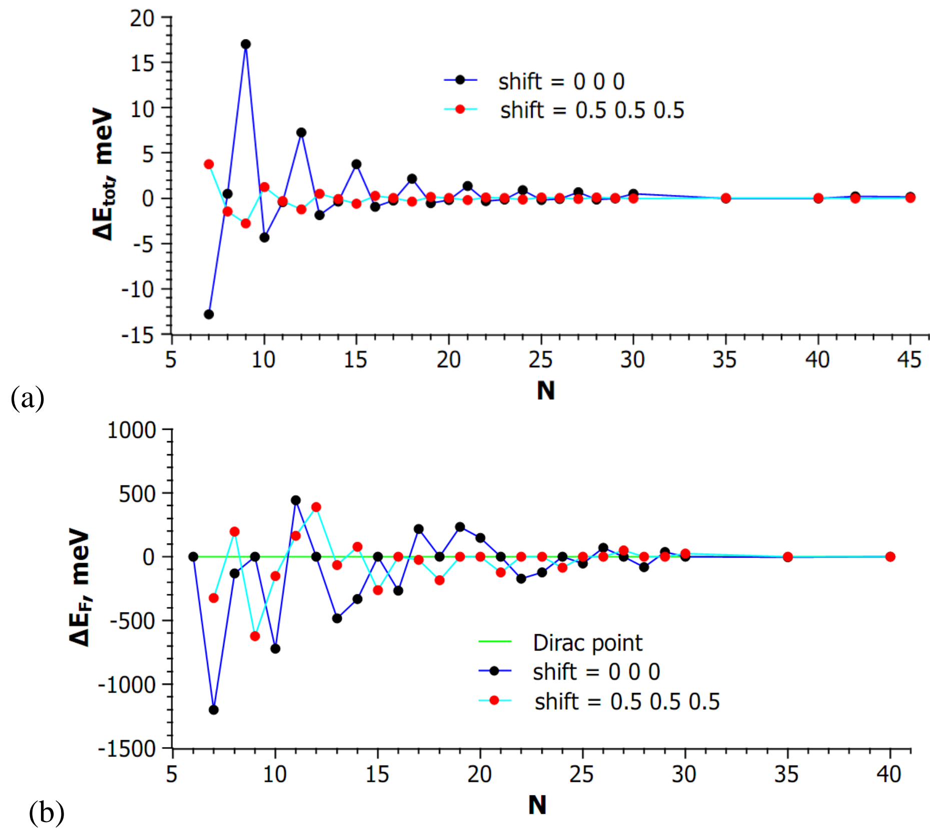

Figure 2.3: Convergence of (a) the total energy (b) the Fermi level with the number of $\mathbf{k}$-points $(N \times N \times 1)$ for the Brillouin zone sampling for band structure calculations. The red and black circles are for the initial shifts of (0.5;0.5;0.5) and (0;0;0) respectively. The lines are plotted as guides for eyes.

Chapter 3

Intercalation of hydrogen and fluorine into graphene/SiC(0001) interface

3.1 Introduction

Epitaxial growth of graphene on SiC substrates is considered as one of the most promising ways for the production of large area homogeneous graphene layers [24,39,112,113]. Annealing hexagonal SiC at elevated temperatures results in the loss of Si atoms from the surface, while the remaining C atoms rearrange in a graphene honeycomb structure. Single-layer or few-layers graphene (SLG or FLG) can be grown on both Si- and C-terminated SiC surfaces (SiC(0001) and SiC(000$\bar{1}$), respectively). However, the graphene-substrate interface, growth kinetics and properties of epitaxial graphene layers are very different for the two SiC faces.

The growth of FLG on Si-terminated SiC surface occurs through the formation of the $(6\sqrt{3} \times 6\sqrt{3})R30^{\circ}$ ($6R3$) surface reconstruction. Experimental and theoretical studies have shown that the $6R3$ reconstruction corresponds to a single layer of carbon atoms with a graphene like atomic arrangement with a fraction of the C atoms covalently bound

to the substrate Si atoms [39,40,114,115]. No linear dispersion of π-bands typical for free standing graphene is observed for this interfacial layer, which is often called a buffer layer (BL). However, the next graphene layer above the buffer layer behaves electronically as a graphene monolayer, which is electron doped with a carrier density of $n \approx 10^{13}$ cm^{-2} due to charge transfer from the substrate. [39, 115–117]. In addition to electron doping, there is a considerable reduction in carrier mobility in the layer, which was found to be lower than 2000 cm^2/Vs [113]. Epitaxial graphene layers grown on SiC(0001) maintain the 30° orientation of the buffer layer relative to the SiC surface and are arranged in the graphitic AB stacking sequence.

For the C face of SiC, it was shown that the typical graphene electronic band structure appears already in the first epitaxial carbon layer and covalent bonds between this layer and the substrate do not occur [39]. Furthermore, it was shown that, in contrast to the SiC(0001) surface, where graphene layers grow in AB stacking on the Si face, on the SiC(000$\bar{1}$) C face graphene layers consist of domains oriented at angles around 0° and 30° relative to the SiC surface [118, 119]. During growth the majority of domains do not exhibit AB stacking. As a result, each carbon layer behaves electronically as an isolated graphene sheet and has a high carrier mobility close to the value of 250,000 cm^2/Vs [38].

Although graphene layers on SiC(000$\bar{1}$) show a much higher carrier mobility compared with those on SiC(0001), the growth on the Si faced SiC has some advantages. The lower growth rate for graphene layers on the Si face of SiC compared to the C face allows for better control of the growth process, so a defined number of graphene layers can be grown. This gives a possibility of creating n-layer (n=1,2,3...) graphene systems with AB stacking, which have different properties. The growth on SiC(0001) also leads to epitaxial graphene layers with improved structural quality than those grown on the C face, particularly, with better homogeneity, bigger grain sizes, and lower concentration of defects. Moreover, it was shown that graphene-SiC interface can be significantly modified by intercalation of several chemical species.

For the Si face, Riedl *et al.* have observed a transformation of the buffer layer to monolayer graphene following annealing of their graphitized SiC samples at temperatures higher than 600 °C in molecular hydrogen at atmospheric pressure [41]. Similar results were obtained by Virojanadara *et al.* who exposed graphene-SiC samples to atomic hydrogen fluxes at temperatures higher than 450 °C [120]. It was suggested that hydrogen atoms penetrated between the BL and the SiC substrate, broke the interface C-Si bonds and saturated any Si dangling bonds. This resulted in decoupling of the BL from the substrate and the formation of a band structure typical for monolayer graphene lying within the band gap of passivated SiC. This process was found to be reversible with the inverse transformation starting at about 700 °C associated with hydrogen desorption from the SiC surface [41, 120]. Other experimental groups have reported on the intercalation of fluorine [42], oxygen [121], gold [122, 123], lithium [124, 125], and sodium [126] into graphene-SiC interface. While in general, intercalation results in the decoupling of the buffer layer from the substrate, it can also lead to a doping of the decoupled graphene layers. For example, the intercalation of fluorine results in the strong p-type doping, while intercalation of Li or Na results in n-type doping. The intercalation of Au may lead to either n- or p-type doping depending on the Au coverage.

Theoretical investigations, based on *ab-initio* modelling, have shown that intercalation of hydrogen [127] and sodium [128] is energetically favorable and the type and level of doping, obtained from the band structure calculations, are in a good agreement with experimental results [128, 129]. However, mechanisms of intercalation of different atomic species into graphene-SiC interface have not been investigated sufficiently and are not understood. Furthermore, there are some experimental and theoretical results which are seemingly contradictory. For example, in an experimental investigation of atomic hydrogen adsorption on epitaxial graphene on SiC(0001), no evidence of hydrogen penetration below a graphene layer was observed even at 800 °C [130]. Based on the first principles modelling the energy barrier for H_2 diffusion through the BL was reported to be

6.5 eV [127], that is higher than the experimental value of 4.52 eV for the dissociation energy of the H_2 molecule [131]. The energy barrier for atomic hydrogen diffusion through graphene was reported to be about 4 eV from *ab-initio* calculations [132]. Thus, direct hydrogen diffusion through the BL on SiC(0001) seems to be unrealistic in the temperature range 450–600 °C, in spite of experimental evidences that it occurs.

Excluding a model where that the intercalating species cannot pass through pristine graphene, the most plausible route for the various species to the graphene-SiC interface is through openings in the layers afforded by the presence of various defects or grain boundaries. In practice these may be screw dislocations with an open core, grain boundaries and sample edges. It was reported from the *ab-initio* modelling that an open core screw dislocation with Burgers vector $2c$ has a core energy only about 10% higher than that of a full core [133]. Such a difference could easily be eliminated if the walls of the open core were passivated by hydrogen. However, the perfect screw dislocation with Burgers vector $2c$ appropriate for AB stacking might dissociate into partials lowering its energy. It is then unclear whether the H decorated open core screw dislocation is more stable than the dissociated closed core screw dislocation. In this chapter the results of *ab-initio* simulations of the diffusion of intercalating species through hollow sites in graphene are presented.

3.2 Details of calculations

All calculations presented in this chapter were performed within the local density approximation for the exchange-correlation potential. Core levels were treated within the Hartwigsen-Goedecker-Hutter pseudopotentials scheme [105]. Kohn-Sham valence orbitals were represented by a set of atom-centered s-, p- and d-like Gaussian functions [134]. Spin-polarization of the valence states was taken into account. Matrix elements of the Hamiltonian are determined using a plane wave expansion of the density and Kohn-Sham potential [107] with a cutoff of 200 Ha. All structures were modelled with periodic boundary conditions.

For modelling hexagonal SiC the 4*H*-SiC polytype structure was used. The calculated lattice parameters, a=3.05 Å and c=10.01 Å, are in a good agreement with experimental values, a=3.07 Å and c=10.05 Å [135]. The substrate was represented with four bilayers of SiC. A vacuum layer of 25 Å was included above the SiC surface to separate slabs in the [0001] direction.

A flat graphene layer was placed on top of the SiC(0001) surface. The dangling bonds on the $(000\bar{1})$ surface were passivated with hydrogen atoms. An optimization of atomic positions resulted in a graphene layer covalently bound to the substrate, thus representing the buffer layer (BL). It was shown that this approach correctly reproduced the structure and electronic properties of the BL on SiC(0001) when a real $6R3$ surface reconstruction is modelled [40, 114]. However, a unit cell for the $6R3$ surface geometry consists of 1310 atoms and is too big for realistic modelling of diffusion mechanisms, when a large number of structural optimizations are required. As an approximation to the real structure we used two different surface reconstructions: namely the $(\sqrt{3} \times \sqrt{3})R30^{\circ}$ ($R3$) and 4×4 SiC surface reconstructions. The *R*3 model was adopted in other theoretical investigations of graphene-SiC interfaces [116, 117]. In order to distinguish between the modelled structures and the real $6R3$ reconstruction the term interfacial carbon layer (ICL) will be used hereafter instead of the buffer layer (BL) within $R3$ and 4×4 models.

Integration over the Brillouin zone (BZ) was carried out within the Monkhorst-Pack sampling scheme [110] using 12×12×1 and 6×6×1 grids for the $R3$ and 4×4 models, respectively. Optimization of the atomic positions were performed using a conjugate-gradient algorithm until the change in total energy between two subsequent iterations was less than 1×10^{-5} Ha. For modelling diffusion processes and obtaining corresponding energy barriers, the climbing image Nudged Elastic Band (cNEB) method was used [136,137]. At least seven system images were used for discrete representation of diffusion paths. Structural optimizations along a diffusion path were carried out until the highest force acting on any atom in all system images were less than 0.001 atomic units.

3.3 Electronic and structural properties of the interfacial carbon layer on SiC(0001) according to the *R*3 and 4×4 models

Since simplified models for epitaxial graphene on SiC(0001) are used it is necessary to study the suitability of these models to describe the properties of the real system and to invesigate hydrogen diffusion through the interfacial carbon layer (ICL). Figure 3.1 shows schematic representations of the $R3$ and 4×4 SiC surface reconstructions for the ICL on SiC(0001). The $R3$ reconstruction has been used previously in theoretical investigations of the graphene/SiC(0001) interface [116, 117]. The band structure calculations show the absence of Dirac cones for the ICL and predict correctly the n-type doping of the next graphene layer above the ICL with the Fermi level at 0.4 eV above the Dirac point. It should be noted, however, that *ab-initio* calculations for the $R3$ reconstruction predict the metallic behavior of the ICL on SiC(0001), while it has been argued on the basis of Angle-Resolved Photoemission Spectroscopy (ARPES) measurements that the interface is semiconducting [39]. The metallic band in the ICL/SiC(0001) band structure arises from the Si dangling bonds of the substrate. Because of the lattice mismatch between SiC and graphene, an 8.2% extension of the graphene lattice constant is required to accommodate a 2×2 graphene cell on the $R3$ reconstructed SiC surface. Such a large extension of the graphene lattice will inevitably affect the barriers for diffusion of a hydrogen atom through the ICL. It has also been shown from *ab-initio* calculations that stretching of the C–C bond results in significant increase of the chemical reactivity of graphene [138]. Thus, it can be expected that the binding energy of the ICL to the SiC substrate and the binding energy of the H atom to the ICL will be overestimated in calculations using the $R3$ model.

The smallest structure in which graphene and SiC cells are almost commensurate corresponds to the 4×4 SiC surface reconstruction which accommodates the 5×5 graphene

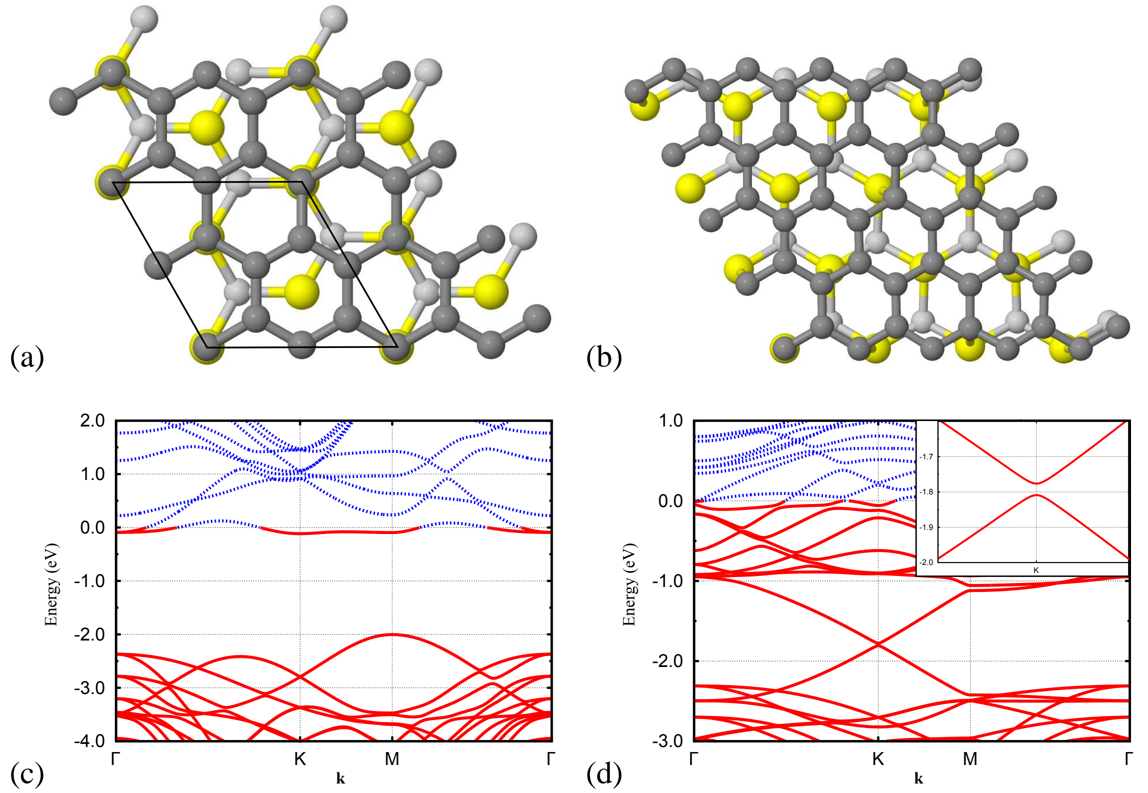

Figure 3.1: Schematic representations of atomic structures and calculated electronic band structures of the iterfacial carbon layer (ICL) on the $(\sqrt{3} \times \sqrt{3})R30^{\circ}$ (a) and (c), and the 4×4 (b) and (d) SiC(0001) surface reconstructions. The $(\sqrt{3} \times \sqrt{3})R30^{\circ}$ unit cell is indicated in (a). Silicon atoms are represented by large (yellow) circles. Smaller dark gray and light gray circles represent carbon atoms in the ICL and in the SiC substrate, respectively. Solid (red) lines represent occupied states, while (blue) dashed lines represent empty states. The position of the Fermi level is set to zero. The inset in (d) shows that graphene π and π^{*} bands are separated by the energy gap of 30 meV at the K-point in the Brillouin zone.

cell. This model requires only -0.02% change of graphene lattice constant to adjust the mismatch between the calculated lattice parameters of SiC and graphene. However, it should be emphasized that in this case the ICL orientation with respect to the substrate is 0° in contrast to the 30° orientation observed experimentally. Figure 3.1(d) shows the band structure for the 4×4 reconstruction. Remarkably, the graphene like π-bands are preserved for the ICL, despite a fraction of carbon atoms in the layer being covalently bound with the substrate. There is also an energy gap of about 30 meV separating the π and π^* bands at the K-point of the Brillouin zone (inset in Fig. 3.1(d)). The Fermi level is located well above the bottom of the π^* band indicating high n-type doping of the interfacial carbon layer and the metallic nature of the interface. Such a large difference between the band structures calculated with the use of the two models shows the importance of the orientation of the ICL relative to the SiC substrate.

Table 3.1 shows the structural parameters and the binding energy per C atom calculated for the ICL on SiC surfaces with the $R3$ and 4×4 reconstructions. The values for the $R3$ model are in a good agreement with those found in previous theoretical investigations [116, 117]. The average distance between the ICL and the SiC(0001) surface is nearly the same for both models. However, corrugations of the layer and the binding energy, calculated per C atom, differ significantly. For the 4×4 model, the binding energy per C atom is less than half that for the $R3$ model. This is due to several factors: i) stretching the graphene lattice in the $R3$ model increases the chemical reactivity of the layer; ii) in the $R3$ model the C atoms which form covalent bonds with the substrate are located directly above the surface Si atoms, which is not the case for the 4×4 model; iii) it is also very likely that the binding energy depends on the ICL/substrate orientation although it is difficult to estimate the contribution of this.

From the modelling of the actual reconstruction with $6R3$ periodicity the corrugation of the ICL was reported to be of the order of 1 Å [114]. This value is much bigger than those obtained from our calculations for both the $R3$ and 4×4 models. It should

Table 3.1: Calculated values for the average distance between the ICL and the SiC surface, h, maximum difference in the height of C atoms in the ICL, Δh, and the binding energy per C atom, E_b, for the ICL on the SiC(0001) surface.

Model	h, Å	Δh, Å	E_b, eV
$R3$	2.26	0.28	0.41
4×4	2.22	0.52	0.18

be noted, however, that in small cells, atomic displacements induce high lattice strains which result in a significant increase in the total energy of the system. In bigger cells such lattice strains can be reduced because of the correlated motions of a large number of atoms. The particular distribution of graphene C atoms, some of which are tightly bound to the substrate Si atoms and some are not, are different for the $R3$, 4×4 and $6R3$ reconstructions, and this can also result in different magnitude of the corrugation of a graphene layer.

3.4 Effect of lattice strain on the binding energy and diffusion of hydrogen through a graphene layer

To investigate the effect of a graphene lattice extension on the diffusion of atomic hydrogen through the layer a set of calculations for single isolated graphene sheets with different lattice constants varying in the range of 0-10% was performed. For these calculations 6×6 graphene cells have been used. The 9×9×1 **k**-points grid has been used for the Brillouin zone integration.

The barrier for diffusion of a hydrogen atom through a graphene layer is defined as the energy difference between the initial stable configuration and the saddle point configuration.

The most stable position of a hydrogen atom on graphene is the H atom chemisorbed to a C atom. So, it is reasonable to take this configuration as the initial one for the diffusion process. Thus, the diffusion barrier can be calculated as

$$Q = E_{\mathrm{SP}} - E_{\mathrm{init}} = E_{\mathrm{SP}} - (E_{\mathrm{gr}} + E_{\mathrm{H}} - E_{\mathrm{bind}}), \tag{3.1}$$

where E_{SP} is the energy of the saddle point configuration, E_{gr} is the energy of a separate graphene layer, E_{H} is the energy of a distant hydrogen atom, and E_{bind} is the binding energy of an H atom on graphene.

The dependence of Q on E_{bind} should be pointed out. The binding energy of the chemisorbed H atom on graphene with equilibrium lattice constant was calculated to be 1.18 eV. This value is larger than those in the range of 0.2–0.9 eV found in the majority of previously published theoretical works. Such a large scattering in the data can be explained by the use of different exchange-correlation functionals. The calculations with hybrid functionals give the lowest values of the binding energy, while the values of 0.6–0.9 eV are typical for GGA [138,139]. Previous calculations with the use of LDA predict the binding energy in the range 1–1.4 eV, which is close to our result [138, 140].

The energy barrier for diffusion of an H atom through a graphene layer was calculated to be 3.73 eV. In agreement with the results of Ito *et al.* [141], it is found that in the saddle point configuration the hydrogen atom is not exactly in the center of graphene hexagon but slightly shifted towards one of the C atoms. Figure 3.2 shows the dependence of the binding energy and diffusion barrier of an H atom on the extension of graphene lattice constant. In the vicinity of 10% isotropic expansion of graphene lattice, the change in the absolute value of the binding energy of H on graphene can be approximated by a linear dependence with a slope of 89 meV per 1% strain. This result is in a good agreement with the investigation of Andres *et al.* [138] and confirms the substantial increase of chemical reactivity of graphene upon the lattice stretching.

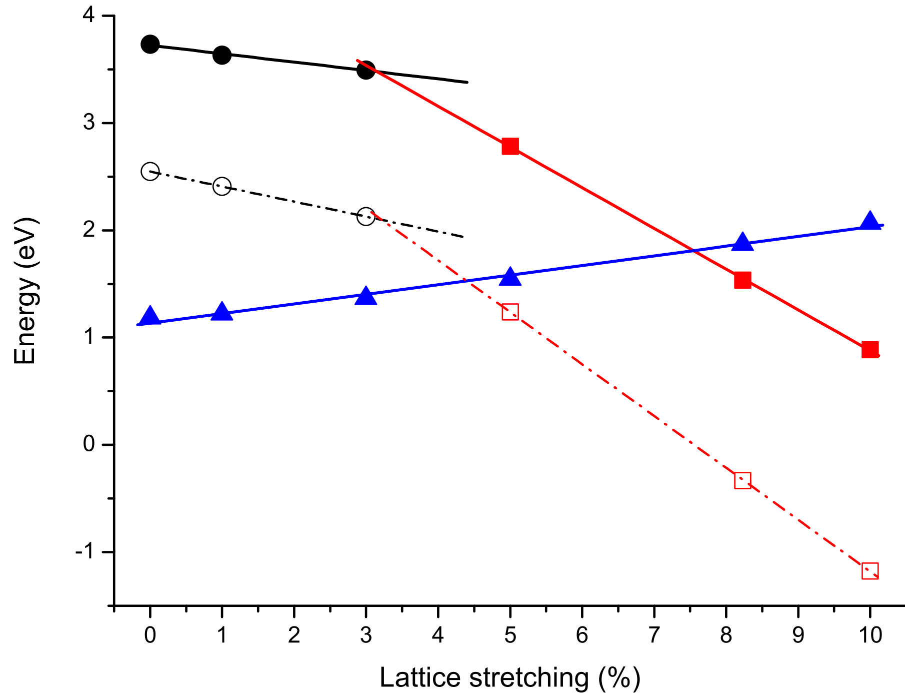

Figure 3.2: The calculated values of the binding energy of an H atom on graphene (blue triangles) and diffusion barrier of an H atom through a graphene sheet (red and black circles and squares) for different values of the graphene lattice constant stretching. Circles and squares distinguish two different dependencies of the diffusion barrier versus strain that correspond to the change of H diffusion path through the graphene layer. Open circles and squares shows the calculated diffusion barriers if the binding energy term is excluded from the Eq. 3.1. This corresponds to energy barriers for H diffusion through a graphene layer if the initial configuration is defined as an H atom remote from the layer. Lines represent linear fits to the data.

As can be seen from Fig. 3.2, there is a large decrease in the energy barrier for H diffusion through a strained graphene layer. The barrier for H penetration drops from 3.73 eV to 0.89 eV for 0% and 10% stretching, respectively. There are two clearly distinct regions in the plot of the diffusion barrier versus strain (shown with circles and squares in Fig. 3.2). An analysis shows that the data can be approximated by two linear dependencies with different slopes. In the range from 0% to about 3.2% expansion, the diffusion barrier changes with a rate of 78 meV per 1% dilation. Above 3.2%, the slope becomes much greater, corresponding to the change of the diffusion barrier with the rate of 380 meV per 1% dilation. The transition between two regions corresponds to the change of H diffusion path through the graphene layer. For a small strain, the H atom in the saddle point configuration is close to the center of the hexagon formed by C atoms. When the extension of graphene lattice is larger than 3.2% the saddle point configuration corresponds to the H atom in the middle of the C-C bond. Figure 3.2 also shows a plot of $Q - E_{\rm bind}$ versus graphene lattice constant expansion. This corresponds to energy barriers for H diffusion through a graphene layer if the initial configuration is defined as an H atom remote from the layer.

To summarize results of this section, we note that, 1) The permeability of graphene to H and the graphene chemical reactivity can be changed significantly by tensile strain; and 2) the use of the $R3$ model for the ICL on SiC(0001), which requires the extension of graphene lattice constant by 8.2%, will probably give incorrect values for the binding energy of H with the ICL and for the diffusion barrier of hydrogen through the layer. Thus we suggest that the 4×4 reconstruction, although it has not been observed experimentally, is a better approximation than the $R3$ model in the cases when the actual energies of atomic interactions are of more importance than the electronic properties.

3.5 Properties of a quasi-free-standing graphene layer on H- and F-passivated SiC(0001)

Figure 3.3(a) shows the band-structure of graphene on the H-passivated SiC(0001) surface calculated with the use of the 4×4 model. The band structure can be expressed as a sum of two components: the substrate component, consisting of the SiC slab and H-passivated SiC surface, and the graphene component. The graphene related bands are almost identical to those calculated for a separate graphene layer, indicating the small interaction of graphene with the substrate. The quasi-free-standing nature of graphene on the hydrogenated SiC(0001) has been also supported by experimental investigations [41, 142].

The Fermi level crosses the Dirac point indicating that there is no doping of the graphene layer. However, a slight p-type doping of the decoupled graphene layer has been observed experimentally [41, 142]. This effect has vanished after heating samples above 700 °C. Thus, the p-type doping has been proposed to arise from some surface adsorbates on the layer [41]. It should be noted that the key features of the band structure, namely appearence of graphene Dirac cones in the SiC energy gap and the absence of doping, are identical for the 4×4 and $R3$ reconstructions. This fact also supports the above mentioned results on the independence of the substrate and graphene components, since the band structures for the ICL strongly interacting with the substrate are very different for the 4×4 and $R3$ model.

Recently, it was shown that the buffer layer can also be decoupled from SiC(0001) by the intercalation of fluorine atoms [42]. However, in this case the strong p-type doping of the quasi-free-standing graphene layer was observed with the Fermi level at about 0.79 eV below the Dirac point. Figure 3.3(b) shows the calculated band structure of the graphene layer on F-passivated SiC(0001) surface. The position of the Fermi level is 0.38 eV below the graphene Dirac-point, indicating p-type doping of the layer in agreement with the

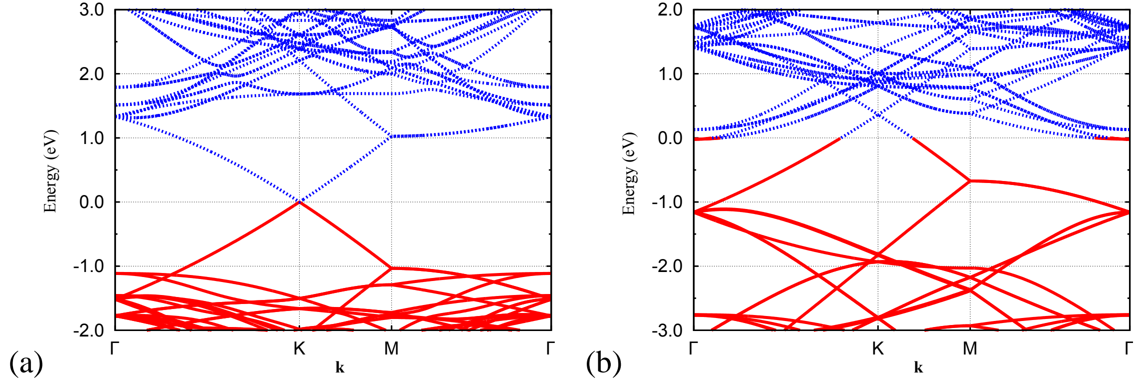

Figure 3.3: The calculated band structures for a graphene layer on top of the (a) hydrogenated and (b) fluorinated SiC(0001) surface calculated with the use of the 4×4 model. Solid (red) lines represent occupied states, while (blue) dashed lines represent empty states. The position of the Fermi level is set to zero.

experimental results. However, the magnitude of the doping obtained from the calculations is less than half that observed experimentally. Some extra doping of the layer in the experimental conditions might arise from surface contaminants. It should be noted that the discrepancy between the calculated and experimentally observed level of doping occurs for graphene layers on both H- and F-passivated SiC(0001) surface. In the band structure shown in Fig. 3.3(b), an electron pocket can also be seen around the Γ point in the Brillouin zone. An analysis of the wave function distribution shows that the electron pocket is localised at the SiC substrate, while a hole pocket, around the K point, is entirely located on the graphene layer. This result indicates that the p-type doping of graphene on the F-passivated SiC(0001) is due to a transfer of electrons from the graphene layer to the SiC substrate.

Table 3.2 shows the calculated values of the formation energy, the binding energy per C atom and the average distance from the substrate, for the quasi-free-standing graphene layer obtained by intercalation of fluorine and hydrogen atoms. The formation energy is calculated as $E_{\mathrm{f}} = E_{\mathrm{ICL}} - (E_{\mathrm{qfg}} + N/2 \times E_{\mathrm{H_2(F_2)}})$, where E_{ICL} is the energy of the SiC

Table 3.2: Calculated values of the formation energy, E_f, the binding energy per C atom, E_b, and the distance from the substrate, h, for the quasi-free-standing graphene layer obtained by intercalation of hydrogen and fluorine atoms. The distance h is calculated with respect to H(F) atoms.

	E_f, eV	E_b, meV	h, Å
H	-2.9	29	2.59
F	-10.8	25	2.85

substrate with the ICL, E_qfg is the energy of the quasi-free-standing graphene layer on hydrogen (fluorine) passivated SiC, $E_{\mathrm{H_2(F_2)}}$ is the calculated energy of the separate H_2 (F_2) molecule, and N is the number of H(F) atoms required to passivate all Si dangling bonds on the SiC(0001) surface. For the 4×4 reconstruction N is equal 16.

The negative values of the formation energy indicate that the process of H(F) intercalation and the decoupling of the ICL is energetically favorable. The formation energy also gives the qualitative evaluation of the stability of the structure. The H-intercalated samples were shown to be stable up to 600°C [41]. The very high absolute value of the formation energy for the case of fluorine intercalation suggests the extremely high stability of this structure.

The binding energy per C atom of the quasi-free-standing graphene layer to the substrate was calculated to be of the order of 30 meV for both structures. This result confirms the small interaction between the graphene and SiC-substrate. It should be noted that in the case of graphene on F-passivated SiC surface the charge transfer should result in an increase in the binding energy. This, however, can be compensated by the repulsion due to anti-bonding character between the F atoms and the π-states on the graphene.

3.6 Mechanisms for hydrogen penetration through the interfacial carbon layer on SiC(0001)

It was shown in the previous section that the decoupling of the interfacial carbon layer from SiC(0001) by intercalation of hydrogen or fluorine atoms is energetically favorable. In this section we examine different ways for hydrogen penetration below the ICL. For this reason we have modelled diffusion of atomic and molecular hydrogen through the ICL and defective graphene layers using the NEB method. The actual diffusion barriers depend on the binding energy of hydrogen in the initial configuration, E_{bind}, according to Eq. 3.1. For a flat free standing graphene layer without defects the binding energy of an H atom to any C atom in the layer is identical. However, for the ICL and for defective graphene layers, the symmetry of graphene lattice is broken and adsorption sites with different binding energies exist. To facilitate the comparison of the energy barriers for hydrogen diffusion through a graphene layer, an ICL, and different defects in graphene lattice, we exclude the binding energy term in Eq. 3.1 in further calculations. This is also justified by the fact that during the exposure of the ICL on SiC to a hydrogen atmosphere, some of the hydrogen atoms or molecules are adsorbed onto the ICL, while some of them diffuse directly through defective sites in the layer to the SiC surface.

Figure 3.4(a,b) shows the path for a hydrogen atom diffusion through the ICL obtained with the NEB method and the corresponding changes in the system total energy. The energy barrier for diffusion was calculated to be 2.55 eV with respect to the totatl energy of the separate H atom and the ICL/SiC structure. This value is the same as that for H diffusion through the free standing graphene. This result suggests that there is no qualitative difference between hydrogen diffusion through the ICL and free standing graphene layer. However, binding energies for a hydrogen atom on a graphene layer and on the ICL were found to be quite different. We have tested five different adsorption sites for the H atom on the ICL (see Fig. 3.4). The binding energies were calculated to be 2.10,

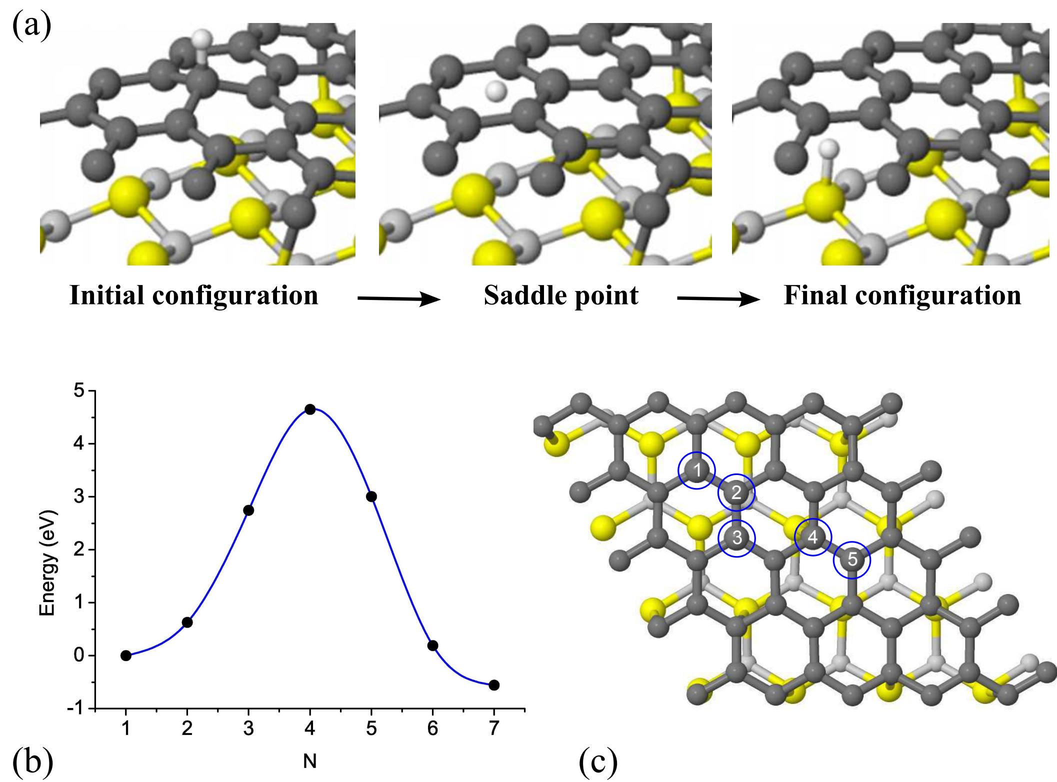

Figure 3.4: (a) Initial, saddle point and final configurations for H diffusion through the intefacial carbon layer (ICL) on the 4×4 SiC(0001) surface reconstruction. The total energy variation along the corresponding diffusion path is shown in (b). Black circles correspond to the calculated energies of atomic configurations along the diffusion path relative to the energy of the initial configuration. N is the number of an atomic configuration along the diffusion path. N equal 1, 4 and 7 corresponds to the initital, saddle point and final configurations, respectively. The blue solid curve is an interpolation shown as a guide for eyes. In (c) considered adsorption sites for an H atom on the ICL are marked out and numbered. The H atom adsorbed on the site 1 corresponds to the initital configuration for the modelled diffusion path.

2.90, 2.60, 2.35, and 3.56 eV for sites numbered 1, 2, . . . 5, respectively. All these values are much higher than the binding energy of H on the free standing graphene, which

was calculated to be 1.18 eV. The result for the ICL indicates that chemisorbed hydrogen is more stable in this environment than on a free-standing graphene. Adding a binding energy term to the calculated diffusion barrier of a hydrogen atom through the interfacial layer will give values in excess of 4.7 eV. Such barriers are too high to be overcome at 600°C, the temperature at which the hydrogen intercalation has been achieved experimentally. Modelling H_2 diffusion through the ICL and free standing graphene showed that a hydrogen molecule became unstable when passing through the defect-free layers, dissociating into atomic hydrogen. Thus, direct diffusion of hydrogen atoms and molecules through a defect-free ICL can be excluded from possible ways of H intercalation into the graphene-SiC interface.

Other possible mechanisms of hydrogen penetration through the ICL to the interface with SiC involve extended defects such as holes, threading edge and screw dislocations, discontinuities of the layer, grain boundaries, sample edges, etc. Of these, a threading open core dislocation is attractive as such a defect runs through the n-layer graphene, including the ICL as well as the SiC. However, modelling this defect requires supercells that are too large for realistic calculations, so instead we have calculated the barriers for hydrogen atoms and molecules migration through a heptagon ring in the Stone-Wales defect and open rings composed of a divacancy (V_2) and tetravacancy (V_4) (Fig. 3.5). The incorporation of these defects into a graphene layer is accompanied by long range relaxations of the surrounding lattice. The size of the ICL in the 4×4 model which corresponds to the 5×5 graphene cell, is not enough to account for these relaxations. Thus, the defects were modelled in the free standing graphene layers with 8×8 graphene unit cells.

The reasons for choosing the V_2 and V_4 defects are as follows. Removal of carbon atoms from the layer creates dangling bonds on the defect edges which are highly chemically reactive. For V_2 and V_4, the dangling bonds reconstruct in such ways that all atoms remain threefold coordinated (Fig. 3.5(d,e)). Thus, influence of the dangling bonds upon diffusion of hydrogen should be minimized for the case of these vacancy clusters. It has

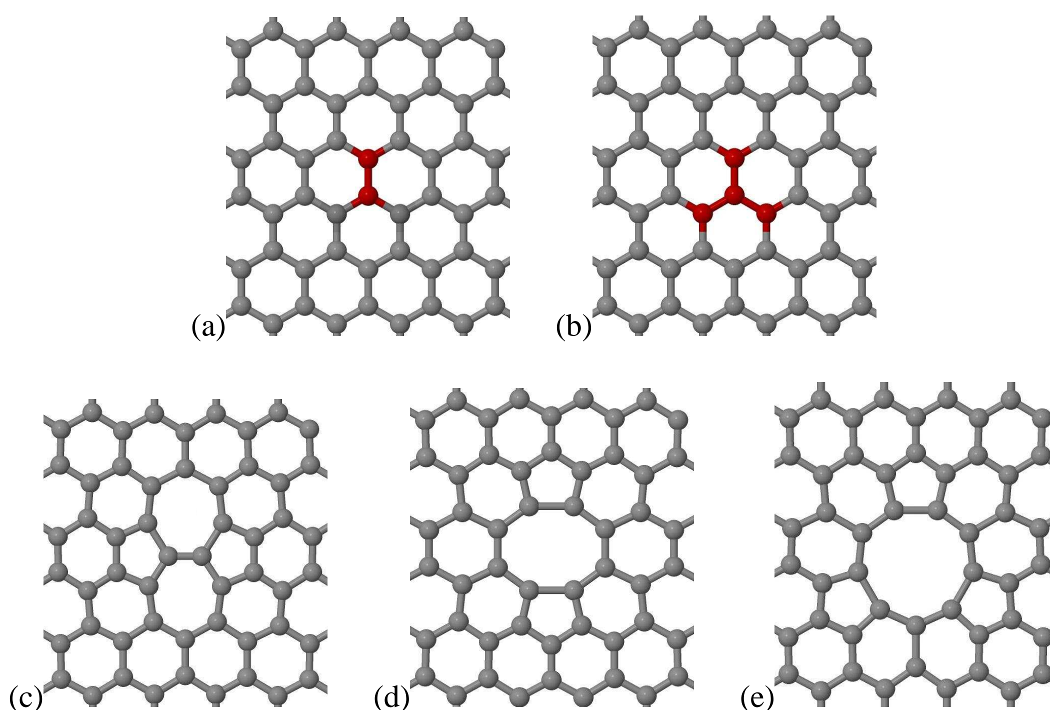

Figure 3.5: Atomic structures of Stone-Wales (SW), V_2 and V_4 defects in graphene. The SW defect (c) is formed by in-plane 90° rotation of the C–C dimer shown in red in (a). Removal of the C–C dimer results in the formation of the V_2 defect (d). The V_4 defect (e) is formed by the removal of four C atoms shown in (b) with red colour. The structures shown in (c)–(e) are the reconstructed defect structures.

been found, however, that interactions between hydrogen atoms and C atoms at the edges of the V_2 and V_4 defects are very strong. Optimization of structures with hydrogen atoms placed above V_2 or V_4 defects results in configurations with the H atoms being covalently bound to C atoms at the defect edges. Thus, an investigation of atomic hydrogen diffusion through these defects would require a thorough study of interactions between H atoms and defects edges. This study is beyond the aims of the present work and therefore diffusion of an H atom through the V_2 and V_4 defects has not been modelled.

Figure 3.6 shows the total energy variation along the paths for H diffusion through a hep-

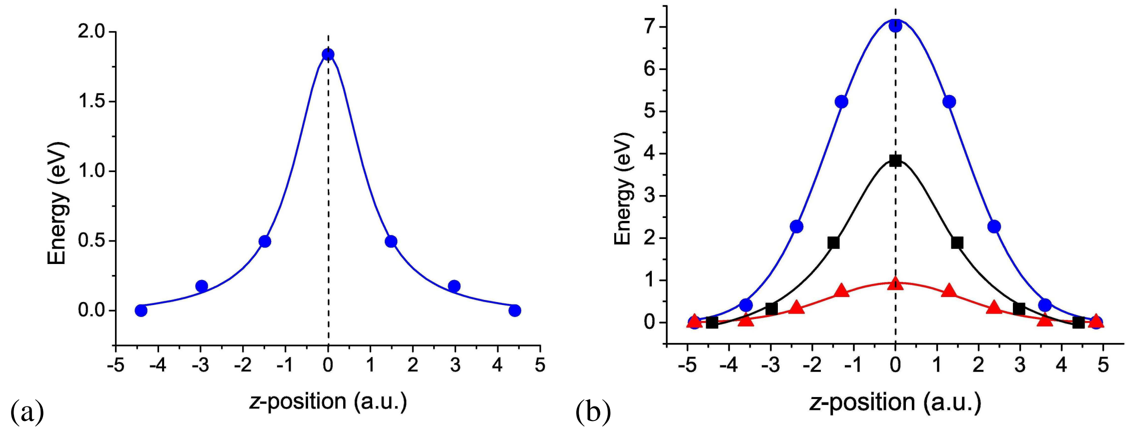

Figure 3.6: The total energy variation, $E_i - E_{\text{init}}$, along the paths for (a) H diffusion through a heptagon in a Stone-Wales defect and (b) for H_2 diffusion through the SW (blue circles), V_2 (black squares) and V_4 (red triangles) defects in the graphene layer. The symbols correspond to the calculated energies of atomic configurations along a diffusion path, E_i, relative to the energy of the corresponding initial configuration E_{init}. z-positions correspond to positions of a hydrogen atom or the center of a hydrogen molecule along the axis perpendicular to the graphene plane. The zero of this axis is the position of the graphene plane. The solid curves are the interpolations shown as guides for eyes.

tagon in a Stone-Wales defect and for H_2 diffusion through the SW, V_2 and V_4 defects in the graphene layer. Initial and final configurations for modelling the diffusion processes were chosen to be H or H_2 physisorbed above and below the defects in the layer. It was found that saddle point configurations for all diffusion paths correspond to a hydrogen atom or the center of a hydrogen molecule crossing the graphene plane approximately at the center of a defect. The path for H_2 diffusion through the V_4 defect obtained with the NEB method is shown in Fig. 3.7. Since diffusion calculations are very time consuming, the found saddle point configurations were then optimized separately to ensure the convergence of the calculations. The calculated energy barriers for atomic and molecular hydrogen diffusion through the defects considered are given in Table 3.3.

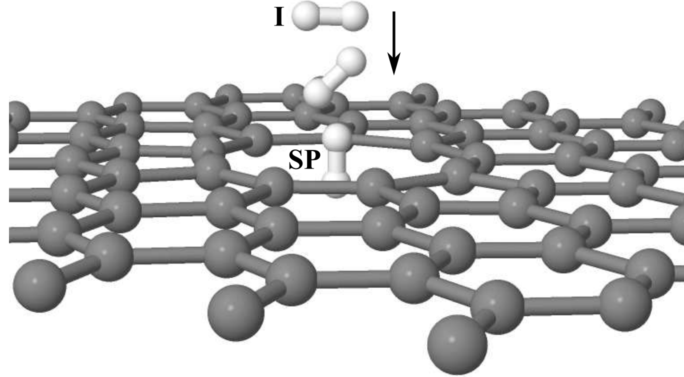

Figure 3.7: A path for H_2 diffusion through the V_4 defect. Positions of the H_2 molecule in the initial and saddle point configurations are denoted by I and SP respectively.

Table 3.3: Calculated values of energy barriers in eV for H diffusion through a perfect graphene layer and a heptagon in a Stone-Wales (SW) defect and for H_2 diffusion through the SW, V_2 and V_4 defects in the free standing graphene layer. The energy barriers were calculated with respect to H and H_2 remote from the graphene layers.

	Pristine	SW	V_2	V_4
H	2.55	1.52	-	-
H_2	-	6.89	3.64	0.69

The diffusion rate is proportional to $\nu\text{exp}(-W/kT)$, where W is energy barrier and ν is the attempt frequency, taken as Debye frequency or 10^{13} s^{-1}. This rate is about 1 s^{-1} at temperatures 500 °C and 890 °C for barriers 2 and 3 eV respectively. Thus, the energy barrier for H diffusion through the Stone-Wales defect is low enough to be overcome at about 600 °C. However, if the binding energy of H to the graphene layer is taken into account the hydrogen diffusion through the SW defect will be very slow at 600 °C and lower temperatures.

For H_2 diffusion the energy barrier can be overcome at 600 °C only in the case of the V_4 defect. The average distance between H_2 and the C atoms at the defect edges in the saddle point configuration is 2.27 Å. Thus, hollow defects with lateral dimensions of about 4.5 Å and larger can provide a path for hydrogen molecules to diffuse through the ICL. The low value of the diffusion barrier of 0.69 eV suggests that the interaction between the H_2 molecule in the saddle point configuration and the V_4 defect edges is rather small. It could be suggested that hydrogen atoms would easily migrate through hollow defects of the same dimensions, if they are not trapped at the defect edges. This could be the case when the defect edges are already passivated by hydrogen or other chemical species.

3.7 Hydrogen diffusion between the interfacial carbon layer and SiC substrate

It has been shown that hydrogen can reach the SiC surface by diffusing through the hollow defects in the ICL. It remains unclear, however, if hydrogen atoms (molecules) can migrate between the ICL and the substrate in order to reach and passivate all Si sites at the SiC-graphene interface. To find an answer to this question two mechanisms of hydrogen intra-surfacial migration were investigated. First the energy barriers for an H atom migration between four different chemisorption sites on the Si-terminated SiC surface below the ICL were calculated (Fig. 3.8(a)). These barriers are all low and are 0.56, 0.59 and 0.67 eV. Then migration of a hydrogen molecule between the H-saturated SiC surface and the decoupled graphene layer (Fig. 3.8(b)) was considered. The total energy of the most favorable configuration was calculated to be only 0.34 eV higher than that for the configuration with the H_2 molecule remote from the slab, and the energy variation along the migration path was found to be within 0.3 eV. Thus, hydrogen molecules can easily intercalate between H-passivated SiC surface and a partially decoupled graphene layer, and migrate to the regions where the ICL is still covalently bound to the substrate. The

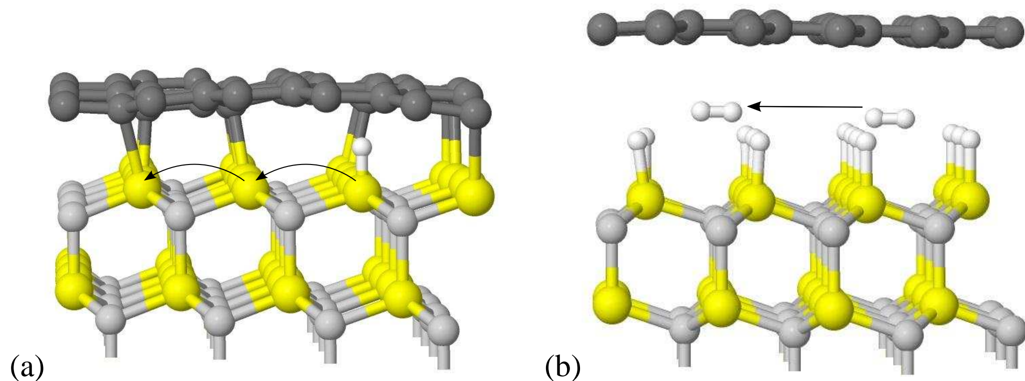

Figure 3.8: Schematic representation (a) H and (b) H_2 diffusion along the SiC surface below the interface graphene layer. Silicon atoms are represented by large yellow circles. Smaller dark gray and light gray circles represent carbon atoms in the graphene layer and in the SiC substrate, respectively. The arrows show the direction of hydrogen diffusion.

energy barriers for both considered mechanisms of hydrogen intra-surfacial diffusion are low enough to be overcome at 600 °C.

3.8 A model of hydrogen intercalation into graphene/SiC interface

Now a model for the processes that occur when the buffer layer on SiC(0001) is exposed to molecular hydrogen gas can be proposed. If there are no hollow defects in the BL, hydrogen molecules will be physisorbed on the BL. If hollow defects are present, some H_2 moleculed will be dissociated at the defect edges, and hydrogen atoms will chemically passivate them. Other molecules will diffuse through the defects and reach the SiC surface. On the SiC surface, H_2 molecules will dissociate into hydrogen atoms, which will then migrate along the surface, break covalent bonds between the substrate and the BL and passivate the surface Si atoms. Finally, when all SiC surface dangling bonds are pas-

sivated with hydrogen atoms the BL is transformed to a graphene layer that only weakly interacts with the substrate. In the case of the BL exposure to the atomic hydrogen gas the picture is qualitatively the same, excluding steps involving H_2 dissociation. It should be noted that experimentally decoupling of several graphene layers has also been observed. We suggest that in this case the diffusion of hydrogen towards the SiC surface occurs through the hollow defects penetrating several carbon layers. In practice, these can be open core screw dislocations, grain boundaries or sample edges.

3.9 Conclusions

Density functional theory has been used to investigate mechanisms of hydrogen intercalation into graphene-SiC(0001) interfaces, as well as the properties of graphene on H- and F-passivated SiC(0001) surfaces. It is shown that provided the passivating species can access the interfacial region, intercalation of hydrogen and fluorine atoms which results in decoupling of the buffer layer from the SiC substrate is energetically favorable. The decoupled graphene layer only weakly interacts with the substrate. The band structure calculations suggest that a graphene layer on H-passivated SiC(0001) is undoped, while in the case of F-passivated SiC(0001) the charge transfer results in p-type doping of graphene.

The present calculations also show that hydrogen atoms and molecules cannot diffuse through pristine graphene layers at 600 °C, the temperature around which hydrogen intercalation has been achieved experimentally. Considering vacancy clusters as prototypes of open regions in graphene, it is shown that the hydrogen diffusion readily occurs through hollow defects in graphene layers. We suggest that in practice the defects, through which hydrogen diffusion occurs, may be open core screw dislocations, grain boundaries and sample edges, which can penetrate several carbon layers. It is further shown that hydrogen can easily migrate along the graphene-SiC interface, break covalent bonds between

the buffer layer and the substrate, and thereby passivate the SiC surface.

Effects of the lattice strain on the permeability and chemical reactivity of graphene have been also studied. According to the calculations dilation of the graphene lattice by 10% results in an increased binding energy of a hydrogen atom, and a decrease in the energy barrier for a hydrogen atom to diffuse through the layer by as much as 75%.

Chapter 4

Graphene on diamond substrates

4.1 Introduction

Graphene and diamond are two carbon allotropes that have attracted a lot of interest for their singular electronic and optical properties. The very high mobility of charge carriers in graphene makes it a promising material for ultrafast electronics. Mobility values of several 10^6 cm^2/Vs were reported for suspended graphene layers [9, 35]. However, for many practical applications graphene has to be deposited on a substrate. In graphene on substrates additional scattering mechanisms due to the presence of surface defects, impurities, and substrate related phonons occur resulting in a lowering of the mobility of charge carriers by several orders of magnitude compared to the value for the free standing material. For graphene on SiO_2, the commonly used substrate, the typical value of mobility is around 20 000 cm^2/Vs [13]. In graphene deposited onto or encapsulated in hexagonal boron nitride, which contains a lower concentration of defects than SiO_2, mobility values higher than 100 000 cm^2/Vs can be achieved [36, 37]. Thus, substrates with high quality surfaces are required for high performance graphene-based electronic devices. Such substrates, with low densities of defects and surface roughness below 1 nm, can be made from

diamond [143]. Beside the high surface quality there are other advantages of diamond substrates. The higher energy of optical phonons in diamond compared with that in SiO_2 lowers the scattering of charge carriers in graphene by remote interfacial phonons and results in improved mobility and saturation velocity of the carriers [143, 144]. Recently an advantage of diamond-like carbon over SiO_2 substrates for high performance RF transistors has been demonstrated [145]. It has also been shown that due to the high thermal conductivity the use of diamond substrates allows better heat dissipation for graphene-based devices and improves the current-carrying capacity of graphene by one order of magnitude compared to that for graphene on SiO_2 [143].

For CVD (chemical vapor deposition) grown diamond the most technologically important surfaces are those with (001) and (111) orientation. Dangling bonds associated with surface atoms usually undergo reconstructions or are saturated with different atomic or molecular species, such as oxygen, hydrogen, hydroxyl groups, etc. The type of reconstruction/saturation of the surface has a significant effect on its electronic properties. For example, hydrogenated diamond surfaces are known to exhibit a rare property of negative electron affinity, while oxygen-terminated surfaces have a large positive electron affinity. Electronic properties of the graphene-substrate interfaces can also be significantly changed by a substrate surface termination. It was shown for epitaxial graphene grown on SiC(0001), that a strong graphene to substrate interaction eliminates the linear dispersion of graphene π-bands in the first grown graphene layer [39, 116]. However, this layer can be electronically decoupled from the substrate by intercalation of several chemical species into the graphene-SiC interface and passivation of the surface Si bonds [41, 42, 147]. The decoupled graphene only weakly interacts with the SiC substrate and can be considered as quasi-free-standing [142]. It has also been found that depending on the intercalated species the graphene layer can be undoped or doped either *n*- or *p*-type [42, 125, 147].

Naturally terminated surfaces may not be homogeneous and exhibit uncontrolled changes of properties across the surface or the interface. Thus, intentional passivation of a sub-

strate allows better control of the substrate quality and predictable modification of properties of the graphene-substrate interface. Hydrogenated diamond substrates have already been used for the production of graphene-based field-effect transistors [143, 148]. However, the properties of graphene-diamond interfaces have not been investigated thoroughly. In this chapter results of an *ab initio* study of the electronic properties of single and double layer graphene on H-, OH-, and F- terminated diamond (111) surfaces are reported.

4.2 Details of calculations

All results presented in this chapter were obtained from first-principles calculations within the local spin density approximation for the exchange-correlation potential. Core levels of atomic species were treated within the Hartwigsen-Goedecker-Hutter pseudopotential scheme [105]. Kohn-Sham valence orbitals were represented by a set of atom-centered *s*-, *p*- and *d*-like Gaussian functions [134]. Matrix elements of the Hamiltonian were determined using a plane wave expansion of the density and Kohn-Sham potential [107] with a cutoff of 200 Hartree (Ha). Periodic boundary conditions were applied to all modelled structures. Integration of the Brillouin zone was carried out within the nhorst-Pack sampling scheme [110]. A grid of $9 \times 18 \times 1$ **k** points was found to be enough to ensure the convergence of the total energy to within $1{\times}10^{-5}$ Ha for all structures and was used in all calculations. The **k**-point that corresponds to the graphene Dirac point was included in the sampling, this is necessary for an accurate determination of the Fermi energy in calculations involving graphene layers. Optimization of the atomic positions was performed using a conjugate-gradient algorithm until the change in total energy between two subsequent iterations was less than $1{\times}10^{-5}$ Ha. In all cases, this criterion corresponded to the maximum force acting on any atom in the final iteration being less than $1{\times}10^{-3}$ Ha/a.u. Within this approach the lattice constants of bulk diamond, a_D, and graphene, a_{GR}, were

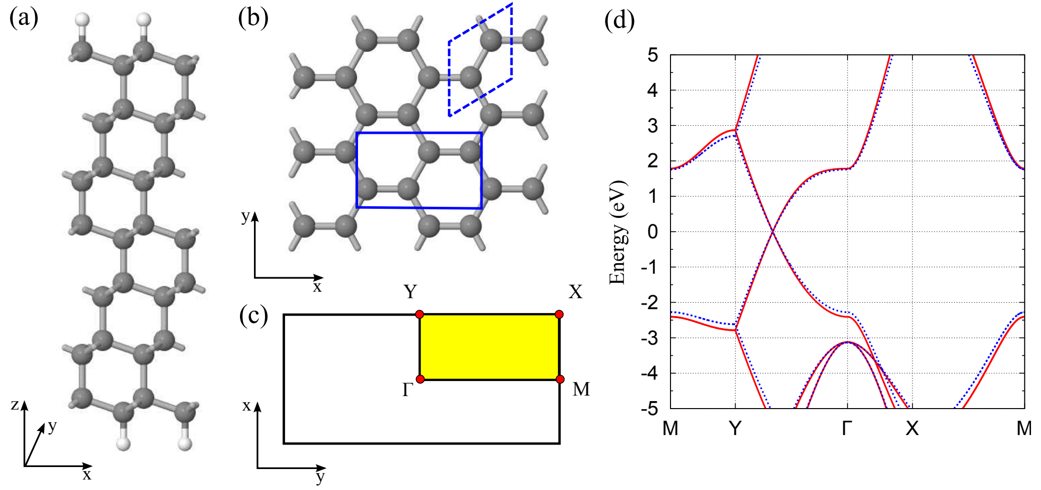

Figure 4.1: (a) The unit cell of the hydrogenated diamond substrate. (b) Atomic structure of graphene with the orthorhombic unit cell defined by the blue solid rectangle and the conventional unit cell defined by the blue dashed rhomb. (c) The Brillouin zone for the orthorhombic unit cell of graphene and diamond slab. Shaded region shows the irreducible part of the Brillouin zone with the **k**-points labelled. (d) The electronic structure of graphene with the equilibrium (red solid lines) and extended (blue dashed lines) lattice constants. The zero of the energy scale is set to the Fermi level.

calculated to be 3.53 and 2.45 Å respectively. These values are very close to the experimentally determined values of 3.57 Å for diamond [149] and 2.46 Å for graphene [150].

Modelling structures of diamond and graphene

For modelling diamond slabs and graphene layers orthorhombic unit cells were used (see Fig. 4.1(a,b)). An orthorhombic unit cell of graphene (see Fig. 4.1(b)) contains 4 C atoms and has lattice parameters a_1=$a_{GR} \times \sqrt{3}$=4.235 Å and a_2=a_{GR}=2.445 Å along x and y axis respectively. Among the different diamond surfaces the surface with (111) orientation has the lattice parameters which are the closest to those of graphene. For the or-

thorhombic unit cell of the (111) diamond surface the lattice parameters are a_1=4.328 Å and a_2=2.499 Å. Both values are 2.25% larger than those for graphene. For example, for the (001) diamond surface a_1=4.998 Å and a_2=2.499 Å. In this case the mismatch between graphene and diamond lattices in x direction is 18.10%. Thus, the (111) diamond surface has been used for modelling graphene on diamond. In order to adjust graphene and diamond unit cells the graphene lattice was strained by 2.25% in x and y directions. The band structure calculations have shown that such strain of the graphene lattice does not have significant effect on the shape of graphene electronic bands (see Fig. 4.1(d)). However, the calculated values of the work function are slightly different in these two cases. For graphene with the equilibrium lattice constant the work function was calculated to be 4.48 eV, while in the case of the stretched lattice constant the value of 4.69 eV was obtained. Both values are quite similar to the experimentally measured value of the work function of graphene, ~4.6 eV [151, 152].

Diamond substrates were represented with 14 atomic planes in z direction giving 28 C atoms per unit cell of diamond (see Fig. 4.1(a)). A vacuum layer of 25 Å was included above the diamond surface to separate adjacent slabs in z direction. The top and the bottom surfaces of the slab were identically terminated and covered with graphene in order to preserve the inversion symmetry of the system and avoid unwanted electric fields in the vacuum region of a supercell. The graphene layer was initially placed 2.5 Å above the diamond surface. For modelling bilayer graphene the second layer was placed in AB stacking at a distance of 3.28 Å from the first one. The equilibrium separation between the layers of 3.28 Å was calculated for AB graphite using the same method.

Electronic structure calculations

The electronic band structures were calculated along the MYΓX path of the Brillouin zone shown in Fig. 4.1(c). For each system the xy-plane-averaged electrostatic potential was also calculated as a function of the position along the z axis. This allows to determine

the value of the flat potential V_{vac} in the vacuum region. The electronic levels calculated for different systems can then be aligned to the same reference level by aligning their respective values of V_{vac}.

In order to distinguish the surface and the bulk related electronic states in the slab calculations, the band structures of the slab systems were compared with that calculated for the bulk diamond. The latter was modelled using the supercell of the same size as in the slab calculations but containing only diamond atoms. The bulk energy bands were then rigidly shifted such that the average electrostatic potential of the bulk system is aligned with the average electrostatic potential found in the middle of the slab.

Calculations of ionization potentials and electron affinities

The ionization potentials, I, and electron affinities, χ, for different systems were calculated as

$$I = V_{vac} - E_{\text{HO}} \quad (4.1)$$

$$\chi = V_{vac} - E_{\text{LU}}, \quad (4.2)$$

where E_{HO} and E_{LU} are the energies of the systems highest occupied state and the lowest unoccupied state, respectively. In the calculations of diamond substrates with different terminations, to distinguish the change of I and χ caused by the rigid shift of the bulk related states and that due to the appearance of the surface states, the values of the ionization potential and electron affinity for the bulk, I_{bulk} and χ_{bulk}, and that for the surface, I_{surf} and χ_{surf}, are given separately.

The use of the LDA-DFT for electronic structure calculations is known to result in underestimation of the energies of a system's excited states [153]. The energy gap of bulk diamond was calculated to be 4.22 eV, while experimentally this is measured to be 5.48 eV at low temperatures. It should be assumed therefore that the values of electron affinities

obtained in the calculations are underestimated by about 23%. It was shown that the calculated values can be corrected by multiplication with a scaling factor of 1.297 [154]. The electron affinity values given in this chapter are corrected according to this scaling procedure.

Calculation of graphene to substrate binding energy

The graphene to substrate binding energy per a C atom of graphene, E_{bind}, can be calculated as

$$E_{\mathrm{bind}} = \frac{1}{N}(E_{\mathrm{GR}} + E_{\mathrm{D}} - E_{\mathrm{GR/D}}), \tag{4.3}$$

where E_{GR}, E_{D} and $E_{\mathrm{GR/D}}$ are the total energies of the relaxed structures of isolated graphene, isolated diamond slab and the combined system, respectively, and N is the number of C atoms in a graphene layer.

4.3 Effect of the termination on the diamond (111) surface electronic properties

4.3.1 Clean surface

The clean (111) diamond surface is known to undergo a transformation into the Pandey reconstruction [155] with the uppermost C atoms arranged in zigzag chains extended over the surface (Fig. 4.2(a)). Each C atom within a chain is threefold coordinated and has an electron in $2p_z$ orbital, which does not participate in covalent bonding. The $2p_z$ orbitals form a network of π bonds along the chain which results in semimetallic behavior of the surface.

Figure. 4.2(b) shows the calculated electronic band structure of the Pandey-chain surface. Shaded regions represent conduction and valence bands of the bulk diamond. As can be seen from the plot the electronic structure of the bulk diamond is sufficiently well represented by the slab system. The surface π states are dispersed throughout the energy gap of the bulk diamond and cross the Fermi level. This indicates that the surface is semimetallic. In this case the surface ionization potential and electron affinity are equal and equivalent to the work function, which is the difference between the vacuum potential and the Fermi energy, thus, $I_{\text{surf}} = \chi_{\text{surf}} = 5.03$ eV. From the position of the bulk VBM and CBM, the ionization potential is $I_{\text{bulk}} = 5.85$ eV and the corrected electron affinity is $\chi_{\text{bulk}} = 0.37$ eV. The obtained values are in excellent agreement with previous theoretical investigations [154].

It is interesting to point out that the electronic configuration of the Pandey-chain (111) diamond surface and the formation of the extended π network resembles graphene. Furthermore, the value of the work function for the Pandey-chain surface, 5.01 eV, is quite similar to that of graphene, 4.6 eV.

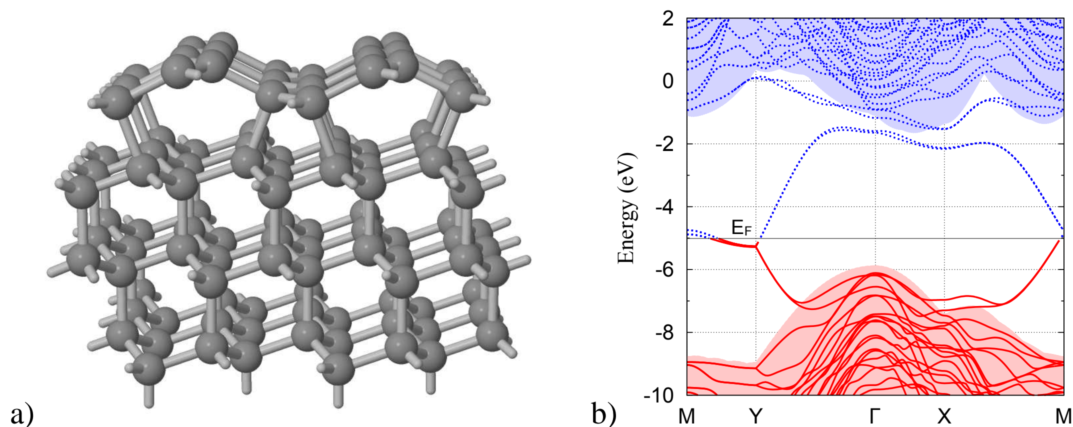

Figure 4.2: (a) Optimized atomic geometry and (b) calculated electronic band structure of the Pandey-chain reconstructed (111) diamond surface. Solid (red) lines represent occupied states, while (blue) dashed lines represent empty states. The zero of the energy scale is the vacuum level. Shaded regions represent the aligned band structure of the bulk diamond. The horizontal solid black line defines the Fermi energy.

4.3.2 Hydrogenated surface

It has been shown by theoretical [156] and experimental [157] investigations that hydrogen termination of the unreconstructed (111) surface is more energetically favourable than that of the Pandey-chain surface. Hydrogen termination is stable to about 900 °C, where H_2 desorbs. Figure 4.3 shows the atomic structure and the calculated electronic band structure of the unreconstructed (111) diamond surface terminated with H atoms. Hydrogen atoms saturate dangling bonds of the surface C atoms, removing the π states of the clean surface from the bandgap of the bulk diamond. The electronic structure of the hydrogenated diamond slab is very similar to that of the bulk diamond, except the unoccupied band has approximately parabolic shape below the bulk conduction band. This band, labeled as A in Fig. 4.3(b), was shown to originate mainly from the C-H σ bonds and is characteristic for hydrogenated diamond surfaces.

Comparing with the clean (111) surface the hydrogen termination results in the shift of the

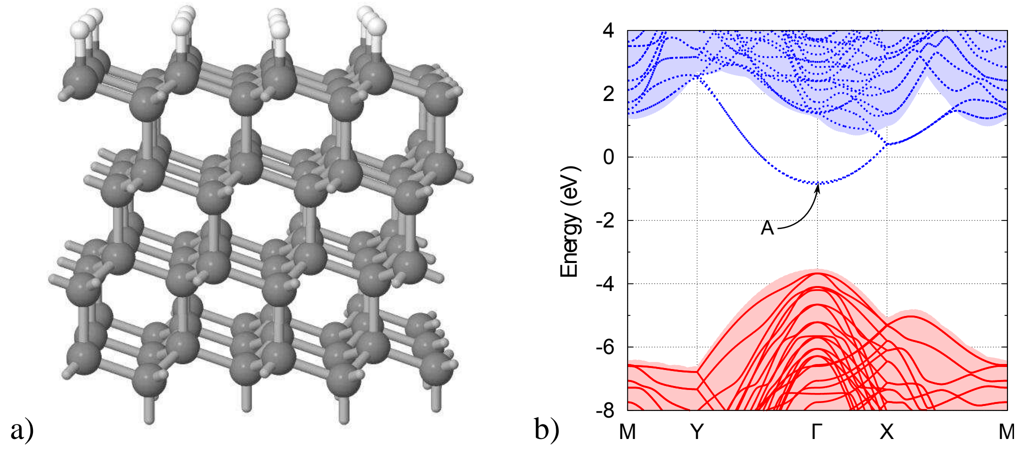

Figure 4.3: (a) Optimized atomic geometry and (b) calculated electronic band structure of the H-terminated (111) diamond surface. Carbon atoms are represented with large grey spheres, while H atoms are shown by small white spheres. The band labeled as A originates from the C-H σ bonds and is characteristic for hydrogenated diamond surfaces.

bulk related energy bands upward by about 2.28 eV. This shift is caused by the presence of the $C^{\delta-}$–$H^{\delta+}$ dipoles layer on the surface. Polarization of the surface C–H pairs occurs due to the higher electronegativity of C compared to H. The bulk ionization potential is $I_{\text{bulk}} = 3.57$ eV and the bulk electron affinity is $\chi_{\text{bulk}} = -1.91$ eV. The presence of the surface states below the bulk CBM results in $\chi_{\text{surf}} = 0.21$ eV. The obtained values are in a very good agreement with previous theoretical investigations [154]. However, experimental investigations have indicated the negative electron affinity of the hydrogenated diamond surfaces. For the (111) hydrogenated surface the value of -1.27 eV for χ has been obtained from ultraviolet photoelectron spectroscopy measurements. It should be noted, that experimental techniques usually probe the near surface region, which, strictly speaking, consists of a mixture of the surface and the bulk related states, while in theoretical studies these states can be clearly distinguished. Thus, measured values of the electron affinity should be between the χ_{bulk} and χ_{surf} calculated values.

4.3.3 Fluorinated surface

The atomic geometry of the fluorine terminated (111) surface and the corresponding electronic band structure are shown in Fig. 4.4. Fluorine atoms saturate the C dangling bonds of the unreconstructed (111) surface in a similar way as in the case of hydrogen passivation. However, in terms of the electronic properties the effect of the F and H termination is very different. Since F is more electronegative than C, the dipole moment of the surface $C^{\delta+}$–$F^{\delta-}$ pairs has opposite direction than that of $C^{\delta-}$–$H^{\delta+}$. Thus, in contrast to the H-terminated surface, fluorination causes the bulk related energy bands to move downwards by about 2.40 eV from their position with the clean surface (Fig. 4.4)(b). This results in $I_{\text{bulk}} = 8.25$ eV and $\chi_{\text{bulk}} = 2.77$ eV which are 4.63 eV larger than the same parameters for the hydrogenated (111) surface. Due to some mixing of the surface and bulk related states at the top of the bulk valence band (Fig. 4.4), the surface ionization potential is slightly lower than that of the bulk, $I_{\text{surf}} = 8.20$ eV.

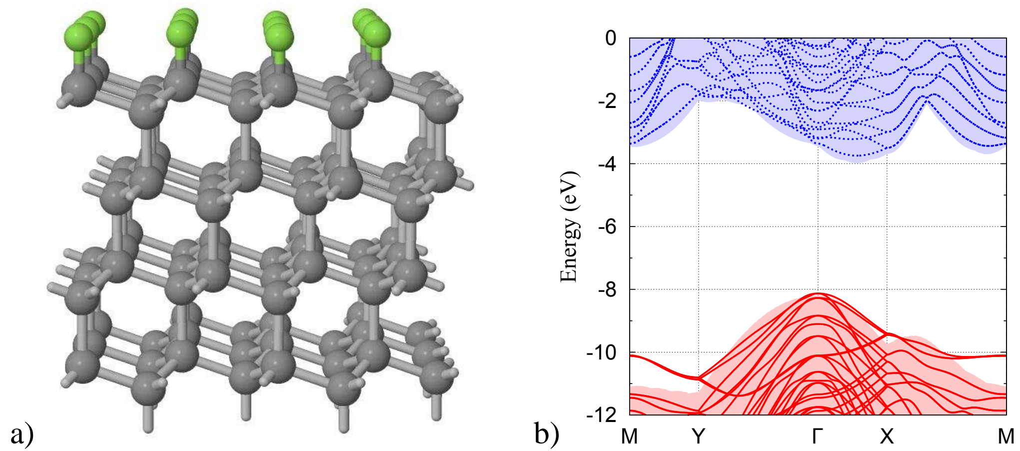

Figure 4.4: (a) Optimized atomic geometry and (b) calculated electronic band structure of the F-terminated (111) diamond surface. Carbon atoms are represented with large dark grey spheres, while F atoms are shown by smaller light grey spheres.

4.3.4 Hydroxylated surface

Hydroxylated and oxygenated diamond surfaces are of particular practical interest, since these types of termination often occur during CVD growth of diamond crystals and etching of their surfaces [158, 159]. It has been shown that diamond (111) surfaces etched in oxygen-water vapour under the high pressure are terminated by a full monolayer of OH groups [159]. The atomic geometry of the OH-terminated (111) surface is shown in Fig. 4.5. Orientation of the OH groups shown in Fig. 4.5(b) was found to be the most favourable in agreement with a previous theoretical study [160].

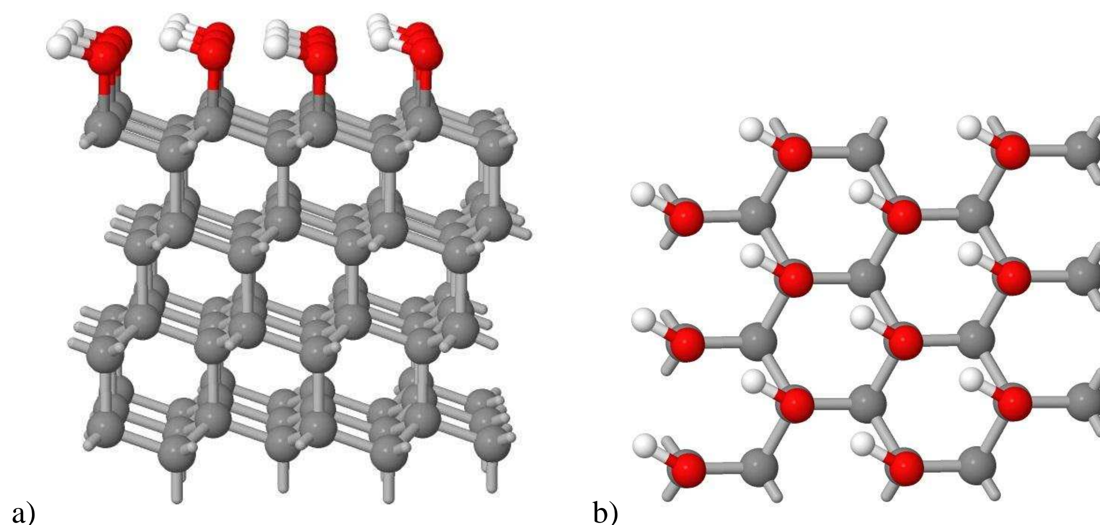

Figure 4.5: Optimized atomic geometry of the OH-terminated (111) diamond surface: (a) side view and (b) top view. Large grey spheres represent carbon atoms, red spheres show oxygen atoms, and small white spheres are hydrogen atoms.

Fig. 4.6 shows the calculated electronic band structure for the diamond slab with the OH-terminated (111) surface. The bulk VBM and CBM correspond to $I_{\text{bulk}} = 5.47$ eV and $\chi_{\text{bulk}} = 0.0$ eV, indicating the upward shift of the bulk related energy bands by about 0.38 eV relative to the clean surface. The direction of the shift is similar to that for the H-

terminated surface, however its magnitude is much smaller. This suggests that relatively weak polarization of the C–OH bonds occurs, which results in the formation of the $C^{\delta+}$–$(OH)^{\delta-}$ dipoles layer on the surface. Due to the presence of the occupied states above the bulk VBM the surface ionization potential, $I_{\text{surf}} = 4.78$ eV, is lower than the bulk value.

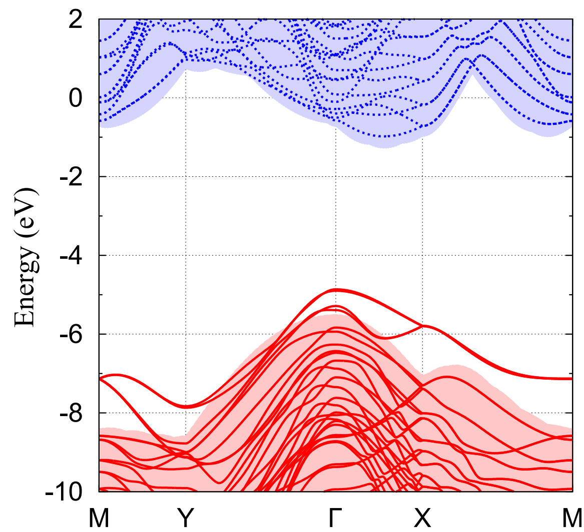

Figure 4.6: Calculated electronic band structure of the OH-terminated (111) diamond surface. Solid (red) lines represent occupied states, while (blue) dashed lines represent empty states. The zero of the energy scale is the vacuum level. Shaded regions represent the aligned band structure of the bulk diamond.

4.4 Graphene on passivated diamond substrates

4.4.1 Graphene on the H-passivated diamond (111) surface

The optimized atomic geometry of a graphene layer on the H-terminated diamond (111) surface is shown in Fig. 4.7. No significant changes in both graphene and H-passivated diamond atomic structures were caused by the relaxation. However, the graphene layer moved slightly away from the initial position of 2.5 Å above the surface. The final separation between the graphene layer and the surface hydrogen atoms was found to be 2.60 Å.

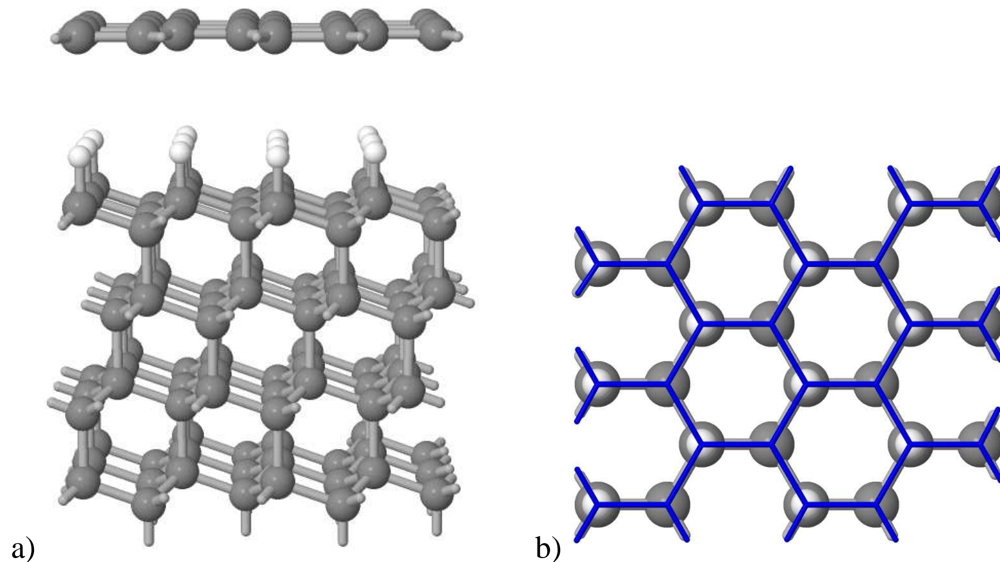

Figure 4.7: Optimized atomic geometry of a graphene layer on the H-terminated (111) diamond surface: (a) side view and (b) top view. Carbon atoms are represented with large grey spheres, while H atoms are shown by small white spheres. In (b) graphene lattice is shown by blue wireframe.

Figure 4.8(a) shows the calculated electronic band structure of graphene on the H-passivated (111) diamond surface. The graphene and diamond components of the band structure can be clearly distinguished. Moreover, the shape of both graphene and diamond related

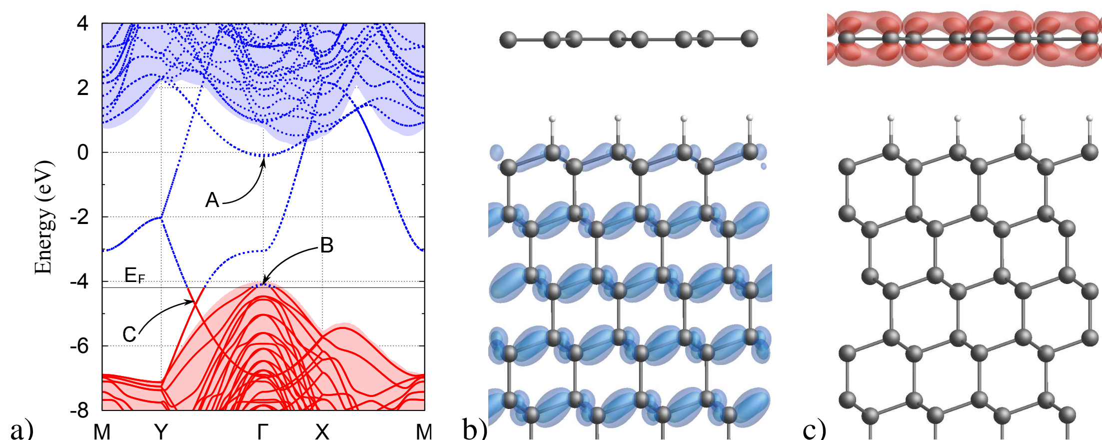

Figure 4.8: (a) Calculated electronic band structure for a single graphene layer on the hydrogenated diamond (111) surface. Solid (red) lines represent occupied states, while (blue) dashed lines represent empty states. The zero of the energy scale is the vacuum level. Shaded regions represent the aligned band structure of the bulk diamond. The horizontal solid black line defines the Fermi energy. (b) and (c) show the plot of the charge density with two isosurface values for the states defined as B and C in (a) respectively. Blue and red colors correspond to the charge density of unoccupied (b) and occupied (c) states respectively. The state defiend as A is referred to in the text.

bands is very similar to those calculated for isolated structures, indicating that graphene-substrate interaction is very weak. The unoccupied band labeled as A in Fig. 4.7(b) originates from the C-H bonds of the hydrogenated diamond surface. It should be noted that for the isolated diamond substrate the minimum of this band at Γ was found to be about 2.1 eV below the bulk CBM. The presence of graphene shifts the minimum of the band by about 1.7 eV upwards in energy, however, the form of the band remains parabolic.

The graphene Dirac point, which separates occupied and empty states in a free standing layer, lies below the valence band maximum of diamond. This results in electron transfer from the substrate to the graphene layer. The position of the Fermi level (see Fig. 4.8(a)) indicates that states at the top of the diamond valence band are empty while graphene re-

lated states are filled up to 0.52 eV above the Dirac-point. The plot of the charge density shows that the empty states in the diamond valence band, and hence the positive charge, are mainly delocalized over the bulk-like region of the diamond substrate (Fig. 4.8(b)). The negative charge, due to the graphene states occupied above the Dirac point, is delocalized over the graphene layer (Fig. 4.8(c)). No mixing of graphene and diamond states is observed.

The concentration of electrons in a graphene layer due to the doping can be found by integration of the graphene density of states. Since for graphene on H-terminated diamond the linear dispersion of graphene π bands is preserved, the standard equation for graphene density of states can be used [13]:

$$\rho(E) = \frac{2\,|E|}{\pi\hbar^2 v_F^2}, \tag{4.4}$$

where $\rho(E)$ is the density of states per unit area of graphene, $v_F \approx 10^6 ms^{-1}$ is the Fermi velocity and E corresponds to the energy difference between the Fermi level and the Dirac point. Integration of the density of states (Eq. 4.4) gives the concentration of charge carrier in graphene:

$$n = \frac{|E|^2}{\pi\hbar^2 v_F^2}. \tag{4.5}$$

Using Eq. 4.5 and the value of 0.52 eV for E the density of free electrons in the graphene layer on the H-terminated diamond (111) surface was calculated to be about 2×10^{13} cm^{-2}.

Although there may be some uncertainty as to the realization of charge transfer between the graphene and diamond, it should be noted that such an effect was predicted for C_{60} absorbed onto hydrogen terminated diamond [161], which was subsequently observed experimentally [162].

It should be noted that the bulk diamond VBM appears 4.12 eV below the vacuum level, so, there is a downward shift of the diamond energy bands by about 0.55 eV from their position in the calculations of the hydrogenated diamond substrate without graphene. This effect can be explained by the p-type doping of the substrate. The graphene Dirac-point is found at -4.72 eV with respect to the vacuum level, which is very similar to the value of -4.69 eV calculated for the isolated graphene layer.

Graphene to substrate binding energy, for the configuration shown in Fig. 4.7(b), where two of four C atoms in the graphene unit cell are positioned directly above surface hydrogen atoms, was calculated to be 36 meV per atom. Changing the position of the graphene layer in the horizontal plane results in slightly lower values of E_{bind}. However, for all the tested structures this deviation was smaller than 5 meV per atom and no changes in the band structure were observed. Such small values of the binding energy indicate very weak interaction between graphene and the H-terminated diamond surface.

4.4.2 Graphene on the F- and OH-passivated diamond (111) surfaces

Similar to the case of graphene on the hydrogenated diamond surface, relaxation of a graphene layer on the F- and OH-terminated surfaces does not result in significant changes of both graphene and the substrate atomic structures. The separation between the graphene layer and the surface in the optimized structures was found to be 2.86 Å and 2.77 Å for the fluorinated and hydroxylated surfaces respectively. The binding energy per C atom of graphene was calculated to be 27 meV for graphene on the F-terminated surface and 33 meV for graphene on the OH-terminated (111) diamond surface.

The calculated electronic band structures of graphene on the F- and OH- terminated diamond (111) surfaces are shown in Fig. 4.9. In both cases the electronic structure can be simply expressed as a superposition of graphene and diamond components. The graphene Dirac point lies in the energy gap of the F- and OH-terminated diamond surfaces. Thus,

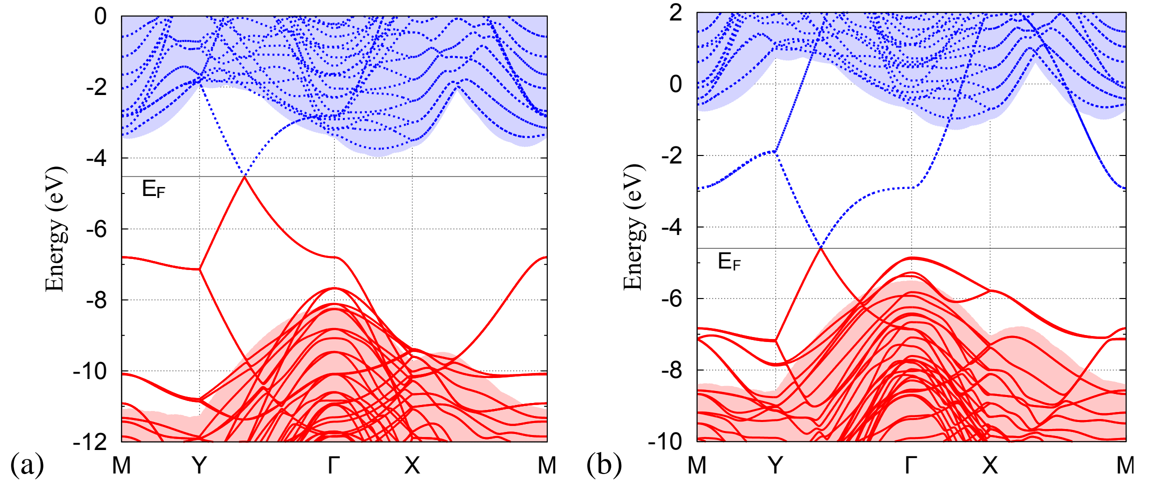

Figure 4.9: Calculated electronic band structure for a single graphene layer on the (a) F- and (b) OH-terminated diamond (111) surfaces. Solid (red) lines represent occupied states, while (blue) dashed lines represent empty states. The zero of the energy scale is the vacuum level. The horizontal solid black line defines the Fermi energy.

no charge transfer and no doping of graphene or substrate occur. The Fermi level crosses the Dirac point as in the case of a free standing graphene layer.

4.4.3 Bilayer graphene on the passivated diamond substrates

The calculated electronic band structures for bilayer graphene on the H-, OH- and F-passivated diamond (111) surfaces are shown in Fig. 4.10. For graphene on the hydrogenated diamond surface a gap of about 0.15 eV between graphene conduction and valence bands appears. The appearance of a band gap is a characteristic of a bilayer graphene in the presence of a difference between the electric potentials of the layers [163, 164]. In the case of the bilayer on the H-passivated diamond surface the charge transfer from the substrate results in a different amount of doping of the two layers, so the electric potentials of the layers are different. Similar splitting has been predicted from *ab-initio* calculations for bilayer graphene on the SiC(0001) surface, where the charge

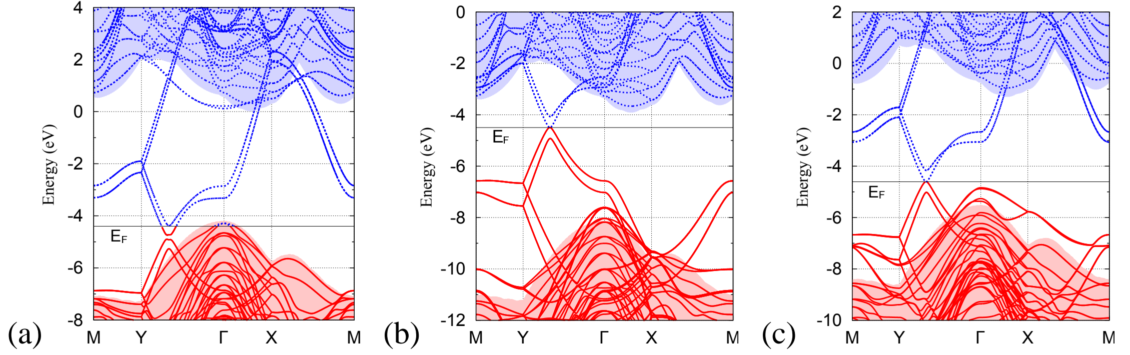

Figure 4.10: Calculated electronic band structure for a bilayer graphene on the (a) H-, (b) F-, and (c) OH-terminated diamond (111) surfaces. The zero of the energy scale is the vacuum level. The horizontal solid black line defines the Fermi energy.

transfer between the graphene and the substrate occurs [116].

In the case of bilayer graphene on the OH- and F-terminated diamond (111) surfaces, the work function of graphene lies in the energy gap of diamond. Thus, no charge transfer between the bilayer and the substrate occurs. The electronic band structure can be expressed as a sum of graphene and diamond components.

4.5 Discussion

Since the interaction between graphene and passivated diamond substrates is very weak and does not result in significant perturbation of both graphene and diamond energy bands, similar conclusions on the possibility of the charge transfer between graphene and diamond substrates can be obtained by considering their ionization potentials, I, and electron affinities, χ. For graphene $I_{\mathrm{GR}} = \chi_{\mathrm{GR}} = W_{\mathrm{GR}}$ is the graphene work function, which is the difference between the vacuum potential and the Fermi energy. In a free standing graphene layer the Fermi energy crosses the Dirac point. The charge transfer between the dielectric substrate and the graphene layer will occur if the work function of

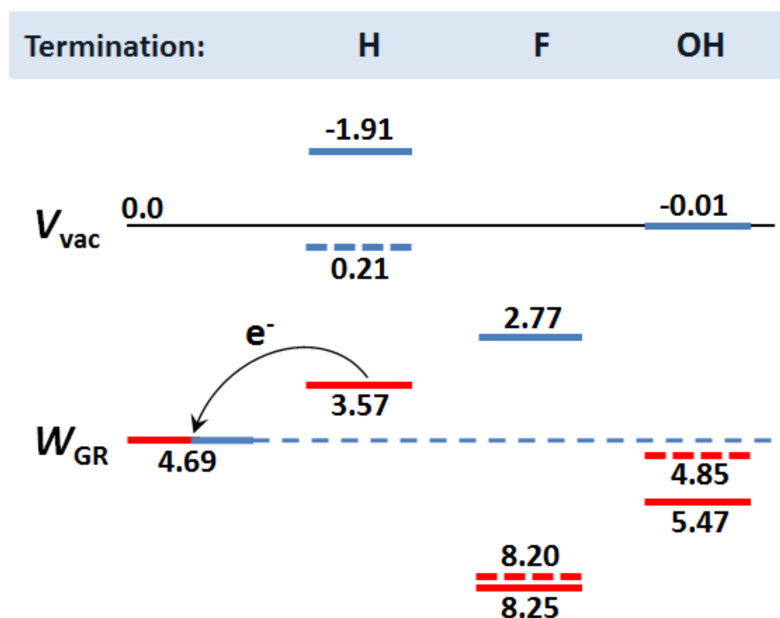

Figure 4.11: Calculated values of ionization potentials (red lines) end electron affinities (blue lines) for H-, F- and OH-terminated (111) diamond surfaces. The bulk related values are defined by short solid lines, while the surface related values are shown with short dashed lines. The zero of the energy scale is the vacuum level V_{vac}. Long dashed line defines the calculated work function of graphene, W_{GR}. All energy values are given in eV.

graphene crosses the conduction or valence bands of the substrate. Or in other words, the condition for the electron transfer from the substrate to the graphene layer is $W_{GR} \leq I_{sub}$ and for the electron transfer from graphene to the substrate is $W_{GR} \geq \chi_{sub}$. The I_{sub} and χ_{sub} are the ionization potential and the electron affinity of the substrate.

It has been shown in the Section 4.3 that the ionization potential and the electron affinity of the diamond substrate, I_D and χ_D, can be significantly changed by the different surface terminations. Figure 4.11 shows schematically the calculated values of I_D (red lines) and χ_D (blue lines) for H-, F- and OH-terminated (111) diamond surfaces together with the calculated work function of graphene. For the H-terminated surface the value of I_D is lower than W_{GR}, thus, the transfer of electrons from the substrate to the graphene layer

will occur. In the case of the F- and OH-terminated surfaces the value of W_{GR} is between I_{D} and χ_{D} and no charge transfer is expected. These conclusions agree with the results obtained in the previous section DFT calculations of the graphene layers on the passivated diamond substrates.

4.6 Conclusions

In this chapter the electronic properties of graphene/diamond interfaces have been studied with the use of density functional theory. The results obtained show that for a single graphene layer on the H-, F- and OH-terminated (111) diamond surfaces the linear dispersion of graphene π-bands is preserved and the shape of graphene electronic bands is very similar to that calculated for a free standing layer. Thus, graphene layers only weakly interact with the passivated diamond surfaces can be considered as quasi-free-standing. Similar cases have been found to occur for graphene on H- and F-passivated SiC(0001) surfaces [41, 142, 147].

For graphene on the hydrogenated diamond (111) surfaces the charge transfer results in n-type doping of graphene layers and p-type doping of the substrate. In the case of a single graphene layer the density of charge carriers is estimated to be about 3.7×10^{13} cm^{-2}. For the bilayer graphene on hydrogenated diamond substrates the doping results in the appearance of a 150 meV energy gap between graphene conduction and valence bands. For graphene on the OH- and F-terminated diamond surfaces no transfer doping occurs.

Chapter 5

Doping of fluorographene by surface adsorbates

5.1 Introduction

Graphene is considered a promising material for nanoelectronics due to its very high carrier mobility [165–167]. However, the absence of an electronic energy gap is a serious limitation for applications of graphene to conventional electronic devices. Indeed, the creation of an energy gap in the electronic spectrum of graphene is currently a subject of intense research. One way to open the band gap is to change the electronic configuration of carbon atoms from sp^2 to sp^3 by functionalization with other chemical species [46,47]. Following this route several graphene derivatives, which show insulating behavior, have been realized: namely, graphene oxide [48], graphane [46, 49, 50] and fluorographene (graphene monofluoride) [51–55]. In contrast to oxidized graphene layers, which are highly inhomogeneous, graphane and fluorographene (FG) are formed by ordered arrangement of hydrogen (in the case of graphane) and fluorine (in the case of FG) atoms on both sides of the graphene layer. Such ordered graphene derivatives can be considered as

new two-dimensional (2D) crystals. While graphane can be decomposed quite easily [50], FG shows high chemical and temperature stability (up to 400°C) [51]. The resistivity of fluorographene has been shown to be higher than 1 TΩ indicating that FG is an insulator with a wide energy gap [51]. The value of 3 eV was obtained for the energy gap of fluorographene from optical measurements [51]. However, for successful applications in electronics the graphene based dielectrics require doping with free charge carriers. It was shown that in pristine graphene, charge carriers can be introduced by deposition of several metals and molecules [168–172]. Ways for introduction of free charge carriers into fluorographene have not yet been studied and are considered in the present work.

In general, doping of a semiconductor (SC) by surface adsorbates occurs if there is a charge transfer between the semiconductor and the adsorbate. This requires a difference in electronic chemical potentials at the interface. For efficient n-type doping the ionization energy (IE) of the adsorbate should be lower than the electron affinity at the SC's surface. In terms of the electronic levels this means that the highest occupied level of the adsorbate should lie above or close to the conduction band minimum of the SC. Thus, to investigate the possibility of n-type doping of fluorographene two metal atoms with the low value of the IE, potassium and lithium, have been chosen. A gold atom has high IE and is considered for comparison. Potassium is known to act as a donor for pristine graphene, while little charge transfer has been predicted theoretically for the case of Au atoms [168, 169, 172]. For efficient electron transfer from the SC to the adsorbate, which results in p-type doping, the electron affinity of the adsorbate should be larger than the work function of the SC. This requires that the lowest unoccupied electronic level of the adsorbate lies below or close to the valence band maximum of the SC. Thus, as a potential p-type dopant for FG the F4-TCNQ molecule has been considered. This organic molecule has a high electron affinity of 5.2 eV, and it was shown to be an efficient acceptor for different carbon allotropes: graphene [173–175], nanotubes [176] and diamond [177].

5.2 Details of calculations

Spin-optimized DFT calculations were performed using the local density approximation (LDA) for the exchange-correlation potential. Hartwigsen-Goedecker-Hutter pseudopotentials were used to eliminate core levels [105]. Basis sets of independent atom-centred $s-, p-$ and d-like Gaussian functions were used to represent the Kohn-Sham orbitals. The charge-density is Fourier transformed and fitted using plane waves with a cutoff energy of 200 Ha. The FG structure is modelled from the flat graphene layer by adding a fluorine atom to each carbon atom and optimising both the atomic positions and the lattice constant. The chair configuration of fluorographene (Fig. 5.1(a)) is considered since this structure was shown to be the most energetically favourable one [55]. To investigate the effect of metal adsorbates on the electronic properties of fluorographene a metal atom is placed on top of the 4×4 FG supercell. In the case of F4-TCNQ molecule the 6×6 FG supercell is used. A vacuum of 25 Å is included above the fluorinated graphene layer and separates the layers in the stack from each other. Integration over the Brillouin zone (BZ) is carried out within the Monkhorst-Pack sampling scheme [110] using 12×12×1 and 8×8×1 grids for the 4×4 and 6×6 supercells, respectively.

5.3 Structural and electronic properties of fluorographene

Fluorographene is a stoichiometric derivative of graphene with each carbon atom covalently bonded to fluorine. The configuration in which carbon atoms from two graphene sublattices are bonded to fluorine atoms on different sites of a graphene layer was shown to be the most energetically favourable and is called the chair fluorographene configuration (Fig. 5.1).

Table 5.1 shows the structural parameters of fluorographene derived from the present calculations and those from earlier theoretical and experimental works. The calculated value

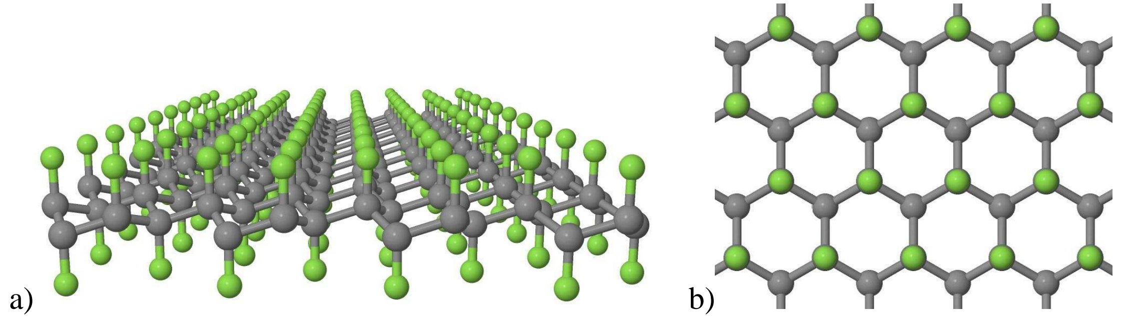

Figure 5.1: Schematic representation of the fluorographene atomic structure: (a) side view and (b) top view. Dark grey and green (light grey) spheres represent carbon and fluorine atoms respectively.

Table 5.1: Structural parameters and electron energy gap (E_g) for fluorographene derived from the present calculations. The values from the other theoretical and experimental works are shown for comparison. The FG lattice constant, a_0, and the C-C and C-F bond lengths, d_{CF} and d_{CC}, are shown in angstroms (Å). The angles between bonds, θ_{CCF} and θ_{CCC}, are in degrees.

	Reference	a_0, Å	d_{CF}, Å	d_{CC}, Å	θ_{CCF}	θ_{CCC}	E_g, eV
Theory							
LDA	This work	2.55	1.361	1.552	108.3	110.6	3.1
GGA	Leenaerts *et al.* [55]	2.60	1.371	1.579	108.1	110.8	3.2
	Boukhvalov *et al.* [47]	–	–	1.559	–	–	4.2
GW	Leenaerts *et al.* [55]	–	–	–	–	–	7.4
	Klintenberg *et al.* [178]	–	–	–	–	–	7.4
Experiment							
TEM	Nair *et al.* [51]	2.48	–	–	–	–	3
XRD	Cheng *et al.* [52]	2.57[a]	–	–	–	–	–

[a]The lattice constant was measured for 100% fluorinated SP-1 graphite powder.

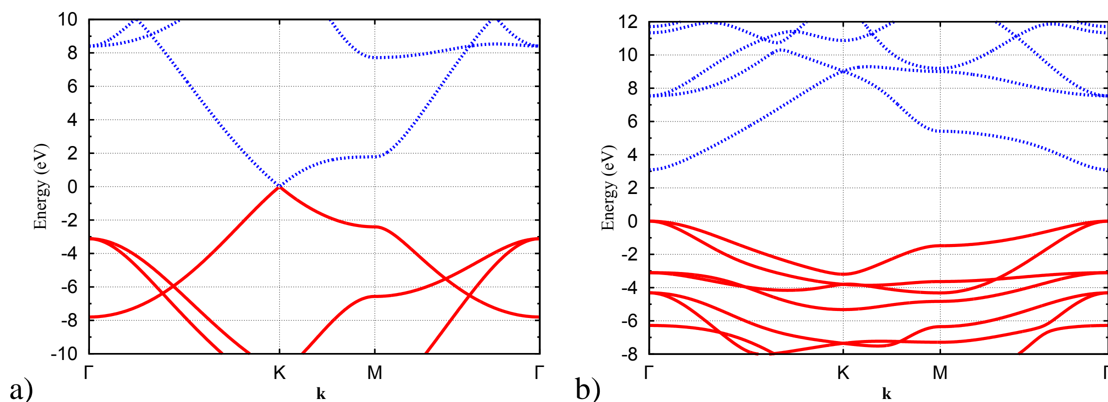

Figure 5.2: Calculated electronic band structure of (a) graphene and (b) fluorographene. Red solid lines represent occupied states, while blue dashed lines represent empty states. The zero of the energy scale is set to the Fermi level in (a) and to the valence band maximum in (b).

of the FG lattice constant is 2.55 Å which is 4.5% larger than that calculated for a pristine graphene, 2.44 Å. This is in a good agreement with X-ray Diffraction (XRD) data, which showed a 4.5% difference between the values of in-plane lattice constant for 100% fluorinated and for pristine SP-1 graphite powder, 2.57 Å and 2.46 Å, respectively [52]. However, only a 1% change of the lattice constant was reported for fully fluorinated monolayer graphene from electron diffraction measurements [51]. The authors attributed this to the possibility of much stronger out-of-plane corrugations for 2D fluorographene layer than for 3D graphite. However, such corrugations cannot be predicted by our calculations.

Figure. 5.2 shows the calculated electronic band structures of graphene and fluorographene. In the case of FG the formation of the C-F covalent bonds changes the electronic configuration of graphene carbon atoms from sp^2 to sp^3. This removes graphene related π bands from the electronic structure of fluorographene and results in the appearance of an energy gap. The value of the band gap at Γ was found to be 3.1 eV, which is in good agrrement with previously reported DFT results (see Table 5.1). However, it is well known that band gap values calculated with the application of DFT are underestimated. Calculations based

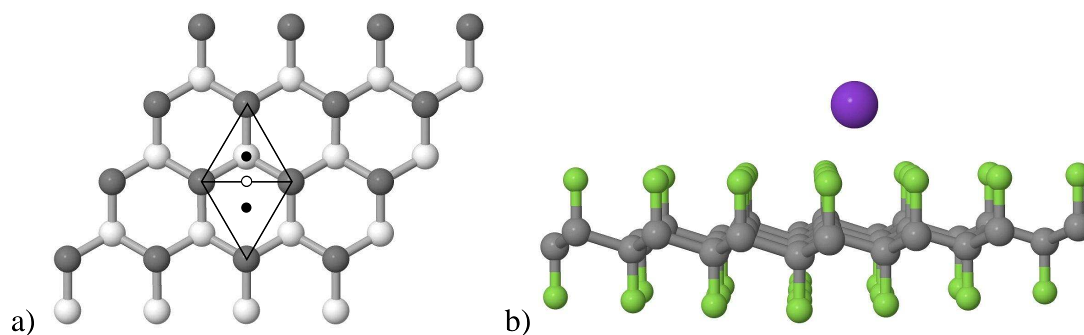

Figure 5.3: (a) Schematic representation of 4×4 fluorographene supercell. Dark grey and light grey spheres represent C-F units with fluorine atoms above and below the fluorographene plane, respectively. Small filled circles show the most favorable adsorption sites for metal atoms on FG, which are above the centre of triangles formed by the three nearest fluorine atoms. Positions marked by opened circle and those directly above the fluorine atoms are less favorable. (b) Side view of fluorographene with an adsorbed metal atom.

on the GW approximation predict the energy gap of 7.4 eV for the chair configuration of FG [55, 178]. The experimental value of 3 eV has been reported for the optical gap of FG [51]. This value, however, might be smaller than the real energy gap due to excitonic effects [51] or possibly the effect of disorder.

5.4 K, Li and Au atoms on fluorographene

The considered adsorption sites for metal atoms on fluorographene are shown in Fig. 5.3(a). The most favourable position for all the metal atoms is found above the centre of a triangle formed by the three nearest fluorine atoms. The calculated values of binding energy and optimum height for K, Li and Au atoms above the FG layer are given in Table 5.2. The value obtained for the binding energy for the K atom on FG, 2.22 eV, is higher than the value reported for the K atom on pristine graphene, 1.51 eV, which was derived from the similar DFT-LDA calculations [172]. This indicates slightly stronger interaction of the K

Table 5.2: Experimental values of the ionization energy (IE) of metal atoms [131] and calculated values of the binding energy, E_b, optimum height, h, and magnetic moment, M, for the metal atoms and F4-TCNQ at the most favourable adsorption site on top of fluorographene. The heights are calculated with respect to the top fluorine atoms. The type of doping due to the adsorbates is also shown.

	IE[a], eV	E_b, eV	h, Å	M, μ_B	Doping
K	4.34	2.22	1.92	0	n-type
Li	5.39	2.38	1.05	0	n-type
Au	9.23	0.24	2.52	1	-
F4-TCNQ		1.02	2.48/2.78[a]	0	-

[a]The values are for the smallest distance (between N atoms and the FG surface) and the average distance between F4-TCNQ and FG.

atom with FG than with a pristine graphene. The opposite effect is observed in the case of Au atom: the binding energies are 0.24 eV and 0.65 eV for the adsorption on FG and pristine graphene, respectively. Such a low value of the binding energy for gold indicates a very low stability of this metal on the fluorinated graphene surface.

Figures 5.4(a) and 5.4(b) show the band structures of pristine fluorographene and fluorographene with the adsorbed K atom. The adsorption has resulted in the appearance of a half-filled band close to the conduction band of FG. An analysis of the band structure shows that the K atom adsorption partially lifts the degeneracy of the levels at the bottom of the conduction band at the K and M points of the Brillouin zone. This indicates that the observed half-filled band arises from the splitting of the conduction band of FG by the dopant. To investigate further, the wave functions were calculated at Γ for the lowest level of the conduction band of FG (point A in Fig. 5.4(a)) and for the half-filled level of FG with the adsorbed K atom (point B in Fig. 5.4(b)) . The wave functions appear to be very similar and are delocalized over the carbon and fluorine atoms (see Fig. 5.5). This result

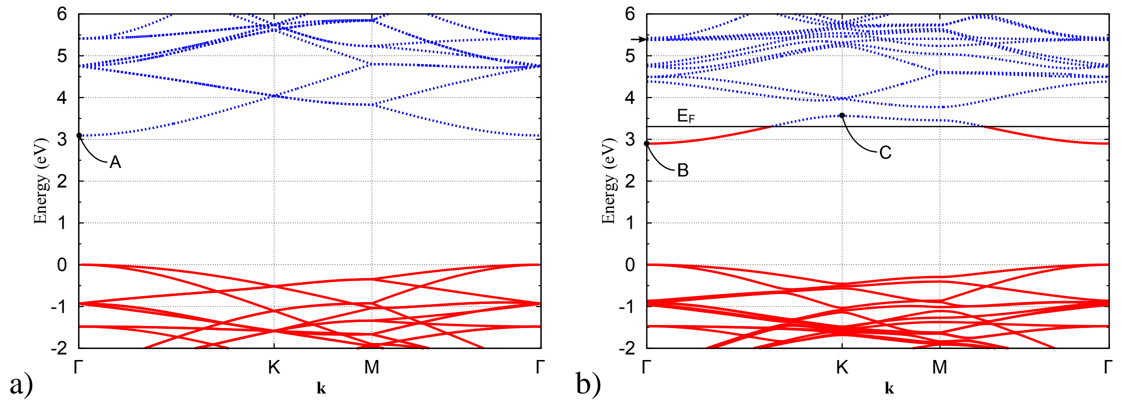

Figure 5.4: The calculated electronic band structure of (a) the 4×4 fluorographene supercell, and (b) fluorographene with an adsorbed K atom. Red solid lines represent occupied states, while blue dashed lines represent empty states. The valence band maximum is set to zero. The Fermi level in (b) is shown with a black solid line and labeled as E_F. The arrow points at the position of the potassium $4s^1$ level. Points labeled as A, B and C are the points at which wave functions are calculated.

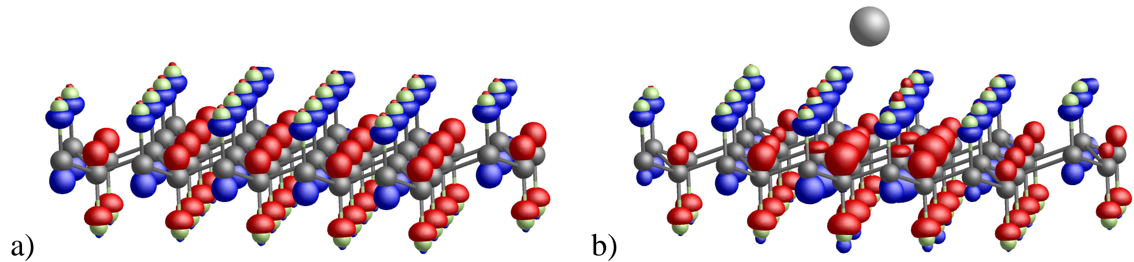

Figure 5.5: Plot of the real part of the wave function for (a) fluorographene at point A in Fig. 5.4(a) and (b) for fluorographene with the adsorbed K atom at point B in Fig. 5.4(b). Carbon atoms are shown in dark grey color, while fluorine atoms are in green (light grey) color. Red and blue colors correspond to the different signs of the wave function. Note that the state in (a) is empty while the same delocalized state is occupied in (b) showing that doping has occured.

demonstrates that the wave functions at both points correspond to the same energy level of FG, which is empty for pristine FG and becomes occupied after the adsorption of the K atom. The potassium $4s^1$ level, which is the highest occupied level for an isolated K atom, is found at about 5.4 eV above the valence band maximum and is empty (see Fig. 5.4(b)). These results indicate that the charge transfer occurs from the K atom to fluorographene and, thus, free electrons are introduced into the system.

It should be noted, that the wave function for the half-filled band at Γ (point B in Fig. 5.4(b)) is not distributed uniformly. Fig. 5.6(a) shows the wave function at B with the smaller isosurface value than in Fig. 5.4(d). The amplitude of the wave function is higher on the C and F atoms below the K atom and decreases to the periphery of the cell, indicating partial localization of the charge. We attribute this to the Coulomb interaction between the positively charged K ion and the negative charge on fluorographene. Interestingly, the wave function for the same level but at the K point of the BZ, labeled as C in Fig. 5.4(b), is nearly localized in the small region of FG below the K ion (Fig. 5.6(b)). The possible explanation of this phenomenon is that in pristine fluorographene the bottom of the conduction band at the K point of the BZ is three fold degenerate (Fig. 5.4(a)). The wave functions for each degenerate energy level have a build-up of the amplitude at different parts of the super cell (not shown). When the degeneracy is lifted by the adsorption of the K atom (Fig. 5.4(b)) the behavior of the wave function for each level is in general conserved: the distribution of the wave function is not uniform within the cell, although its exact form and the position of the amplitude peak is now slightly changed. Redistribution of the wave function at point C (Fig. 5.4(b)), such that it becomes largely localized below the K ion, is probably due to the electrostatic interaction with the positive K ion. However, it should be stressed that the wave functions for the levels at the bottom of the conduction band are distributed only on fluorographene and not on the K atom. This means that the splitting of the conduction band is not due to the overlap with potassium levels.

The adsorption of the Li atom results in the similar changes in the electronic band struc-

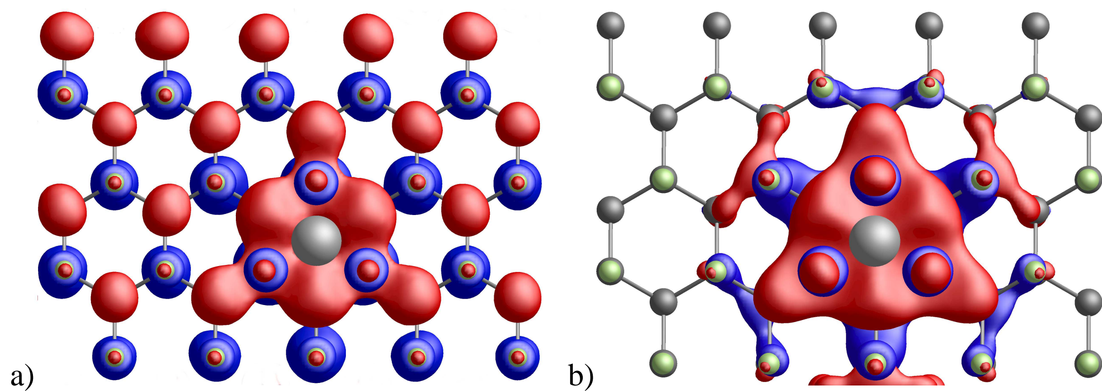

Figure 5.6: Plot of the real part of the wave function for the half-filled metallic level of fluorographene with the adsorbed K atom at a) point B and b) point C of the bandstructure shown in Fig. 5.4(b). Carbon atoms are shown in dark grey color, while fluorine atoms are in green (light grey) color. Red and blue colors correspond to the different signs of the wave function.

ture of FG (not shown) as in the case of the K atom adsorption, suggesting that Li also acts as a donor for fluorographene. However, the magnitude of the conduction band splitting and the dispersion of the half-filled band is slightly different for FG doped by the K and Li atoms. In the case of the K atom adsorption the splitting of the conduction band at the K point of the BZ is 0.41 eV, and the energy difference for the half-filled band between Γ and K points is 0.66 eV. In the case of doping by Li both values are 0.55 eV.

Fig. 5.7 shows spin-up and spin-down electronic band structures of an Au atom on fluorographene. The flat bands within the energy gap of fuorographene originate from the Au atom orbitals. The highest occupied band corresponds to the $6s^1$-Au level, which is the highest filled level for an isolated Au atom, and it lies 1.27 eV below the conduction band of FG. Thus, no charge transfer occurs from gold to fluorographene. The adsorption of an Au atom does, however, lead to a magnetic moment of about 1 Bohr magneton.

The results obtained are also consistent with the differences in the binding energy for the metallic atoms on FG and pristine graphene mentioned earlier. Since the fluorine atoms

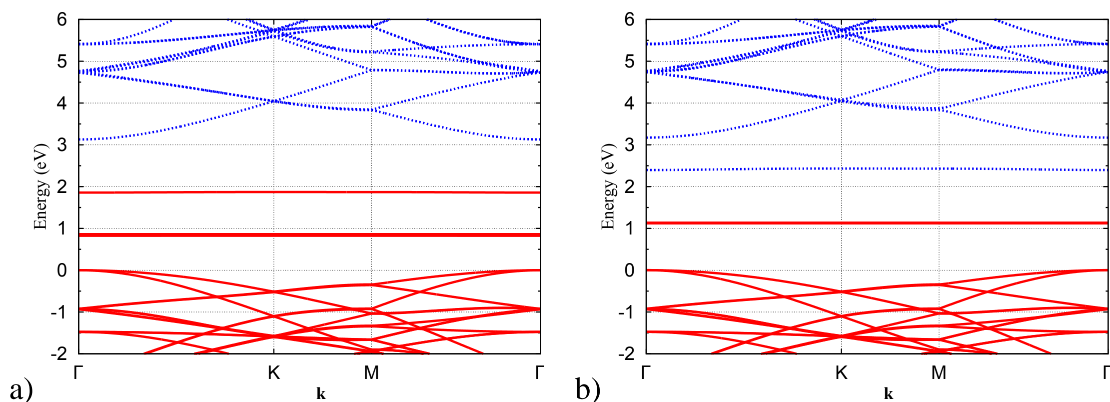

Figure 5.7: (a) Spin-up and (b) spin-down band structures for fluorographene with the adsorbed Au atom. Red solid lines represent occupied states, while blue dashed lines represent empty states. The valence band maximum is set to zero.

in FG are negatively charged due to the higher electronegativity of F compared to C, the stronger binding of the K atom on FG can be explained by the additional Coulomb attraction between the negatively charged F atoms and the positive metal ion. For the Au atom adsorption the absence of ionic or covalent bonding with FG or graphene explains the small values of the binding energy. However, in the case of Au on pristine graphene the strong hybridization between Au $6s^1$ level and graphene π bands occurs [172]. This results in stronger interaction of Au with the pristine graphene than with FG.

5.5 F4-TCNQ on fluorographene

The molecular structure of F4-TCNQ is shown in Fig. 5.8(a). The electron affinity of F4-TCNQ was estimated to be 5.25 eV from the position of the lowest unoccupied molecular orbital (LUMO) level relative to the vacuum level. The calculated value is in very good agreement with that obtained from photoemission spectroscopy measurements, 5.24 eV [179]. The molecule was placed parallel to the FG surface. However, after structural optimization the molecule became slightly bent with the N atoms moved closer to the FG

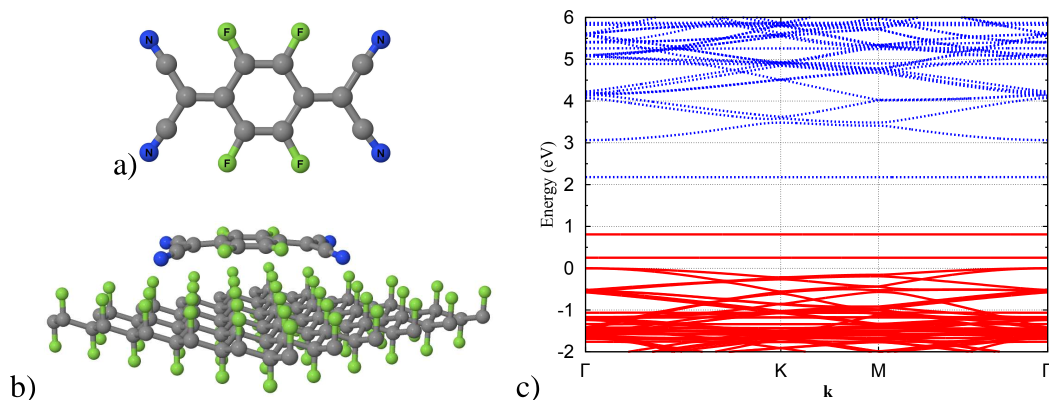

Figure 5.8: (a) Molecular structure of F4-TCNQ and (b) F4-TCNQ on top of fluorographene. Carbon atoms are shown in grey color. Fluorine and nitrogen atoms are represented with green and blue colors and labeled as F and N respectively. (c) Electronic band structure of fluorographene with the F4-TCNQ molecule. Red solid lines represent occupied states, while blue dashed lines represent empty states. The valence band maximum is set to zero.

surface (Fig. 5.8(b)). The height of the atoms in the molecule relative to FG varies within 0.49 Å. We have tested four orientations and positions of the F4-TCNQ molecule on FG in *xy*-plane. For the considered configurations the binding energy varies within only 45 meV. The height and the binding energy of F4-TCNQ at the most favourable adsorption site on FG are given in Table 5.2.

The electronic band structure of FG with the F4-TCNQ molecule is shown in Fig. 5.8(c). Adsorption of F4-TCNQ results in the appearance of the two filled levels at 0.25 and 0.81 eV above the valence band of FG. The LUMO level lies 2.2 eV above the valence band maximum indicating that no charge transfer occurs from FG to F4-TCNQ. The calculated value of the electron affinity for F4-TCNQ on FG is 5.1 eV, which is very close to that for the separate F4-TCNQ molecule, 5.25 eV. This implies that the energies of F4-TCNQ electronic levels are only slightly affected by the FG surface potential. The work function of fluorographene was estimated to be 7.3 eV from the position of the valence band max-

imum relative to the vacuum level. Thus, only the adsorbates with the electron affinities higher than (or close to) 7.3 eV can induce p-type doping of fluorographene.

5.6 Effect of doping on structural parameters of fluorographene

Recently, in the theoretical investigation of diluted F atoms on graphene, Sofo *et al*. [180] have shown that doping has a strong effect on the nature of the C-F bond. It was shown that high electron doping induces a transformation of the electronic configuration of C from sp^3 towards sp^2. To investigate this, the changes in the structural parameters caused by the adsorption of metal atoms were examined. It is found that structural parameters of FG are changed in the cases of K and Li atoms adsorption, while no changes are observed for FG with an Au atom. The structural changes induced by the adsorption of K and Li atoms are larger beneath the positive metal ions while at the periphery of the cell the bonds lengths and angles only slightly differ from those for pristine FG (Table 5.3). Such distribution of the structural changes correlates with the distribution of the electron wave function in FG, which shows a partial localization below the metal ions (Fig. 5.6). This suggests that the structural changes are related to the extra negative charge on FG due to doping. On the other hand, the changes in structural parameters can be caused by the Coulomb interaction between a positive metal ion and negatively charged F atoms. To separate the effects of the doping and Coulomb forces we have investigated the negatively charged FG with no metal atom deposited on it. In this case the negative charge of 1 e is distributed uniformly over all C-F units in the FG cell, while the compensating positive charge is spread over the background. The calculated structural parameters in this case are between the values found for FG beneath the metal ion and at the periphery of the cell (Table 5.3). The decrease in the C-C bond length and increase in the θ_{CCC} angle correspond to a change of electronic configuration of the carbon atoms from sp^3 towards

Table 5.3: Structural parameters calculated for pristine fluorographene, for fluorographene with the negative charge of 1 e added to the 4×4 cell and for fluorographene beneath the adsorbed metallic atom.

FG structure	d_{CF}, Å	d_{CC}, Å	θ_{CCF}	θ_{CCC}
pristine	1.361	1.552	108.31	110.61
+1 e	1.376	1.547	107.81	111.09
with K	1.420	1.538	107.15	112.11
with Li	1.452	1.535	106.84	112.50

sp^2 due to the electron doping in agreement with *et al.* [180]. The latter results confirm the dependence of structural changes in FG on doping. On the other hand, the presence of a metal ion affects the distribution of the extra charge on FG. Together with the Coulomb interaction between the positive metal ion and negatively charged F atoms this results in the larger changes beneath the metal ion than at the periphery of the cell.

5.7 Conclusions

In this chapter doping of fluorographene (FG) by surface adsorbates has been studied with the use of density functional theory. It is shown that FG can be doped with electrons by the deposition of metal atoms with a low value of ionization energy, such as K and Li. Adsorption of K or Li atoms results in the splitting of the FG conduction band by about 0.4-0.5 eV. Plots of the wave functions suggest that there is a build-up of the negative charge in FG beneath a positive metal ion. The doping results in changes in bonds lengths and angles in FG which correspond to the change of electronic configuration of the carbon atoms from sp^3 towards sp^2. It has also been shown that adsorption of metal atoms with a high value of the ionization energy, such as Au, results in the appearance of deep levels

within the energy gap of fluorographene. According to our calculations, adsorption of F4-TCNQ molecule, which is known to be an efficient acceptor for graphene, nanotubes and diamond, does not result in doping of fluorographene. Although F4-TCNQ has a high electron affinity of 5.2 eV, that value is much lower than the fluorographene work function, which is calculated to be 7.3 eV. Such a high value of the work function suggests that p-type doping of fluorographene is difficult to achieve, since adsorbates with electron affinities higher than 7.3 eV are required.

Chapter 6

Concluding remarks

This thesis presents results of density functional theory studies of graphene interactions with SiC and diamond substrates and interactions of fluorographene with metallic and molecular surface adsorbates. The main aims of the work were: 1) to investigate the influence of different substrates on graphene electronic properties; 2) to understand mechanism of graphene decoupling from the SiC(0001) substrate by intercalation of hydrogen and fluorine into graphene/SiC interface; 3) to find ways for doping fluorographene.

6.1 Summary

6.1.1 Graphene on SiC(0001) substrates

Problems related to epitaxial growth of graphene layers on SiC(0001) substrates have been considered in Chapter 3. Recent experimental and theoretical studies showed that the electronic properties of epitaxial graphene on the Si face of SiC are strongly modified by the interaction with the substrate. The first graphene layer grown on SiC(0001) is partially sp^3-hybridized by covalent bonds with the substrate Si atoms and no linear

dispersion of π-bands characteristic for free standing graphene is observed. This interface graphene layer is non conductive and is often called buffer layer. Moreover, the next graphene layer above the buffer layer is electron doped and mobility of charge carriers in this layer does not exceed 2000 cm^2/Vs at low temperatures. This is very low compared to typical value of 20,000 cm^2/Vs for charge carriers mobility in graphene on SiO_2. Further experiments showed that treatments of the graphene/SiC(0001) structures in hydrogen or fluorine gas containing ambients at elevated temperatures could result in decoupling of the graphene layers from the SiC substrate. The decoupled graphene layers were shown to have electronic properties similar to those for free standing graphene. Details of hydrogen and fluorine intercalation into the graphene/SiC(0001) interface were not well understood and have been studied in the present work.

Modeling of epitaxial graphene on SiC(0001) is associated with some difficulties. A unit cell, that is required to reproduce a real surface reconstruction of the graphene/SiC interface, is too big for realistic calculations. Two simplified models have been proposed before and their suitability for calculations of different properties of the graphene/SiC structures was discussed here in detail.

Further, the electronic and structural properties of graphene on H- and F-passivated SiC(0001) surfaces have been studied. First, it was found that the total energy of these structures is lower than that for graphene covalently bound to the substrate plus separate gas molecules. This means that provided the hydrogen and fluorine atoms or molecules can reach the interfacial region the intercalation process and decoupling of the graphene layer is energetically favourable. The binding energies per C atom of the decoupled graphene layers to the passivated SiC substrates were calculated to be about 30 meV, indicating weak graphene to substrate interaction. Moreover, the electronic structure of the decoupled layers was found to be similar to those for free standing graphene. In agreement with experimental results it was found that the graphene layer on the F-passivated SiC(0001) is p-type doped, while no doping occurs in the case of graphene on the H-passivated SiC surface.

To investigate possible ways for hydrogen penetration between epitaxial graphene layers and SiC substrate the energy barriers for H and H_2 migration through graphene layers with no defects and those containing Stone-Wales defect, or two- and four-vacancy clusters have been calculated. The obtained results show that the presence of hollow defects in graphene layers is necessary for hydrogen diffusion through the layers in the temperature range where the decoupling of graphene from the SiC substrates was observed. In practice these defects can be grain boundaries, sample edges or open core screw dislocations, which penetrate several graphene layers. Migration of hydrogen atoms and molecules along graphene/SiC interface was further considered. For both H and H_2 this process is not associated with any significant energy barrier. Thus, once penetrated through the interfacial graphene layer hydrogen can easily migrate along the interface, break covalent bonds between the graphene layer and the substrate, and passivate the SiC surface. This results in decoupling of graphene layers from SiC substrates.

6.1.2 Graphene on passivated diamond substrates

The demand for substrates with high surface quality for deposition of graphene layers has brought diamond into consideration as a substrate material. Further, it is very tempting to combine the unique electronic properties of graphene and optical properties of diamond for designing ultrafast optoelectronic devices. To realize potential applications of graphene/diamond heterostructures better understanding of their electronic properties is required. So, electronic properties of single- and double-layer graphene on the hydrogen-, fluorine- and hydroxyl-terminated diamond substrates with (111) surface orientation have been considered in the present work.

First, effects of different terminations on the electronic properties of diamond surfaces have been studied. It is found that all terminating species effectively saturates the surface C atoms, removing the π states of the clean surface from the bandgap of diamond. The

difference in the electronegativity of C atoms and passivating species results in the appearance of a dipole layer on the surface. The electric field due to this dipole layer shifts the electronic energy bands upwards or downwards in energy compared to their position for the clean surface. For the hydrogen-terminated surfaces this effect results in significant upward shift of the electronic bands and leads to the negative electron affinity observed experimentally and found in other theoretical works. In contrast, F-termination results in downward energy shift of electron states and large positive electron affinity.

The interactions between graphene layers and the passivated diamond surfaces were found to be weak, so that the electronic structures of graphene is almost not affected and the linear dispersion of π-bands is preserved. Thus, graphene layers on these substrates can be considered as quasi-free-standing. For graphene on the hydrogenated diamond surfaces, charge transfer was found to occur. This results in n-type doping of graphene layers and p-type doping of the substrate. For bilayer graphene the doping leads to the appearance of 150 meV energy gap between conduction and valence bands. No charge transfer and no doping was found for graphene layers on the F- and OH-passivated surfaces.

It is interesting to compare results obtained for graphene on diamond and SiC surfaces. In both cases the interactions of graphene with passivated substrates were found to be very weak, and graphene electronic structure is very similar to that for a free standing layer. Moreover, for different substrate passivations graphene layer can be either doped or undoped. In the case of the SiC substrates, graphene layer is p-type doped on the fluorinated surfaces while no doping occurs for graphene on the hydrogenated surfaces. For diamond substrates, n-type doping occurs for graphene on the H-passivated surfaces, while no charge transfer was found for other passivating species. Thus, passivation of a substrate is an effective method to avoid strong graphene/substrate interactions, hence preserve the high transport quality of graphene, and to control type of doping of graphene layers.

6.1.3 Doping of fluorographene by surface adsorbates

Fluorographene is formed by ordered arrangement of fluorine atoms on both sides of a graphene layer. It was shown to be a high quality insulator with a wide range of potential applications. For successful applications in electronics doping of fluorographene with free charge carriers is required. In order to investigate the possibility of doping fluorographene by surface adsorbates effects of several metals and F4-TCNQ molecule on the electronic properties of fluorographene have been studied.

It is found that deposition of metal atoms with low values of ionization energy, such as potassium and lithium, results in effective n-type doping of fluorographene. While adsorption of metal atoms with high values of ionization energy, such as gold, results in the appearance of deep levels within the fluorographene energy gap and no doping occurs. The p-type doping of fluorographene is, however, extremely difficult to achieve. The ionization energy of fluorographene has been calculated to be 7.3 eV. This means that for p-type doping of fluorographene by surface adsorbates highly electronegative materials with electron affinities higher than 7.3 eV are required. The F4-TCNQ molecule has one of the largest electron affinities among known materials, which is 5.2 eV. This is, however, much lower than the fluorographene ionization energy and adsorption of this molecule does not result in p-type doping of fluorographene.

6.2 Outlook

The results of the calculations obtained in the present work are, in general, consistent with the available experimental and theoretical results on electronic properties of graphene-related structures. So, the suitability of density-functional-theory calculations with the use of AIMPRO code for analysis of structural and electronic properties of graphene and various graphene derivatives is confirmed. We expect that the results of our calculations

will be useful for researchers dealing with graphene and for electronic engineers who design graphene-based devices with required functional characteristics.

Clearly, possibilities to modify properties of graphene, and, more general, other nanostructures, provides a fertile background for exciting research for physicists, chemists and materials engineers. Following the results obtained in the present work some directions of research can be suggested.

Mechanisms of epitaxial growth of graphene layers on the SiC substrates are not fully understood. It is known that at high temperatures Si atoms sublime from the SiC surface, while remaining C atoms rearrange into graphene honeycomb structure. However, ways for Si atoms to escape from the interfacial region between carbon layers and the surface are not clear. We have shown that to explain hydrogen intercalation into the graphene/SiC interface the presence of the hollow defects in the graphene layers is necessary. Such defects can also provide ways for Si atoms to move away from the interfacial region. Examining of this assumption is an interesting and challenging problem which requires close collaboration between theorists and experimentalists.

Regarding graphene layers on the passivated substrates, there are a lot of interesting problems that deserve attention. It is important to investigate effects that can arise when some of the surface atoms are not passivated on the graphene electronic properties. In principle, these atoms have dangling bonds that can introduce electron levels into the substrate band gap and leads to doping of graphene layers. It will be interesting to investigate effects of mixed surface passivation, when some of the surface atoms are passivated with one chemical species and the rest with another. Effects of different bulk defects close to the surface, such as NV^- in diamond, are also of high interest.

In the present work effects only of a few surface adsorbates on fluorographene properties has been studied mainly in order to search for a potential transfer dopants. There are many other possible dopants, including metals and organic molecules, that will be interesting to investigate. However, it is even more important to study effects of materials that are

involved in fabrication of electronic devices on the base of fluorographene. Particularly, interactions of fluorographene with Ti and Cr, that are often used for metallic contacts. p-type doping of fluorographene is also a challenging problem.

It has been recently shown that the presence of transition metals atoms and oxygen on graphene results in formation of vacancies clusters in graphene lattice. This was successfully used for cutting graphene nanostructures of different shape by transition metals nanoparticles. However, this can also lead to degradation of graphene-based electronic devices due to the presence of transition metals atoms in metallic contacts. This problem has a long history and has been previously studied for graphite. However, mechanisms of catalytic oxidation of graphite and graphene are not fully understood and requires more experimental and theoretical studies.

Structures consisting of few layers graphene are also of great interest. Intercalation of different chemical species between graphene layers provide ways to design, in principle, new materials with required properties. *Ab initio* calculations can be used for investigation and prediction of the properties of such structures.

There is also a growing research interest in other two-dimensional materials, such as MoS_2 or BN. Investigation of structural defects in these materials and ways to modify their electronic properties is a demanding task.

Clearly, much more theoretical and experimental research has to be done to get a full advantage of graphene unique properties for practical applications. In this respect, *ab-initio* methods provide a powerful tool to investigate effects of different substrates and adsorbates on graphene electronic properties and to find ways for their predictable and controllable modification.

Bibliography

[1] P. R. Wallace, Phys. Rev. **71**, 622 (1947).

[2] L. D. Landau, Phys. Z. Sowjetunion **11**, 26 (1937).

[3] R. E. Peierls, Ann. I. H. Poincare **5**, 177 (1935).

[4] K. S. Novoselov, A. K. Geim, S. V. Morozov, D. Jiang, Y. Zhang, S. V. Dubonos, I. V. Grigorieva, and A. A. Firsov, Science **306**, 666 (2004).

[5] A. K. Geim and K. S. Novoselov, Nature Materials **6**, 183 (2007).

[6] J. C. Charlier, P. C. Eklund, J. Zhu, and A. C. Ferrari, Top. Appl. Phys. **111**, 673 (2008).

[7] Y. Zhang, Y.-W. Tan, H. L. Stormer, and H. L. Kim, Nature **438**, 201 (2005).

[8] X. Du, I. Skachko, F. Duerr, A. Luican, and E. Y. Andrei, Nature **462**, 192 (2009).

[9] A. S. Mayorov, D. C. Elias, I. S. Mukhin, S. V. Morozov, L. A. Ponomarenko, K. S. Novoselov, A. K. Geim, and R. V. Gorbachev, Nano Lett. **12**, 4629 (2012)

[10] F. Bonaccorso, Z. Sun, T. Hasan, and A. C. Ferrari, Nat. Photon **4**, 611 (2010).

[11] C. Casiraghi, A. Hartschuh, E. Lidorikis, H. Qian, H. Harutyunyan, T. Gokus, K. S. Novoselov, and A. C. Ferrari, Nano Lett., **7(9)**, 2711 (2007).

[12] I.W. Frank, D.M. Tanenbaum, A.M. van der Zande, and P.L. McEuen,

[13] A. H. Castro Neto, F. Guinea, N. M. R. Peres, K. S. Novoselov, A. K. Geim, Rev. Mod. Phys. **81**, 109 (2009).

[14] P. W. Atkins, *Physical Chemistry*, 5th ed. (Oxford University Press, Oxford, 1997).

[15] M. I. Katsnelson, K. S. Novoselov, A. K. Geim, *Nature Phys.* **2**, 620 (2006).

[16] A. Bostwick, T. Ohta, T. Seyller, K. Horn, E. Rotenberg, Nature Phys. **3**, 36 (2007).

[17] K. S. Novoselov, A. K. Geim, S. V. Morozov, D. Jiang, M. I. Katsnelson, I. V. Grigorieva, S. V. Dubonos, and A. A. Firsov, Nature **438**, 197 (2005).

[18] A. F. Young, and P. Kim, Nature Phys. **5(3)**, 222 (2009).

[19] K. S. Novoselov, Z. Jiang, Y. Zhang, S. V. Morozov, H. L. Stormer, U. Zeitler, J. C. Maan, G. S. Boebinger, P. Kim, and A. K. Geim, Science **315**, 1379 (2007).

[20] K. S. Novoselov, D. Jiang, F. Shedin, T. J. Booth, V. V. Khotkevich, S. V. Morozov, and A. K. Geim, PNAS **102**, 10451 (2005).

[21] P. Blake, E. W. Hill, A. H. C. Neto, K. S. Novoselov, D. Jiang, R. Yang, T. J. Booth, and A. K. Geim, Appl. Phys. Lett. **91**, 063124 (2007).

[22] M. S. Fuhrer, C. N. Lau, and A. H. MacDonald, MRS Bulletin **35**, 289 (2010).

[23] M. Choucair, P. Thordarson, and J. A. Stride, Nature Nanotech. **4**, 30-33 (2009).

[24] C. Berger, Z. M. Song, T. B. Li, X. B. Li, A. Y. Ogbazghi, R. Feng, Z. T. Dai, A. N. Marchenkov, E. H. Conrad, P. N. First, and W. A. de Heer, J. Phys. Chem. B **108**, 19912 (2004).

[25] C. Berger, Z. M. Song, X. B. Li, X. S. Wu, N. Brown, C. Naud, D. Mayo, T. B. Li, J. Hass, A. N. Marchenkov, E. H. Conrad, P. N. First, and W. A. de Heer, Science **312**, 1191 (2006).

[26] K. S. Kim, Y. Zhao, H. Jang, S. Y. Lee, J. M. Kim, J. H. Ahn, P. Kim, J. Y. Choi, and B. H. Hong, Nature **457**, 706 (2009).

[27] A. Reina, X. T. Jia, J. Ho, D. Nezich, H. B. Son, V. Bulovic, M. S. Dresselhaus, and J. Kong, Nano Lett. **9**, 30 (2009).

[28] X. S. Li, W. W. Cai, J. H. An, S. Kim, J. Nah, D. X. Yang, R. Piner, A. Velamakanni, I. Jung, E. Tutuc, S. K. Banerjee, L. Colombo, and R. S. Ruoff, Science **324**, 1312 (2009).

[29] H. Liu, Y. Liu, and D. Zhu, J. Mater. Chem. **21**, 3335 (2011).

[30] C. R. Dean, A. F. Young, I. Meric, C. Lee, L. Wang, S. Sorgenfrei, K. Watanabe, T. Taniguchi, P. Kim, K. L. Shepard, and J. Hone, Nat. Nanotechnol. **5**, 722 (2010).

[31] L. S. Panchokarla, K. S. Subrahmanyam, S. K. Saha, A. Govindaraj, H. R. Krishnamurthy, U. V. Waghmare, and C. N. R. Rao, Adv. Mater. **21**, 4726 (2009).

[32] D. C. Wei, Y. Q. Liu, Y. Wang, H. L. Zhang, L. P. Huang and G. Yu, Nano Lett. **9**, 1752 (2009).

[33] E. H. Hwang, S. Adam, and S. Das Sarma, Phys. Rev. Let. **98**, 186806 (2007).

[34] J. H. Chen, C. Jang, S. Xiao, M. Ishigami, and M. S. Fuhrer, Nature Nanotech. **3**, 206 (2008).

[35] D. C. Elias, R. V. Gorbachev, A. S. Mayorov, S. V. Morozov, A. A. Zhukov, P. Blake, L. A. Ponomarenko, I. V. Grigorieva, K. S. Novoselov, F. Guinea, and A. K. Geim, Nat. Phys. **7**, 701 (2011).

[36] C. R. Dean, A. F. Young, I. Meric, C. Lee, L. Wang, S. Sorgenfrei, K. Watanabe, T. Taniguchi, P. Kim, K. L. Shepard, and J. Hone, Nat. Nanotechnol. **5**, 722 (2010).

[37] A. S. Mayorov, R. V. Gorbachev, S. V. Morozov, L. Britnell, R. Jalil, L. A. Ponomarenko, P. Blake, K. S. Novoselov, K. Watanabe, T. Taniguchi, and A. K. Geim, Nano Lett. **11**, 2396 (2011).

[38] M. Orlita, C. Faugeras, P. Plochocka, P. Neugebauer, G. Martinez, D. K. Maude, A.-L. Barra, M. Sprinkle, C. Berger, W. A. de Heer, and M. Potemski, Phys. Rev. Lett. **101**, 267601 (2008).

[39] K. V. Emtsev, F Speck, Th. Seyller, L Ley, and J. D. Riley, Phys. Rev. B **77**, 155303 (2008).

[40] S. Kim, J. Ihm, H. J. Choi, and Y.-W. Son, Phys. Rev. Lett. **100**, 176802 (2008).

[41] C. Riedl, C. Coletti, T. Iwasaki, A. A. Zakharov, and U. Starke, Phys. Rev. Lett. **103**, 246804 (2009).

[42] A. L. Walter, K.-J. Jeon, A. Bostwick, F. Speck, M. Ostler, T. Seyller, L. Moreschini, Y. S. Kim, Y. J. Chang, K. Horn, and E. Rotenberg, Appl. Phys. Lett. **98**, 184102 (2011).

[43] M. Y. Han, B. Ozyilmaz, Y. B. Zhang, and P. Kim, Phys. Rev. Lett. **98**, 206805 (2007).

[44] T. Ohta, A. Bostwick, T. Seyller, K. Horn, and E. Rotenberg, Science **313**, 951 (2006).

[45] J. B. Oostinga, H. B. Heersche, X. Liu, A. F. Morpurgo, and L. M. K. Vandersypen, Nature Materials **7**, 151 (2007).

[46] J. O. Sofo, A. S. Chaudhari, and G. D. Barber, Phys. Rev. B **75**, 153401 (2007).

[47] D. W. Boukhvalov and M. I. Katsnelson, J. Phys.: Condens. Matter **21**, 344205 (2009).

[48] S. Park and R. S. Ruoff, Nat. Nanotechnol. **4**, 217 (2009).

[49] M. H. F. Sluiter, Y. Kawazoe, Phys.Rev. B **68**, 085410 (2003).

[50] D. C. Elias, R. R. Nair, T. M. G. Mohiuddin, S. V. Morozov, P. Blake, M. P. Halsall, A. C. Ferrari, D. W. Boukhvalov, M. I. Katsnelson, A. K. Geim, and K. S. Novoselov, Science **323**, 610 (2009).

[51] R. R. Nair, W. Ren, R. Jalil, I. Riaz, V. G. Kravets, L. Britnell, P. Blake, F. Schedin, A. S. Mayorov, S. Yuan, M. I. Katsnelson, H.-M. Cheng, W. Strupinski, L. G. Bulusheva, A. V. Okotrub, I. V. Grigorieva, A. N. Grigorenko, K. S. Novoselov, and A. K. Geim, Small **6**, 2877 (2010).

[52] S.-H. Cheng, K. Zou, F. Okino, H. R. Gutierrez, A. Gupta, N. Shen, P. C. Eklund, J. O. Sofo, and J. Zhu, Phys. Rev. B **81**, 205435 (2010).

[53] F. Withers, M. Dubois, and A. K. Savchenko, Phys. Rev. B **82**, 073403 (2010).

[54] J. T. Robinson, J. S. Burgess, C. E. Junkermier, S. C. Badescu, T. L. Reinecke, F. K. Perkins, M. K. Zalatudinov, J. W. Baldwin, J. C. Culbertson, P. E. Sheehan, and E. S. Snow, Nano Lett. **10**, 3001 (2010).

[55] O. Leenaerts, H. Peelaers, A. D. Hernández-Nieves, B. Partoens, and F. M. Peeters, Phys. Rev. B **82**, 195436 (2010).

[56] M. Born, R. Oppenheimer, Ann. Physik **87**, 457 (1925).

[57] J. M. Thijssen, *Computational Physics*, (Cambridge University Press, Cambridge, 1999).

[58] J. K. L. MacDonald, Phys. Rev. **43**, 830 (1933).

[59] P. Hohenberg, W. Kohn, Phys. Rev. B **136**, 864 (1964).

[60] W. Kohn, L. J. Sham, Phys. Rev. A **140**, 1133 (1965).

[61] J. P. Perdew and A. Zunger, Phys. Rev. B **23**(10), 5048 (1981).

[62] J. P. Perdew, *Electronic Structure of Solids 91*, edited by P. Ziesche and H. Eschrig (Akademie Verlag, Berlin, 1991).

[63] J. P. Perdew, K. Burke, and M. Ernzerhof, Phys. Rev. Lett. **77**(18), 3865 (1996).

[64] J. P. Perdew, K. Burke, and Y. Wang, Phys. Rev. B **54**(23), 16533 (1996).

[65] U. von Barth and L. Hedin, J. Phys. Chem. **5**(13), 1629 (1972).

[66] D. Ceperley, Phys. Rev. B **18**(7), 3126 (1978).

[67] S. J. Vosko, L. Wilk, and M. Nusair, Canadian J. Phys. **58**, 1200 (1980).

[68] D. M. Ceperley and B. J. Alder, Phys. Rev. Lett. **45**(7), 566 (1980).

[69] K. Kunc and R. M. Martin, *Ab Initio Calculation of Phonon Spectra*, edited by J. T. Devreese, V. E. van Doren, P. E. van Camp (Plenum, New York, 1 1983).

[70] J. P. Goss, M. J. Shaw, and P. R. Briddon, *Theory of Defects in Semiconductors*, Topics in Applied Physics, Vol. 104, edited by D. A. Drabold and S. K. Estreicher (Springer, Berlin, 2007), Chap. 3.

[71] J. Coutinho, V.P. Markevich, A.R. Peaker, B. Hamilton, S.B. Lastovskii, L.I. Murin, B.G. Svensson, M.J. Rayson, and P.R. Briddon., Phys. Rev. B **86**, 174101 (2012).

[72] J. Andzelm and E. Wimmer, J. Chem. Phys. **96**, 1280 (1992).

[73] B. G. Johnson, P. M. W. Gill, and J. A. Pople, J. Chem. Phys. **98**, 5612 (1993).

[74] W. Koch, M. C. Holthausen, *A Chemists Guide to Density Functional Theory*, 2nd ed., (Wiley-VCH Verlag GmbH, Weinheim, 2001).

[75] In-Ho Lee and R. M. Martin, Phys. Rev. B **56**, 7197 (1997).

[76] S. Kurth, J. P. Perdew, and P. Blaha, Int. J. Quant. Chem. **75**, 889 (1999).

[77] F. London, Trans. Faraday Soc. **33**, 8-26 (1937).

[78] I. E. Dzyaloshinskii, E. M. Lifshitz, and L. P. Pitaevskii, Sov. Phys.-Usp. **4**, 153 (1961).

[79] T. Björkman, A. Gulans, A. V. Krasheninnikov, and R. M. Nieminen, J. Phys.: Condens. Matter **24**, 424218 (2012).

[80] R. Q. Hood, M. Y. Chou, A. J. Williamson, G. Rajagopal, and R. J. Needs, Phys. Rev. B **57**(15), 8972 (1998).

[81] N. Ooi, A. Rairkar, J. B. Adams, Carbon **44**, 231 (2006).

[82] L. Spanu, S. Sorella, and G. Galli, Phys. Rev. Lett. **103**, 196401 (2009).

[83] W. M. C. Foulkes, L. Mitas, R. J. Needs, and G. Rajagopal, Rev. Mod. Phys. **73**, 33 (2001).

[84] N. D. Drummond and R. J. Needs, Phys. Rev. Lett. **99**, 166401 (2007).

[85] P. Nozièeres and D. Pines, Phys. Rev. **111**, 442 (1958).

[86] D. C. Langreth and J. P. Perdew, Phys. Rev. B **15**, 2884 (1977).

[87] M. Dion, H. Rydberg, E. Schröder, D. C. Langreth, and B. I. Lundqvist, Phys. Rev. Lett. **92**, 246401 (2004).

[88] K. Lee, É. D. Murray, L. Kong, B. I. Lundqvist, and D. C. Langreth, Phys. Rev. B **82**, 081101 (2010).

[89] J. P. Perdew, V. N. Staroverov, J. Tao, and G. E. Scuseria, Phys. Rev. A **78**, 052513 (2008).

[90] S. Grimme, J. Comput. Chem. **27**, 1787 (2006).

[91] J.-D. Chai and M. Head-Gordon, Chem. Phys. Lett. **467**, 176 (2008).

[92] S. Grimme, J. Antony, S. Ehrlich, and H. Krieg, J. Chem. Phys. **132**, 154104 (2010).

[93] N. Marom, A. Tkatchenko, M. Rossi, V. V. Gobre, O. Hod, M. Scheffler, and L. Kronik, J. Chem. Theory Comput., **7**, 3944 (2011).

[94] A. Tkatchenko and M. Scheffler, Phys. Rev. Lett. **102**, 073005 (2009).

[95] W. A. Harrison, *Pseudopotentials in the Theory of Metals*, (W. A. Benjamin, Inc., New York, 1966).

[96] D. Brust, *Methods in Computational Physics*, (Academic Press, New York, 1968).

[97] V. Heine, *Solid State Physics*, (Academic Press, New York, 1970).

[98] W. E. Pickett, Comput. Phys. Rep., **9**(3), 115 (1989).

[99] M. Dolg and X. Cao, Chem. Rev. **112**, 403 (2012).

[100] D. R. Hamann, M. Schlüter, and C. Chiang, Phys. Rev. Lett. **43**, 1494 (1979).

[101] G. B. Bachelet, D. R. Hamann, and M. Schlüter, Phys. Rev. B **26**(8), 4199 (1982).

[102] N. Troullier and J. L. Martins, Phys. Rev. B **43**, 1993 (1991).

[103] J. R. Chelikowsky, J. Phys. D: Appl. Phys. **33**, R33 (2000).

[104] D. Vanderbilt, Phys. Rev. B **41** 7892 (1990).

[105] C. Hartwigsen, S. Goedecker, and J. Hutter, Phys. Rev. B **58**(7), 3641 (1998).

[106] R. Jones and P. R. Briddon, Semicond. Semimet. **51**, 287 (1998).

[107] M. J. Rayson and P. R. Briddon, Phys. Rev. B **80**, 205104 (2009).

[108] P. R. Briddon and M. J. Rayson, Phys. Status Solidi B **248** (6), 1309 (2011).

[109] P. R. Briddon and R. Jones, Phys. Stat. Sol. (b) **217**, 131 (2000).

[110] H. J. Monkhorst and J. D. Pack, Phys. Rev. B **13**, 5188 (1976).

[111] J. D. Pack and H. J. Monkhorst, Phys. Rev. B **16(4)**, 1748 (1977).

[112] I. Forbeaux, J.-M. Themlin, and J.-M. Debever, Phys. Rev. B **58**, 16396 (1998).

[113] K. V. Emtsev, A. Bostwick, K. Horn, J. Jobst, G. L. Kellog, L. Ley, J. L. McChesney, T. Ohta, S. A. Reshanov, J. Röhrl, E. Rotenberg, A. K. Schmind, D. Waldmann, H. B. Weber, and T. Seyller, Nature Mat. **8**, 203 (2009).

[114] F. Varchon, P. Mallet, J.-Y. Veuillen, and L. Magaud, Phys. Rev. B **77**, 235412 (2008).

[115] J. P. Goss, P. R. Briddon, N. G. Wright, and A. B. Horsfall, Mater. Sci. Forum **645-648**, 619 (2010)

[116] F. Varchon, R. Feng, J. Hass, X. Li, B. Ngoc Nguyen, C. Naud, P. Mallet, J.-Y. Veuillen, C. Berger, E. H. Conrad, and L. Magaud, Phys. Rev. Lett. **99**, 126805 (2007).

[117] A. Mattausch and O. Pankratov, Phys. Rev. Lett. **99**, 076802 (2007).

[118] J. Hass, F. Varchon, J. E. Millán-Otoya, M. Sprinkle, N. Sharma, W. A. de Heer, C. Berger, P. N. First, L. Magaud, and E. H. Conrad, Phys. Rev. Lett. **100**, 125504 (2008).

[119] M. Sprinkle, D. Siegel, Y. Hu, J. Hicks, A. Tejeda, A. Taleb-Ibrahimi, P. Le Fèvre, F. Bertran, S. Vizzini, H. Enriquez, S. Chiang, P. Soukiassian, C. Berger, W. A. de Heer, A. Lanzara, and E. H. Conrad, Phys. Rev. Lett. **103**, 226803 (2009).

[120] C. Virojanadara, A. A. Zakharov, R. Yakimov, and L. I. Johanson, Surface Science **604**, L4 (2010).

[121] S. Oida, F. R. McFeely, J. B. Hannon, R. M. Tromp, M. Copel, Z. Chen, Y. Sun, D. B. Farmer, and J. Yurkas, Phys. Rev. B **82**, 041411R (2010).

[122] I. Gierz, T. Suzuki, R. T. Weitz, D. S. Lee, B. Krauss, C. Riedl, U. Starke, H. Höchst, J. H. Smet, C. R. Ast, and K. Kern, Phys. Rev. B **81**, 235408 (2010).

[123] B. Premlal, M. Cranney, F. Vonau, D. Aubel, D. Casterman, M. M. De Souza, and L. Simon, Appl. Phys. Lett. **94**, 263115 (2009).

[124] C. Virojanadara, A. A. Zakharov, S. Watcharinyanon, R. Yakimova, and L. I. Johansson, New J. Phys. **12**, 125015 (2010).

[125] C. Virojanadara, S. Watcharinyanon, A. A. Zakharov, and L. I. Johansson, Phys. Rev. B **82**, 205402 (2010).

[126] A. Sandin, T. Jayasekera, J. E. Rowe, K. W. Kim, M. B. Nardelli, and D. B. Daugherty, arXiv:1111.7009v1 (2011).

[127] J. Soltys, J. Piechota, M. Lopuszynski, and S. Krukowski, arXiv:1002.4717v2 (2010).

[128] S.-M. Choi and S.-H. Jhi, Appl. Phys. Lett. **94**, 153108 (2009).

[129] Y. C. Cheng and U. Schwingenschlögl, Appl. Phys. Lett. **97**, 193304 (2010).

[130] N .P. Guisinger, G. M. Rutter, J. N. Crain, P. N. First, J. A. Stroscio, Nano Lett. **9**, 1462 (2009).

[131] *CRC Handbook of Chemistry and Physics*, 85th ed., edited by David R. Lide (CRC Press, Boca Raton, FL, 2005), Section **9**, pp. 55.

[132] H. McKay, D. J. Wales, S. J. Jenkins, J. A. Verges, and P. L. de Andres, Phys. Rev. B **81**, 075425 (2010).

[133] I. Suarez-Martinez, DPhil Thesis, University of Sussex, 2005.

[134] J. P. Goss, M. J. Shaw, and P. R. Briddon, in *Theory ofDefects in Semiconductors*, Vol. 104 of *Topics in Applied Physics*, edited by David A. Drabold and Stefan K. Estreicher (Springer, Berlin/Heidelberg, 2007), pp. 69-94.

[135] R. W. G. Wyckoff, *Crystal Structures*, Vol. 1, J. Wiley & Sons, New York, London, Sydney (1963), pp. 113.

[136] G. Henkelman, B. P. Uberuaga, and H. Jónsson, J. Chem. Phys. **113**, 9901 (2000).

[137] G. Henkelman and H. Jónsson, J. Chem. Phys. **113**, 9978 (2000).

[138] P. L. de Andres and J. A. Verges, Appl. Phys. Lett. **93**, 171915 (2008).

[139] V. V. Ivanovskaya, A. Zobelli, D. Teillet-Billy, N. Rougeau, V. Sidis, and P. R. Briddon, Eur. Phys. J. B **76**, 481 (2010).

[140] D. W. Boukhvalov, M. I. Katsnelson, and A. I. Lichtenstein, Phys. Rev. B **77**, 035427 (2008).

[141] A. Ito, A. Takayama, and H. Nakamura, Proceed. of ITC/ISHW (2007).

[142] F. Speck, J. Jobst, F. Fromm, M. Ostler, D. Waldmann, M. Hundhausen, H. B. Weber, and Th. Seyller, Appl. Phys. Lett. **99**, 122106 (2011).

[143] J. Yu, G. Liu, A. V. Sumant, V. Goyal, and A.A. Balandin, Nano Lett. **12**, 1603 (2012).

[144] I. Meric, M. Y. Han, A. F. Young, B. Ozyilmaz, P. Kim, and K. L. Shepard, Nat. Nanotechnol. **3**, 654 (2008).

[145] Y. Wu, Y. Lin, A. A. Bol, K. A. Jenkins, F. Xia, D. B. Farmer, Y. Zhu, and P. Avouris, Nature **472**, 74 (2011).

[146] K. V. Emtsev, F. Speck, Th. Seyller, L. Ley, and J.D. Riley, Phys. Rev. B **77**, 155303 (2008).

[147] A. Markevich, R. Jones, S. Oberg, M. J. Rayson, J. P. Goss, and P. R. Briddon, Phys. Rev. B **86** 045453 (2012).

[148] L. H. Hess, M. V. Hauf, M. Seifert, F. Speck, T. Seyller, M. Stutzmann, I. D. Sharp, and J. A. Garrido, Appl. Phys. Lett. **99** 033503 (2011).

[149] J. Singh, *Physics of Semiconductors and Their Heterostructures* (McGraw-Hill, New York, 1993).

[150] Y. Baskin and L. Meyer, Phys. Rev. **100**, 544 (1955).

[151] R. Yan, Q. Zhang, W. Li, I. Calizo, T. Shen, C. A. Richter, A. R. Hight-Walker, X. Liang, A. Seabaugh, D. Jena, H. G. Xing, D. J. Gundlach, and N. V. Nguyen, Appl. Phys. Lett. **101**, 022105 (2012).

[152] Y.-J. Yu, Y. Zhao, S. Ryu, L. E. Brus, K. S. Kim, and P. Kim, Nano Lett. **9**, 3430 (2009).

[153] R. W. Godby, M. Schlüter, and L. J. Sham, Phys. Rev. B **37**(17), 10159 (1988).

[154] S. J. Sque, R. Jones, and P. R. Briddon, Phys. Rev. B **73**, 085313 (2006).

[155] K. C. Pandey, Phys. Rev. B **25**(6), 4338 (1982).

[156] G. Kern, J. Hafner, and G. Kresse, Surface Sci. **366**(3). 445 (1996).

[157] A. V. Hamza, G. D. Kubiak, and R. H. Stulen, Surface Sci. **206**(1-2), L833 (1988).

[158] S. Szunerits and R. Boukherroub, J. Solid State Electrochem. **12**, 1205 (2008).

[159] F.K. de Theije, M.F. Reedijk, J.Arsic, W.J.P. van Enckevort, and E. Vlieg, Phys. Rev. B **64**, 085403 (2001).

[160] K.P. Loh, X.N. Xie, S.W. Yang, and J.C. Zheng, J. Phys. Chem. B **106**, 5230 (2002).

[161] S. J. Sque, R. Jones, J. P. Goss, P. R. Briddon, and S. Öberg, J. Phys. Cond. Matter **17(2)**, L21 (2005).

[162] P. Strobel, M. Riedel, J. Ristein, and L. Ley, Nature **430**, 439 (2004).

[163] Y. Zhang, T.-Ta Tang, C. Girit, Z. Hao, M.C. Martin, A. Zett, M.F. Crommie, Y. Ron Shen, and F. Wang, Nature **459**, 820 (2009).

[164] H. Min, B. Sahu, S.K. Banerjee, and A.H. MacDonald, Phys. Rev. B **75**, 155115 (2007)

[165] K. S. Novoselov, A. K. Geim, S. V. Morozov, D. Jiang, Y. Zhang, S. V. Dubonos, I. V. Grigorieva, and A. A. Firsov, Science **306**, 666 (2004).

[166] A. K. Geim and K. S. Novoselov, Nature Mater. **6**, 183 (2007).

[167] M. Freitag, Nat. Nanotechnol. **3**, 455 (2008).

[168] B. Uchoa, C. Y. Lin, and A. H. Castro Neto, Phys. Rev. B **77**, 035420 (2008).

[169] K. T. Chan, J. B. Neaton, and M. L. Cohen, Phys. Rev. B **77**, 235430 (2008).

[170] F. Schedin, A. Geim, S. Morozov, E. Hill, P. Blake, M. Katsnelson, and K. Novoselov, Nature Mater. **6**, 652 (2007).

[171] T. Wehling, K. Novoselov, S. Morozov, E. Vdovin, M. Katsnelson, A. Geim, and A. Lichtenstein, Nano Lett. **8**, 173 (2008).

[172] H. Pinto, R. Jones, J. P. Goss, and P. R. Briddon, Phys. Status Solidi A **207**, 2131 (2010).

[173] W. Chen, S. Chen, D. C. Qui, X. Y. Gao, and A. T. S. Wee, J. Am. Chem. Soc. **129**, 10418 (2007).

[174] H. Pinto, R. Jones, J. P. Goss, and P. R. Briddon, J. Phys.: Condens. Matter **21**, 402001 (2009).

[175] C. Coletti, C. Riedl, D. S. Lee, B. Krauss, L. Patthey, K. von Klitzing, J. H. Smet, and U. Starke, Phys. Rev. B **81**, 235401 (2010).

[176] Y. Nosho, Y. Ohno, S. Kishimoto, and T. Mizutani, Nanotech. **18**, 415202 (2007).

[177] D. Dongchen, W. Chen, X. Gao, L. Wang, S. Chen, K. Loh, and A. Wee, J. Am. Chem. Soc. **129**, 8084 (2007).

[178] M. Klintenberg, S. Lebègue, M. I. Katsnelson, and O. Eriksson, Phys. Rev. B **81**, 085433 (2010).

[179] W. Y. Gao and A. Khan, J. Appl. Phys. **94**, 359 (2003).

[180] J. O. Sofo, A. M. Suarez, G. Usaj, P. S. Cornaglia, A. D. Hernández-Nieves, and C. A. Balseiro, Phys Rev. B **83**, 081411(R) (2011).